NANYANG
TECHNOLOGICAL
UNIVERSITY
SINGAPORE

Semiconducting Polymer Nanoparticles for Cancer Diagnosis and Therapy

CUI DONG
SCHOOL OF CHEMICAL AND BIOMEDICAL ENGINEERING
2020

Semiconducting Polymer Nanoparticles for Cancer Diagnosis and Therapy

CUI DONG

School of Chemical and Biomedical Engineering

A thesis submitted to the Nanyang Technological University
in partial fulfilment of the requirement for the degree of
Doctor of Philosophy

Statement of Originality

I hereby certify that the work embodied in this thesis is the result of original research, is free of plagiarized materials, and has not been submitted for a higher degree to any other University or Institution.

[Input Date Here]
. . 6/7/2020. . . . . . .
Date

[Input Signature Here]
. . . . Cui Dong . . . . .
CUI DONG

Supervisor Declaration Statement

I have reviewed the content and presentation style of this thesis and declare it is free of plagiarism and of sufficient grammatical clarity to be examined. To the best of my knowledge, the research and writing are those of the candidate except as acknowledged in the Author Attribution Statement. I confirm that the investigations were conducted in accord with the ethics policies and integrity standards of Nanyang Technological University and that the research data are presented honestly and without prejudice.

[Input Date Here]	[Input Supervisor Signature Here]
. . . 6/7/2020.	. . . .
Date	Kanyi Pu

Authorship Attribution Statement

This thesis contains material published in the following peer-reviewed journals in which I am listed as an author.

Chapter 3.1 is published as 'Dong Cui, Chen Xie, Yan Lyu, Zhen Xu, Kanyi Pu. Near-infrared absorbing amphiphilic semiconducting polymers for photoacoustic imaging. *Journal of Materials Chemistry B*, 2017, 5, 4406–4409.'

The contributions of the co-authors are as follows: Prof Pu suggested the materials area and edited the manuscript drafts; I wrote the drafts of the manuscript, the manuscript was co-revised with Dr. Xie and Dr. Zhen; I performed all the materials synthesis, collected the *in vitro* characterization data and conducted data evaluation. Dr. Lyu collected TEM figures; Dr. Zhen and I performed the *in vivo* PA experiments and collected data.

Chapter 3.2 is published as 'Dong Cui, Pengcheng Li, Xu Zhen, Jingchao Li, Yuyan Jiang, Aixi Yu, Xiang Hu, Kanyi Pu. Thermoresponsive semiconducting polymer nanoparticles for contrast-enhanced photoacoustic imaging.' *Advanced Functional Materials*, 2019, 29, 1903461.

The contributions of the co-authors are as follows: Prof Pu suggested the research area and edited the manuscript drafts; Prof Hu and Prof Xu provided the equipment supporting; I wrote the drafts of manuscript, the manuscript was co-revised by Dr. Zhen and Dr. Li; I performed the materials synthesis, performed all the *in vitro* optical, photothermal and PA characterization experiments except that Miss Jiang helped me collecting the TEM data; Dr Zhen, Dr Li and I performed *in vivo* PA imaging experiments; I analyzed data.

Chapter 4 is published as 'Dong Cui, Jingchao Li, Xuhui Zhao, Kanyi Pu, Ruiping Zhang. Semiconducting polymer nanoreporters for near-infrared chemiluminescence imaging of immunoactivation. *Advanced Materials*, 2020, 32, 1906314.'

The contributions of the co-authors are as follows: Prof Pu suggested the materials area and edited the manuscript drafts; Prof Zhang provided equipment and technical assistant; I wrote the manuscript, the manuscript was co-revised by Dr. Li and Dr. Zhao; I performed all materials synthesis, optical characterization, *in vitro* chemiluminescence imaging experiments; Dr. Li and I performed *in vivo* chemiluminescence imaging experiments; The data was analyzed by Dr. Li and I.

Chapter 5 is published as 'Dong Cui, Chen Xie, Jingchao Li, Yan Lyu, Kanyi Pu. Semiconducting photosensitizer-incorporated copolymers as near-infrared afterglow nanoagents for tumor imaging. *Advanced Healthcare Materials*, 2018, 7, 1800329.'

The contributions of the co-authors are as follows: Prof Pu suggested the materials area and edited the manuscript drafts; I wrote the manuscript and the manuscript was co-revised by Dr. Xie and Miss Lyu; I performed the synthesis and *in vitro* characterization of materials, Dr Xie helped me finished *in vivo* imaging of tumor hypoxia; Dr Xie and I performed *in vivo* peritoneal metastatic tumor imaging except that histological analysis was performed by Dr. Li.

Chapter 6.1 is published as 'Dong Cui, Jiaguo Huang, Xu Zhen, Jingchao Li, Yuyan Jiang, Kanyi Pu. Semiconducting polymer nano-prodrug for hypoxia-activated synergetic photodynamic cancer therapy. *Angewandte Chemie International Edition*, 2019, 58, 5920-5924.'

The contributions of the co-authors are as follows: Prof Pu suggested the research area and edited the manuscript drafts; I wrote the manuscript, the manuscript was co-revised by Dr. Huang and Dr. Li; I performed the synthesis, *in vitro* characterization of materials and *in vitro* study of prodrug activation. Miss Jiang collected the TEM data; Dr Li and Dr Zhen helped me finished *in vivo* imaging experiments.

Chapter 6.2 is published as 'Yan Lyu, Dong Cui, He Sun, Yansong Miao, Hongwei Duan, Kanyi Pu. Dendronized semiconducting polymer as photothermal nanocarrier for remote activation of gene expression. Angewandte Chemie International Edition, 2017, 56, 9155-9159.’

The contributions of the co-authors are as follows: Prof Pu, Prof Duan and Prof Miao suggested the research area, Prof Pu edited the manuscript drafts; I mainly performed synthesis of the materials, Dr Lyu finished other work.

[Input Date Here]	[Input Signature Here]
. . 6/7/2020.	. . . . . Cui Dong . . . .
Date	CUI DONG

Acknowledgement

I would like to express my sincere appreciation to my supervisor Prof. Kanyi Pu for his patient guidelines and assistance in the preparation of this thesis report as well as enthusiastic encouragement and useful critiques of my research work. His board knowledge and rigorous scientific research attitude have a profound impact on me. In addition, I really appreciate his concern for my daily life.

I would like to thank Dr Chen Xie, Dr Xu Zhen, Dr Jiaguo Huang, Dr Jingchao Li, Dr. Yan Lyu, Dr. Shasha He, Dr Chi Zhang for their kindly guidelines and assistance in my research experiments. Their stringent careful attitude toward work and superb experimental operation set up a good example for me.

I would like to thank Miss Yuyan Jiang for her excellent cooperation in my experiments. What impressed me most is her unparalleled learning capability with intense thirst for knowledge. My grateful thanks are also extended to Mr. Jingsheng Huang, Mr Cheng Xu and Miss Ziling Zeng for their help on my research.

Finally, I would like to thank my parents for their support and encouragement throughout my study.

Table of Contents

List of Figures

List of Schemes

List of Tables

Summary

Cancer as one of the most common diseases has drawn more and more attention because of its high mortality rate. Although many cancers can be prevented, screening and early detection of primary tumors as well as potential metastases, has a significant impact on the mortality rate. As an emerging kind of organic phototheranostic agents, semiconducting polymer nanoparticles (SPNs) have gained growing attention owing to their diversified optical properties and ideal biophysical features. This thesis report will introduce my previous works on designing and preparation of SPNs for many applications. SPNs were developed as molecular imaging nanoagents for near-infrared (NIR) photoacoustic imaging of tumor with high signal to background ratio, afterglow imaging of tumor hypoxia and metastasis, and biological photo-regulation. In addition, we reported the first kind of organic chemiluminescent nanoreporters (to the best of our knowledge) that can be used for real-time in vivo imaging of cancer immunotherapy and hold great promise for high throughput screening of immunotherapeutics. Moreover, structural modification of precursor polymers has led to SPN based phototherapeutic agents able to convert photoenergy to heat or reactive oxygen species (ROS) for photothermal and photodynamic therapy to solve the tumor hypoxia induced lower anticancer efficiency issue.

Key words: cancer diagnostics and therapy, molecular imaging, semiconducting polymer nanoparticles, photoacoustic imaging, afterglow imaging, tumor hypoxia

1. Introduction

1.1 Molecular imaging for cancer diagnostics

Cancer as one of the most common diseases causes over 9.6 million deaths globally in 2018. Although many cancers can be prevented, screening and early detection of primary tumors (such as breast cancer, cervical cancer, oral cancer, and colorectal cancer), as well as potential metastases, has a significant influence on the therapy regime and the mortality rate of cancers.[1] As reported, many approaches have been applied for cancer diagnosis, such as physical exam, laboratory tests, and biopsy. For instance, complete blood count test as one kind of laboratory tests may reveal an unusual number or type of white blood cells in people with leukemia. In addition, biopsy is the main method doctors diagnose most types of cancer, such as endoscopic biopsy for lung cancer detection, bone marrow biopsy for blood cancer diagnosis and cutaneous biopsy for skin cancer diagnosis. Because of the complexity of disease mechanism, cancer is particularly suitable for detection and characterization by identifying unique molecular signatures.[2] However, traditional macro-scale diagnostic strategies are inadequate for understanding the actual condition a patient is suffering from when discovering a tumor or lesion.[3] Moreover, imaging the molecular interest of cancer requires safe molecular specific contrast agents and cost-effective imaging systems to monitor these agents rapidly and noninvasively *in vivo*.[4] Thus, cancer diagnostics should also achieve the molecular characterization of cancer in real time.

1.1.1 Molecular imaging

Molecular imaging is an emerging technique in the life/physical sciences that has significantly changed our understanding and therapy of diseases (especially for cancer). Molecular imaging can visualize and quantitatively measure the functions of *in vivo* biological and cellular processes.[5] And repeated studies in the same animal is allowed, thus making it possible to collect longitudinal data and reduce the cost. Therefore, compared with anatomical imaging that plays a crucial role in medical imaging for diagnosis, surgical guidance and treatment monitoring, molecular imaging shows improvements in specificity and quantitation for diseases screening, early diagnosis and personalized therapy. In addition, *in vivo* molecular imaging characterizes pathologies of tissues or lesions without invasive biopsies or surgical procedures, which can effectively reduce the side-effect caused by surgery and alleviate the suffering of patients.[6] For instance, *in vivo* molecular imaging can be used to identify and quantify the molecular marker profile of the tumor without the invasiveness of a surgical biopsy for treatment of breast cancer, prostate cancer and ovarian cancer.

Generally, development of molecular imaging focus on two aspects: one is development of molecular imaging techniques and instruments, another is designing imaging probes and contrast agents. Molecular imaging requires high resolution and sensitive instruments to detect specific imaging agents at molecular level. To data, classical imaging modalities, including magnetic resonance imaging (MRI), computed tomography (CT), positron emission tomography (PET), single photon emission computed tomography (SPECT), and ultrasound (US), have been widely used as molecular imaging modalities for applications of cancer diagnosis, drug discovery and theranostics.[7] Take advantage of molecular imaging contrast agents or nanoprobes, these modalities may provide better imaging effect for cancer diagnosis. For example, iodinated nanoparticles were developed for cellular CT imaging of macrophage infiltration.[8] By injection of glucose analog of FDG, FDG-PET has higher accuracy for staging cancer such as non-small-cell lung, gastrointestinal tract cancers.[9] In addition, gold nanoshells conjugated and bovine serum albumin (BSA) and Gadolinium (Gd) (Au@BSA-Gd) was applied as MRI contrast agent for theranostic.[10] However, these modalities have some limitations, such as poor sensitivity for CT and MRI, low spatial resolution for SPECT and PET, ionizing radiation caused safety issues for CT, SPECT and PET.[11] In addition, the cost of these technologies is expensive for preclinical study and cancer early diagnostics. Moreover, most of these modalities need long time to acquire an image, stinting their applications in real-time monitoring of tumor therapy.

1.1.2 Optical fluorescence and bioluminescence imaging

Optical imaging is based on investigating the transmission of light through biological tissue, which is mainly influenced by the processes of absorption and scattering.[12] Optical imaging systems are ideally suited for early detection of cancer and to assess tumor margins and response to therapy because of its various advantages including safety, low cost, real time, non-invasive, high resolution imaging ability.[13] At present, the most widely used optical imaging modalities *in* *vivo* are fluorescence and bioluminescence imaging.

Fluorescence imaging based on fluorescence phenomenon that converting absorbing light energy to emit another wavelength luminescence is a handy and relatively inexpensive method for physiological analysis, diseases screening and diagnosis, drug development, and treatment monitoring.[14] Based on different excitation light wavelength region, fluorescence imaging can be classified as visible light (400-700 nm) fluorescence imaging, the first near-infrared (NIR-I, 700-1000) fluorescence imaging, and the second NIR (NIR-II, 1000−1800 nm) fluorescence imaging.[15] As we known. visible light has limited tissue penetration depth (< 1 mm) and significant attenuation by endogenous molecular, thus scientists research has been focused in the NIR-I and NIR-II regions. For instance, NIR-I fluorescence imaging can be used for deeper visualization of anatomical structures, pathological changes, and metabolic processes *in vivo*.[16] Many materials have been developed as NIR-I fluorescence contrast agents including small molecule organic dyes, quantum dots, and upconversion nanoparticles.[17] For instance, indocyanine green (ICG) conjugated with peptide/antibody/nanoparticles have achieved specific targeting imaging for vasculature, cerebrospinal fluid and human gliomas.[18] DOTA–QD (CdTe/ZnS)–RGD was synthesized for PET/NIR fluorescence imaging of tumor vasculature.[19] However, NIR-I fluorescence imaging still has many drawbacks because of the issues of high tissue autofluorescence and low tissue penetration depth, which may hinder the widespread use for cancer diagnosis and screening.[15] For example, melanoma containing melanin can emit fluorescence within the NIR region and conceal the true fluorescent signal.[20] In contrast, NIR-II fluorescence imaging has obviously decreased background signal and increased tissue penetration depth (5–20 mm) owing to the low photon scattering, autofluorescence and tissue absorption of NIR-II light.[21] However, rare optical agents have been developed as NIR-II fluorescence contrast agents in the past years. The majority of NIR-II fluorophores are inorganic nanomaterials suffering from the safety issues, and carbon-based materials with relatively low quantum yield (QY) and *in vivo* clearance difficulties.[22] Thus, development of organic contrast agents with the emission or absorption above 1000 nm is essential for NIR-II imaging applications.

Bioluminescence imaging is a technique that uses light emitted by enzymatic oxidation reactions of luciferase and its substrate to report biological and pathological activities at the molecular level.[23] Unlike fluorescence imaging, bioluminescence does not need an external light source. Because tissues do not exhibit endogenous bioluminescence, greater sensitivities and higher signal to background ratios (SBR) can be achieved compared with fluorescence techniques.[24] Bioluminescence imaging has been used to investigate the biological processes including protein-protein interactions, gene expression, drugs screening, tumor growth and metastasis, and therapy evaluation.[25] However, bioluminescence imaging still has some drawbacks, such as limited penetration depth, poor spatial resolution at greater depths and limited applications caused by substrate and enzymatic co-factors requirement.[26]

1.1.3 Photoacoustic (PA) imaging

Photoacoustic (PA) imaging (optoacoustic imaging) takes the advantage of the PA effect, was first discovered by Alexander Bell in 1880s.[27] Briefly, PA imaging is a hybrid nonionizing imaging technique that detects ultrasound signals generated by conversion of absorbed nanosecond pulse laser light energy caused rapid thermoelastic expansion of tissue for providing stereoscopic images with real time.[28] PA imaging possesses many advantages such as deeper tissue penetration, higher spatial resolution and better tissue contrast as compared with other optical imaging modalities, because of less ultrasound scattering relative to light when passing through tissue.[29] Thus, PA imaging is an emerging technique that merges the advantages of the high contrast of optical imaging and the high spatial resolution of ultrasound. To image the biological and pathological processes, very few natural light absorbers such as melanin and hemoglobin have been applied as endogenous PA agents. However, most tissues do not have any endogenous molecules to generate PA signals. Recently, many materials have been developed as exogenous PA imaging contrast agents including NIR small molecule organic dyes,[30] fluorescent proteins,[31] porphyrin-based lipidic nanostructures,[32] inorganic nanoparticles,[33] carbon nanomaterials[34] and two-dimensional (2D) materials[35]. For example, IRDye800 conjugated with targets peptides has been developed for imaging glioblastoma and breast cancer. Bacteriophytochrome based genetically-encoded fluorescent proteins (iRFP) could provide higher PA signals of tumors than that of blood. Gold nanocages has been applied for sentinel lymph node

(SLN) mapping at a penetration depth of 33 mm.[36] Single-walled carbon nanotubes (SWCNTs) has been applied for tumor neovascularization imaging.[37] In addition, porphyrin-lipid (phospholipid) provided strong PA signal through mapping of the lymphatic system in rats. However, even with conjugations of a specific targeting ligand, 'always on' PA probes still suffer from low SBR problem because of heavily concentration relying.[38] Activatable PA probes that change their signals in response to the biomolecule of interest, showing low background noise, real-time correlation between signals and diseases status, and concentration-independent contrast.[39] Activatable PA contrast agents have been applied for sensitive imaging of enzymes,[40] small molecule mediators,[41] and pH[42] in living mice. For instance, BHQ3 (MPP2 cleavable peptide)-Alexa750 activatable PA probe was developed for targeting imaging of proteolytic enzyme MMP-2.[43] In addition to small molecular dye, inorganic CuS hyaluronic acid nanoparticle marked by Cy5.5 was designed for PA/fluorescence dual-model imaging response to hyaluronidase, giving stronger fluorescence signals and PA signals delineating the tumor.[44] However, these materials still have limitations, such as photo-bleaching for small molecule organic dyes, ion-induced toxicity or difficulty to be bio-metabolized for inorganic nanoparticles, broad PA sections for carbon and 2D materials, and phototoxicity for porphyrin-based lipidic nanostructures.[45] Thus, development of alternative PA imaging agents is essential.

1.2 Phototherapy

Phototherapy that utilizes photoirradiation to ablate malignant cells has emerged as a promising approach for cancer diagnosis and treatment.[46] As compared to conventional chemotherapy, gene therapy and radiotherapy, phototherapeutic modalities have the advantages of non-invasiveness, negligible drug resistance, minimal side effects, and relatively high therapeutic selectivity.[47] Normally, phototherapy depends on the conversion of light into reactive oxygen species (ROS) for photodynamic therapy (PDT) or hyperthermia (heat) for photothermal therapy (PTT).[48] Phototherapy has shown outstanding results in targeting the origin of various diseases. Moreover, phototherapy can stimulate the innate immune system by triggering an immune response to perform immunological effects by immunologically conveying and long-term releasing theranostic agents, as well as triggering tissue immunological response, and enhancing synergizing immunotherapy.[47] In addition, established tumor cells could be destroyed by selective photochemical and photothermal interactions.[49] Thus, the synergistic effects of photoimmunotherapy (PIT) and PDT or PTT can potentially improve clinical outcomes.

1.2.1 Photodynamic therapy

PDT takes advantage of photosensitizers that are activated by absorption of light energy to initially form the excited singlet state, followed by transition to the long-lived excited triplet state resulting in generation of cytotoxic ROS to induce well-controlled regional cell apoptosis and tissue damage.[50] PDT has been developed as a noninvasive clinical treatment for different types of cancer, such as skin, bladder, lung, and head and neck cancers. ROS are chemical mediators that play key roles in signal transmitting of living organisms, including peroxides, superoxide, hydroxyl radical (·OH) and singlet oxygen ($^1O_2$).[51] As a key component for PDT, photosensitizers have been continuously optimized for improved therapeutic efficacies. Obviously, the dual-specificity of PDT relies on accumulation of the photosensitizers on localized light delivery and in diseased tissue.[50] Porphyrins, chlorins and bacteriochlorins that based on the tetrapyrrole backbone (a structure similar to the protoporphyrin prosthetic group contained in hemoglobin) were developed as photosensitizers for cancer therapy. Except those, some small molecular dyes also applied for PDT, including phthalocyanine, squaraine, methylene blue, rose bengal, BODIPY dyes and so on. In addition of small-molecule dyes, many inorganic and organic nanomaterials have been exploited as photosensitizers, which include metallic nanoparticles,[52] gold nanoclusters,[53] quantum dots,[54] 2D materials,[55] up-conversion nanoparticles (UCPNs),[56] organic porphysome.[57] For example, PEGylated zinc phthalocyanine coated AuNPs was proved that having high photodynamic efficiency and tumor destruction ability for *in vivo* PDT.[58] CdSe-aluminium tetrasulfophthalocyanine (QD-AlSPc) nanocomposites provides agility to utilize different excitation wavelengths to activate the photosensitizer.[59] UCNPs loaded chlorin e6 (photosensitizer, Ce6) and imiquimod (toll-like-receptor-7 agonist, R837) UCNP-Ce6-R837 were prepared as PDT agents for colorectal cancer treatment.[56] In addition, a poly(amidoamine)-Iridium complex was synthesized for imaging and PDT applications.[60] However, the drawbacks of PDT have not been solved by applying these materials. The “always on” photosensitizers may induce harmful photosensitization effects on skin, eyes, and other normal tissues.[61] Despite the promise of PDT in cancer therapy, its oxygen reliance limits the therapeutic effect against tumor hypoxia. In fact, as a result of oxygen consumption and microvascular damage during PDT, PDT even increases the tumor hypoxia to a certain extent and further decreases its antitumor efficacy.[62] Lastly, even at NIR region, the tissue penetration depth of light is limited to a few millimeters, making PDT ineffective for treatment of deep-seated tumors.[63] Thus, developing an effective strategy to amplify or modulate the PDT performances is essential.

1.2.2 Photothermal therapy

PTT uses photo-absorbing agents to efficiently convert the absorbed light (especially NIR light) energy into heat and subsequently induce hyperthermia, resulting in the death of diseased cells.[64] This process leads to either partial or complete ablation of the target tissue over time. In addition, photothermal damage of tumor cells generally initiates when tumor temperature reaches 42 °C. [65] However, PTT often requires the tumor center to reach higher temperatures (above 50 °C). To effectively destruct the tumors, a temperature gradient can form so that the edge of the tumor will reach therapeutic temperatures to kill every cancer cell.[65] Good PTT agents could achieve therapeutic temperatures with less total light energy requirement, thereby decreasing the heat escaping from the target tumor and reducing damage to the surrounding healthy tissue.[66] Photothermal conversion efficiency is an important criterion for designation of photo-absorbing agents.[67] Many nanomaterials with strong absorption in the NIR region have been developed as PTT agents to enhance the heat generation in the target tissue, such as small molecular dyes, gold nanomaterials, graphene oxide (GO) nanosheets, SWCNTs, and metallic nanoparticles.[66] For examples, anti-epidermal growth factor receptor (anti-EGFR) antibodies-modified gold nanorod was developed in PTT for melanoma and squamous cell carcinoma.[68] GO-Chlorin e6 nanosheet has been synthesized to treat tumors by using PTT.[69] Folate-SWCNTs was applied in PTT for treatment of Murine mammary EMT6 tumors.[70] Except that, the copper selenide nanocrystals with a higher photothermal conversion efficiency (22%) than gold nanorods (21%) and nanoshells (13%) is more suitable for PTT than comparable gold nanoparticles.[71] However, these materials still suffer the problems like dose-dependent toxicity, low photothermal conversion efficiency and poor biocompatibility.

1.3 Semiconducting Polymer Nanoparticles (SPNs)

Semiconducting polymer nanoparticles (SPNs) composed of opto-electronically active semiconducting polymers (SPs) and amphiphilic polymer matrixes (Scheme 1) have many applications including electronic devices,[72] sensors[73] and tissue engineering[74] due to their excellent photovoltaic properties.[75] With π-electron delocalized backbones, SPs can form spherical nanoparticles, which is caused by the hydrophobic polymer chain breakage caused by the greatly reduced solvent hydrophobicity from organic solvents to water.[76] Recently, SPNs have gained more and more attention as a new kind of molecular imaging nano-agents due to their excellent optical properties including high absorption coefficients, tunable optical properties, controllable dimensions and high photostability.[77] Moreover, owing to the completely organic and biologically inert components, SPNs have another advantage that intrinsically solves the issue of heavy metal ion-induced toxicity to organisms, and therefore potentially possess good biocompatibility.[78]

SPNs are generally prepared *via* miniemulsion or nanoprecipitation.[79] To endow SPNs with good biodistribution, SPs are generally encapsulated into amphiphilic components such as amphiphilic block copolymers (PEG-*b*-PPG-*b*-PEG), polystyrene polymers and lipids.[80] Therefore, most SPNs could be considered as micellar nanoparticles, which may potentially encounter dissociation issues and subsequently cause aggregation during blood circulation.[81] To avoid the dissociation problems of SPNs, semiconducting polymer amphiphiles (SPAs) composed of the hydrophilic poly(ethylene glycol) (PEG) as side chain and SPs as the backbone could self-assemble into nanoparticles in aqueous solutions *via* hydrophobic interaction. This work will be introduced in my first project.

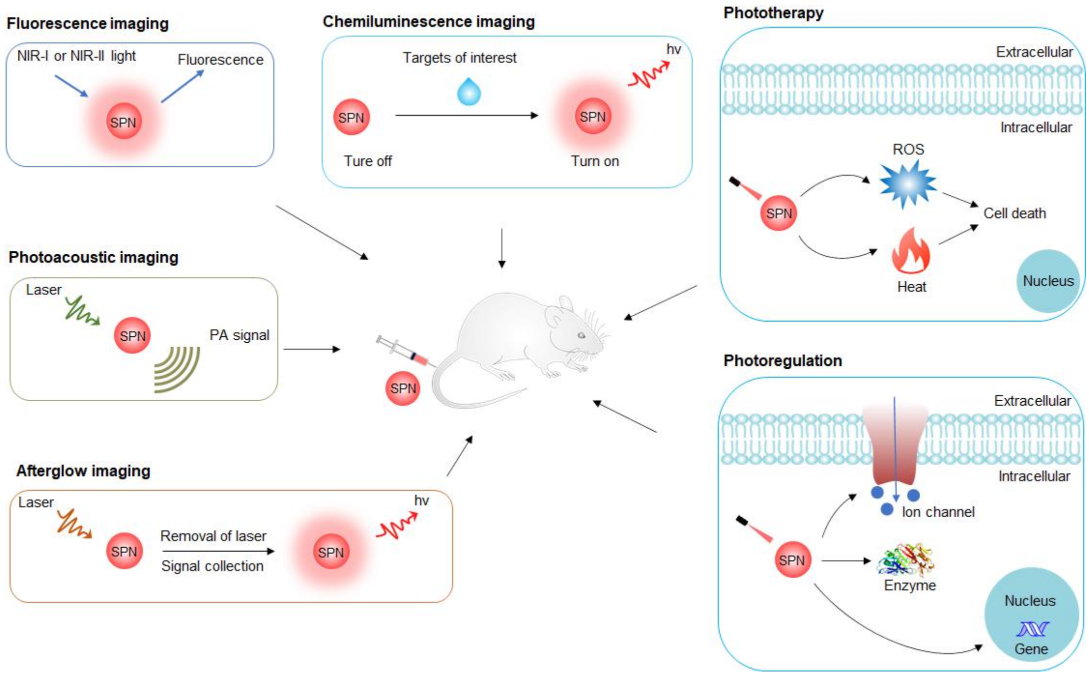

Scheme 1. Summary of the applications of SPNs for optical imaging (fluorescence, photoacoustic, afterglow and chemiluminescence), phototherapy (photodynamic and photothermal therapy) and biological photoregulation.

1.3.1 SPNs for molecular imaging

SPNs have been utilized as a multimodal photonic platform for molecular optical imaging, including fluorescence [82] and photoacoustic imaging [83] (Scheme 1). SPNs as fluorescent probes have been widely reported for molecular imaging and sensing. For example, chlorotoxin (CTX) modified poly[(9,9-dioctylfluorenyl-2,7-diyl)-*alt*-(benzo[2,1,3]thiadiazol-4,7-diyl)] (PFBT, SP1) based SPN1 has been applied for brain tumor fluorescence imaging.[84] Poly(2,5-bis(2-hexyldecyl)-3,6-di(thiophen-2-yl)-2,5-dihydropyrrolo[3,4-c]pyrrolo-1,4-dione-alt-9,9-dioctyl-9H-fluorene) (PCPDTDPP, SP2) based SPA2 was also developed for *in vivo* fluorescence imaging. SPN3 were prepared by encapsulating pendant acetal dextran (m-dextran) modified doxorubicin (DOX) and NIR emissive poly[9,9-bis(N,N-d-imethylpropan-1-amino)-2,7-fluorene-alt-5,7-bis(thiophen-2-yl)-2,3-dimethylthieno[3,4-b]pyrazine] (PFBTT, SP3) into hydrophilic polyvinyl alcohol (PVA). SPN3 was applied for real time DOX release tracking.[85] The continuous release of DOX from SPN3 decreased the intra-particle fluorescence resonance energy transfer (FRET) process in the acidic environment, leading to corresponding fluorescence quenching of SP3 and the recovery of DOX fluorescence. In addition, donor-acceptor (D-A) structure SPN4 was prepared by poly(benzo-[1,2-b:3,4-b]difuran-*alt*-fluorothieno-[3,4-b]thiophene) (Scheme 2, SP4) and DSPE-mPEG. SPN4 could be applied as NIR-II fluorescence imaging agents for real-time cell tracking of arterial blood flow in mouse model.[82]

Many researchers have developed various SPN-based PA imaging agents for *in vivo* imaging of lymph nodes,[78] tumors,[86] glucose,[87] ROS,[88] pH,[89] and protein sulfenic acids[90] (Scheme 2). For instance, poly[4,7(2,1,3-benzothiadiazole) -alt-2,6-(4,4-bis-(2-ethylhexyl)-4H-cyclopenta[2,1-b;3,4-b′]dithiophene)] (Scheme 2, SP5) was transformed into SPN5 for PA imaging of lymph nodes with good NIR light absorption ability, high SBR and PA strength.[78] To enhance the sensitivity of PA imaging for tumor, we incorporated the SPN5 with (6,6)-phenyl-C71-butyric acid methyl ester (PC70BM, Scheme 2) to form intraparticle photoinduced electron transfer (PET) process to increase the heat generation and thus enhance the PA brightness.[80] We also coated SPN2 and SPN5 with a silica shell to reduce the interfacial heat transfer resistance and thus promote heat dissipation, eventually leading to amplified PA signals.[91] In addition, we found that incorporating vinylene bonds into the polymers can facilitate the electron delocalization and increase the mass absorption coefficients, so that SPN6 (Scheme 2, SP6) absorbs more photons and emit stronger PA signals relative to the counterpart.[92] Unlike conventional contrast agents, activatable probes can emit specific signals response to biomolecular targets or events of interest. Compared with other PA contrast agents relied on simple accumulation through the enhanced permeability and retention (EPR) effect or active targeting to sites of interest, activatable PA imaging probes possess several advantages including low background noise, real-time connection between signals and diseases status, and concentration independent contrast.[38] For instance, a ratio-metric PA nanoprobe (rSPN) was developed by doping a ROS-responsive NIR dye (IR775S) with SP2 for real time imaging of peroxynitrite ($ONOO^-$) and hypochlorite ion (ClO^-) in drug-induced mice.[78] Except that, activatable PA probes for pH imaging were also reported. For example, SON-BDP composed of SON and pH sensitive BODDY dye has been developed for pH imaging in tumor tissues.[89]

1.3.2 SPNs for phototherapy

Moreover, structural modification of precursor polymers has led to SPN-based phototherapeutic nano-agents capable of converting light energy into ROS or heat for phototherapy including PDT or PTT (Scheme 1).[93] As reported, $^1O_2$ is the major ROS type generated during PDT with organic SPNs as PDT agents. To enhance the PDT efficiency, incorporation of photosensitizers into SPNs has been developed for PDT. For example, a series of PDT agents were synthesized by doping tetraphenylporphyrin (TPP)[94] and Ce6[95] into SPNs, leading to the improvement of

$^1O_2$ quantum yield and achieving effective cancer PDT in tumor mice model. This is attributed by the efficient resonance energy transfer (RET) from SPs to photosensitizers.[96] In addition to the molecular engineering approaches, O_2-evolving nanoparticles have also been developed for amplified PDT. For example, we have recently synthesized a hybrid core–shell nanoparticle SPN5-MnO_2 composed of manganese dioxide (MnO_2) nanosheets as the shell and SP5 as the core to undergo O_2 evolution in the tumor microenvironment for enhanced PDT.[97] Recently, enzyme-enhanced phototherapy (EEP) with enhanced therapeutic efficiency has been proposed for cancer therapy. For example, glucose oxidase conjugated SPN2 (SPN2-GOx) was synthesized and efficiently catalyzed the conversion of glucose in tumor tissues into gluconic acid and H_2O_2.[98] Upon laser irradiation, ·OH was generated by photolysis of the previous produced H_2O_2, followed by killing cancer cells, suggesting the great potential for effective cancer PDT.

Many SPNs have also been applied for PTT, such as polypyrrole and polyaniline-based SPNs. However, the absorption band of these SPNs is broad and weak in the NIR-I region. To overcome this issue, donor-acceptor structured SPs were synthesized with stronger and sharper NIR absorbance peaks to improve the photothermal conversion efficiency.[99] For instance, PorCP (Scheme 2, SP7) was synthesized for cancer PTT with the absorption maximum at 799 nm.[100] Since PA signal is mainly determined by photothermal conversion, the selection agents used for PA imaging are naturally consistent with those for PTT, which makes PA imaging and PTT an ideal pair for cancer theranostics.[80] SPN5-PC70BM based on intra-particle molecular orbital engineering approach was developed to simultaneously enhance PA brightness and PTT efficacy for *in vivo* imaging and treatment of cancers.[80] In addition, SP nanococktail composed of the amphiphilic PEG grafted phenylenevinylene (PPV) (Scheme 2, PPV-PEG) and NIR absorbing poly(silolodithiophene-alt-diketopyrrolopyrrole) (Scheme 2, SP8) with temperature dependent afterglow luminescence was developed for imaging guided PTT.[101] To effectively destruct deep-seated tumors, NIR-II PTT has been developed owing to the advantages of NIR-II light as compared to the NIR-I light, such as deeper tissue penetration depth and bigger maximum permissible exposure (MPE) for skin.[102] For instance, Poly[(diketopyrrolopyrrole-alt-cyclopentadithiophene)-*r*-(diketopyrrolopyrrole-alt thiadiazoloquinoxaline)] (Scheme 2, SP9) was transferred into SPN9, allowing it for deep-tissue NIR-II PTT. The photothermal conversion efficiency of SPN9 at 1064 nm was 43.4%, allowing it applying for deep tissue PA imaging. After intratumor injection of SPN9 with 1064 nm laser irradiation, the tumors were totally ablated even at a tissue depth of 5 mm. Due to the deep-tissue heating capability, SPN9 showed great potential for effective PTT of xenograft tumors.

1.3.3 SPNs for photoactivation

Photo-regulation (photoactivation) that exploits light stimulus to initiate biological activation has obtained increasing interest because of its advantages, including noninvasive, simple fabrication, good controllability, easy operability, and high resolution. To date, gold nanorods and carbon nanomaterials as well as SPNs have been developed for photoactivation of biological functions including protein ion channels, enzymatic activity, and protein expression. For instance, anti-transient receptor potential cation channel, sub family V, member 1 (TRPV1, Ca^{2+} channel protein) antibodies conjugated SPN2 was synthesized for remote photoactivation of temperature responsive TRPV1 intrinsically overexpressed on the plasma membrane of neurons.[103] In addition, SP1 based SPN1-Bro as pro-nanoenzyme could effectively convert light into heat under NIR laser irradiation at 808 nm to regulate enzyme activity for *in situ* digesting of collagen type I in mice tumor model.[104] Photo-regulation could also be applied to remotely turn on gene expression for curing inherited genetic diseases and cancers.[105] My work is to optimal synthesize dendron SPNs for remote photoactivation of gene expression.

In conclusion, SPNs-based imaging system have many advantages as compared with previous imaging methods, including low dose-dependent toxicity, good photostability and good biocompatibility. Because of the good photothermal conversion ability of SPNs, SPNs-based imaging system could provide low background noise, real-time connection between signals and diseases status, and concentration independent contrast. It is also feasible to use SPNs as phototherapeutic agents for cancer phototherapy Surface conjugation of targeting ligands increases the accumulation of SPNs into tumor sites, making the diagnosis and therapy more accurate and effective. may also be loaded into SPNs could also load inorganic nanoparticles or drugs to generate multifunctional theranostic nanoplatforms for multimodal imaging guided phototherapy and chemotherapy of different diseases.

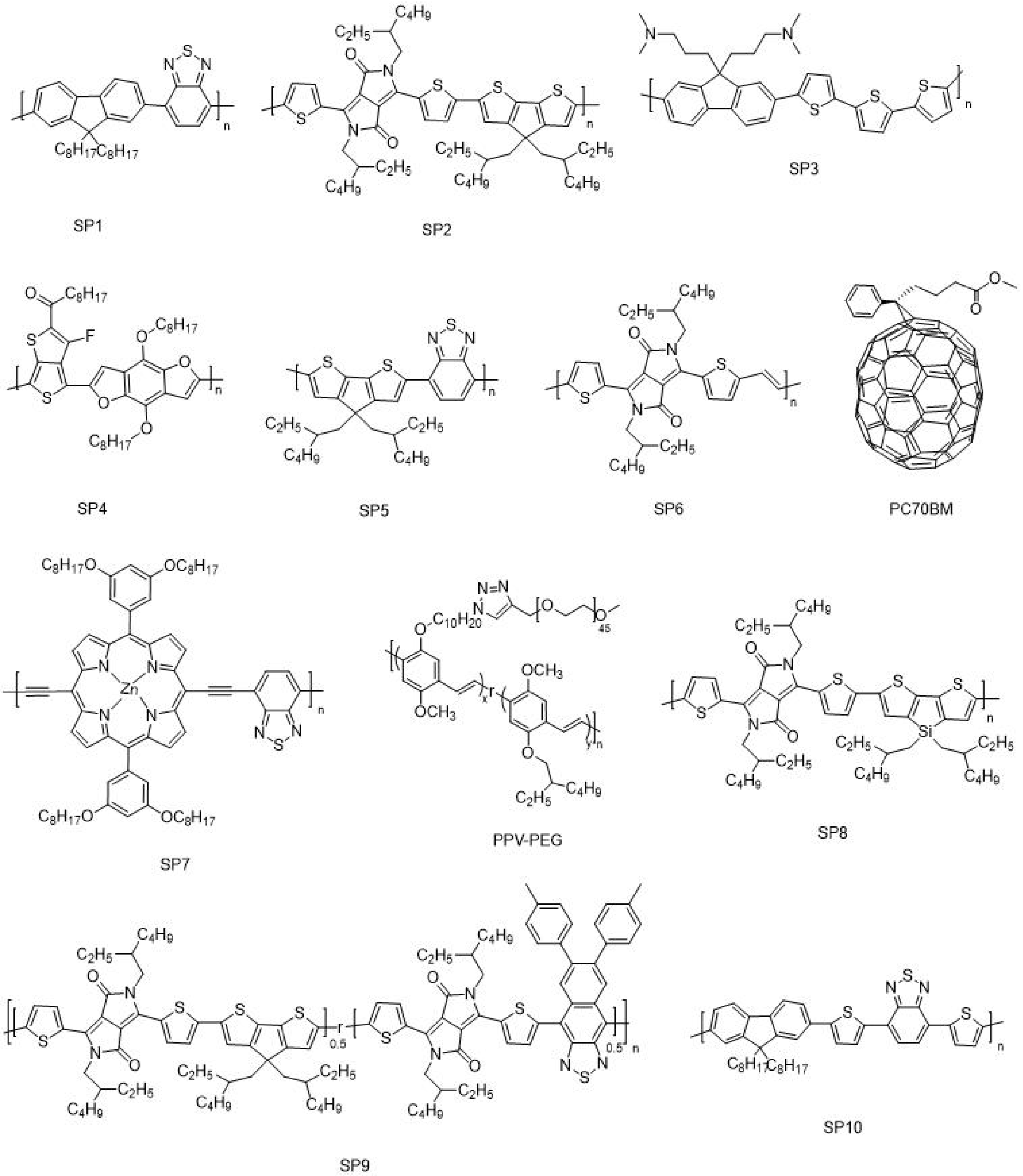

Scheme 2. Chemical structures of SPs and other components for preparation of SPNs.

2. Objectives and corresponding projects

As we reported before, most SPNs could be considered as micellar nanoparticles, which may potentially encounter dissociation issues and subsequently cause aggregation during blood circulation. To avoid the potential dissociation issue of SPNs, we could graft PEG on the backbone of SPs for *in vivo* tumor PA imaging. In addition, the SBR for such probes still heavily rely on the concentration difference of endogenous biomarkers between diseased and normal tissues. By contrast, external stimulus is irrelevant to the location and status of PA agents, and can provide a manual way to noninvasively control the signal generation from the PA imaging agent. Thus, thermoresponsive polymer modified SPNs could be applied for *in vivo* PA imaging of tumor with contrast enhancement. Chapter 3 introduce the work to develop SPNs probes for PA imaging

ROS are chemically reactive molecules derived from oxygen metabolism in living systems. Through preferential reaction with certain groups in biomolecules, they play a crucial role in regulation of biological functions ranging from cell homeostasis to cell death. More importantly, ROS are essential for activation of immune response. Chapter 4 introduces the work to develop a series of $O_2^{\bullet-}$-activatable chemiluminescent semiconducting polymer nanoreporters (SPNRs) for *in vivo* chemiluminescence imaging of immunoactivation in the course of cancer immunotherapy.

Cancer metastasis with its complex cell-biological mechanism, systemic nature, and drug resistance, is the main cause of recurrence and death of most cancer patients. Radiologic imaging approaches have been used for the diagnosis of tumor metastases. However, current methods relatively have low specificity and sensitivity. To solve the challenge of tumor metastasis imaging, we could develop photosensitizer conjugated SPNs as organic afterglow nanoagent. Due to the high sensitivity of afterglow imaging, tiny peritoneal metastatic tumor tissues could be distinguished. Because this afterglow nanoagent is sensitive to oxygen, allowing it for tumor hypoxia imaging.

As a result of oxygen consumption and microvascular damage during PDT, PDT even increases the tumor hypoxia to a certain extent and further decreases its antitumor efficacy. To solve the problem of PDT induced tumor hypoxia, we could synthesize the hypoxia active SP based nano-prodrug for cancer combined PDT-chemotherapy. Chapter 6.2 introduces the synthesis of the dendritic polymer system that integrates the functionalities of gene delivery and photothermal activation, which could be developed into nanomedicines for remotely controlled therapeutic transgene dosing.

In conclude, my works are focused on optimal synthesis and characterization of SPNs for various applications, including PA imaging of tumors, and photo-activation of gene expression, as well as solving some cancer diagnosis and treatment difficulties, including imaging of tumor hypoxia and metastasis, *in vivo* real-time imaging of immuoactivation and overcoming PDT induced tumor hypoxia.

3. SPNs for PA imaging

3.1. Optimized NIR absorbing SPAs for PA imaging

3.1.1 Background

As reported, preparation of SPN is limited to encapsulating of SPs into amphiphilic components *via* nanoprecipitation or emulsion. Thus, most SPNs can be considered to be micellar nanoparticles, which could potentially encounter dissociation and subsequently cause aggregation during blood circulation.[81, 106] To avoid the potential dissociation issue of SPNs, we herein report the design and synthesis of two NIR absorbing amphiphilic SPs that can self-assemble into SPAs for PA imaging. These amphiphilic polymers contain diketopyrrolopyrrole (DPP)-based semiconducting backbone grafted with hydrophilic PEG *via* click reaction. In the following, we report the synthesis methods, characterization of their optical, PA and photothermal properties. Finally, a proof-of-concept application is demonstrated for *in vivo* tumor PA imaging.

3.1.2 Experiment sections

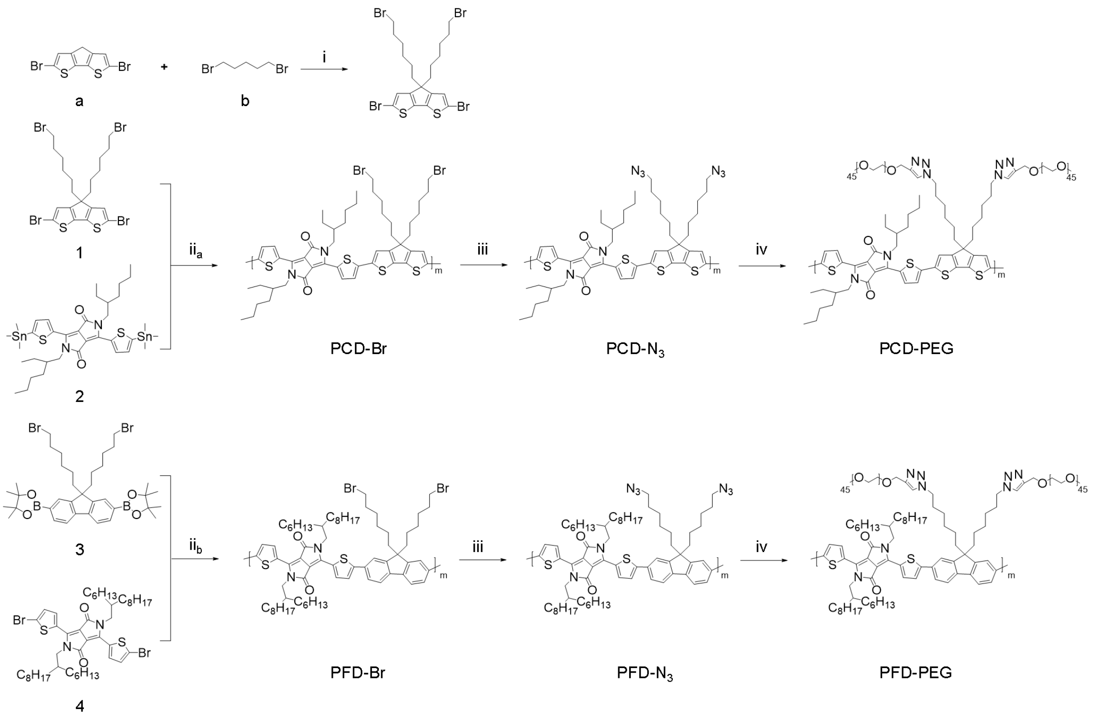

Scheme 3. Synthesis route of PCD-PEG and PFD-PEG. Reagents and conditions: i) 1.6-dibromohexane, tetrabutylammoniumiodide (TBAI), NaOH (50% aq), 75 ºC, 45 min; ii$_a$) bis(triphenylphosphine) palladium(II) dichloride [$PdCl_2(PPh_3)_2$], 2,6-di-tert-butylphenol, toluene, 100 ºC, 2 h; ii$_b$) palladium tetrakis(triphenylphosphine) [$Pd(PPh_3)_4$], potassium carbonate (K_2CO_3), methyltrioctylammonium chloride, toluene/H_2O, 100 ºC, 2 h; iii) Sodium azide (NaN_3), tetrahydrofuran (THF), N,N-dimethylformamide (DMF), 25 ºC, overnight; v) Copper(I) bromide (CuBr), pentamethyldiethylenetriamine (PMDETA), methoxy-PEG-alkyne, THF, 25 ºC, 48 h.

Synthesis of 4,4'-Bis-(5-bromopentyl)-4H-cyclopenta[2,1-b:3,4-b']dithiophene. 2,6-dibromo-4H-cyclopenta-[2,1-b:3,4-b']dithiophene (50 mg, 0.15 mmol), freshly prepared 50% aq NaOH (3.2 mL), and phase transfer catalyst TBAI (10 mg) were added to a 50 ml round Schlenk flask. The Schlenk flask was degassed by applying freeze–thaw cycles, followed by 1.6-Dibromohexane (0.16 mL, 0.38 mmol) addition and the reaction was carried out at 75 °C continuously for 45 min. The crude product was cooled to room temperature and extracted with ethyl acetate (EA) for three times. The organic layer was washed with water for three times and dried over anhydrous sodium sulfate (Na_2SO_4). The EA was removed under vacuum, and the crude product was purified *via* column chromatography over silica/hexane. ^{1}H NMR (300 MHz, $CDCl_3$, δ): 6.92 (2 H, s), 3.34 (4 H, t, *J* = 6.8), 1.76 (8 H, dd, *J* = 18.8, 9.5, 4.6), 1.37 -1.23 (4 H, m), 1.22 -1.08 (4 H, m), 0.97 - 0.81 (4 H, m).

Synthesis of PCD-Br. 4,4'-Bis-(5-bromopentyl)-4H-cyclopenta[2,1-b:3,4-b']-dithiophene (30 mg, 0.041 mmol), 2,5-Bis(2-ethylhexyl)-3,6-bis(5-(trimethylstannyl)-thiophen-2-yl)pyrrolo-[3,4-c]pyrrole-1,4(2H,5H)-dione (35.3mg, 0.042 mmol), $PdCl_2(PPh_3)_2$ (3.5 mg, 0.006 mmol) and 2,6-di-tert-butylphenol (1.2 mg, 5.7 mmol) were added to a 50 ml Schlenk tube. The Schlenk tube was degassed with freeze–thaw cycles to remove air. Then, toluene (5 mL) was added to the tube, which was charged with argon through a freeze-thaw cycle for three times. The mixture was stirred at 100 °C for 2 h. The resulting product was precipitated into methanol to form the dark-green solid. The polymer was purified by extraction using methanol, acetone, hexane and chloroform sequentially. The residue was collected and dried under vacuum. ^{1}H NMR (300 MHz, $CDCl_3$, δ): 8.95 (2 H, s), 7.45 (2 H, d, *J* =92.8), 7.02 (4 H, dd, *J* = 48.7, 30.8), 4.07 (4 H, s), 3.36 (4 H, d, *J* = 6.5), 1.82 (12 H, d, *J* = 37.1), 1.29 (24 H, d, *J* = 24.2), 0.92 (12 H, d, *J* = 7.5).

Synthesis of PFD-Br. 2,7-Bis[9,9(-bis(6-bromohexyl)-fluorenyl)-4,4,5,5-tetramethyl-[1.3.2] dioxaborolane (100 mg, 0.139 mmol), 3,6-Bis(5-bromo-2-thienyl)-2,5-bis(2-hexyldecyl)pyrrolo[3,4-c]pyrrole-1,4(2H,5H)-

dione (126 mg, 0.139 mmol), $Pd(PPh_3)_4$ (5.5 mg, 0.052 mmol), methyltrioctylammonium chloride (1 mg), and K_2CO_3 (244.98 mg, 1.39 mmol) were added in a 50 mL Schlenk flask. Then the solution of water (2.5 mL) and toluene (5 mL) were added to the previous flask, and the system was degassed by applying freeze-thaw circles for three times. The reaction was carried out under vigorously stirring at 100 °C for 2 h. The solvent was removed under vacuum. The obtained solid was dissolved in dichloromethane (DCM) and washed with water for three times. The organic layer was precipitated into excess methanol to remove unreacted monomer. The obtained solid was washed by methanol for three times and then dried under vacuum for 12 h to obtain the PFD-Br. ^1H NMR (300 MHz, $CDCl_3$, δ): 8.96 (2 H, s), 7.62 (8 H, d, $J = 10.7$), 4.38-3.97 (4 H, m), 3.29 (4 H, t, $J = 7.1$), 2.15-1.77 (6 H, m), 1.25 (64 H, t, $J = 9.3$), 0.87 (12 H, dd, J =14.1, 6.5).

Synthetic method for PCD-N_3 and PFD-N_3. PCD-Br or PFD-Br (20 mg) was dissolved into the mixture of THF (6 mL) and DMF (3 mL). To the previous solution, sodium azide (NaN_3) (3 equivalent to Br group of PCD-Br or PFD-Br) was added and the reaction was carried out at room temperature for 12 h. The solvent was removed under vacuum. The crude product was dissolved in DCM. The obtained solution was washed with water for four times and the organic layer was collected. The obtained solution was concentrated and precipitated into methanol to obtain solid. The solid was washed with methanol for three times. PCD-N_3 or PFD-N_3 was obtained under vacuum overnight. PCD-N_3: ^1H NMR (300 MHz, $CDCl_3$, δ): 8.91 (2 H, d, $J = 33.6$), 7.79 -7.29 (2 H, m), 7.09 (2 H, d, $J = 43.3$), 4.07 (4 H, s), 3.21 (4 H, d, *J* = 6.2), 1.78-1.46 (12 H, m), 1.28 (22 H, dd, *J* = 28.7, 11.5), 1.11-0.68 (16 H, m); PFD-N_3: ^{1}H NMR (300 MHz, $CDCl_3$, δ): 8.96 (2 H, s), 7.62 (8 H, d, *J* = 10.7), 4.38 -3.97 (4 H, m), 3.13 (4 H, t, *J* = 7.1), 2.15-1.77 (6 H, m), 1.25 (64 H, t, *J* =9.3), 0.87 (12 H, dd, J =14.1, 6.5).

General Procedure for PCD-PEG and PFD-PEG. PCD-PEG and PFD-PEG polymers were prepared by applying Copper(I) catalyzed alkyne-azide cycloaddition (CAAC) reaction. In brief, PCD-N_3 or PFD-N_3 (3 mg) was dissolved into THF (6 mL). CuBr (2 equivalent to azide group of PCD-N_3 or PFD-N_3), PMDETA (10 equivalent to azide group of PCD-N_3 or PFD-N_3) and methoxy-PEG-alkyne (Mn = 2000, 2 equivalent to azide group of PCD-N_3 or PFD-N_3) were added into previous solution subsequently. The mixture was stirred at room temperature for 48 h. Then THF were removed under vacuum and the resulting residue was dissolved into water. The obtained solution was purified by dialysis against DI water. The PCD-PEG or PFD-PEG polymers were obtained after lyophilization. PCD-PEG: ^{1}H NMR (300 MHz, $CDCl_3$, δ): 7.87-6.68, 4.27-4.12, 3.88, 3.65, 3.55, 3.38, 2.05, 1.45 -1.13, 0.8 PFD-PEG: ^{1}H NMR (300 MHz, $CDCl_3$, δ): 7.79-6.92, 4.35-4.10, 3.92-3.81, 3.74-3.58, 3.58-3.50, 3.43-3.35, 1.91, 1.63 -1.24, 0.86.

Characterization. Dynamic light scattering (DLS) was performed on a Malvern Nano-ZS Particle Sizer. Transmission electron microscopy (TEM) images were captured from a JEM 1400 transmission electron microscope with an accelerating voltage from 40 to 120 kV. The proton nuclear magnetic resonance (^{1}H NMR) spectrums were recorded using a Bruker Advance II 300MHz NMR, $CDCl_3$ was used as the solvent. The gel permeation chromatography (GPC) results were obtained by Shimadzu LC-VP system with polystyrenes as the standard and high purity of THF as the eluent. UV-vis spectra were obtained from a Shimadzu UV-2450 spectrophotometer.

Cell Culture and Cytotoxicity Assay. [3-(4,5-dimethylthiazol-2-yl)-5-(3-carboxymethoxyphenyl)-2-(4-sulfophenyl)-2H-tetrazolium (MTS) viability assay was used for *in vitro* cytotoxicity test by using a breast cancer cell line-4T1 cells derived from the mammary gland tissue of a mouse BALB/c. 4T1 cells were cultured in Dulbecco's Modified Eagle Medium (DMEM) containing 10% fetal bovine serum (FBS) in a humidified environment containing 5% CO_2 and 95% air at 37 °C. 4T1 cells were seeded in 96-well plates (Costar, IL, U.S.A.) at an intensity of 3×10^4 cells/mL. After 24 h incubation, the medium was replaced by fresh medium containing PCD-PEG or PFD-PEG suspensions at different concentrations (10, 25, 50, 75, 100, 125 μg mL^{-1}) and the cells were then incubated for 24 h. After the specified time intervals, MTS reagent was added into cell culture medium for cell incubation. UV measurement (490 nm) was taken after incubation for 3 h, and normalized against untreated samples to the cell viability.

In Vitro Photothermal Studies. Phosphate buffer solution (PBS, pH= 7.4) containing PCD-PEG or PFD-PEG (200 μL, 18 μg mL^{-1}) was exposed to laser irradiation at 808 nm (1 W cm^{-2}). The temperature was monitored using a photothermal camera (FLIR T420) every 20 s until reaching maxima after approximately 6 min. After the laser exposure, the temperature was continuously monitored every 20 s for 6 min. The heating and cooling were repeated five times to test the photothermal stability of PCD-PEG or PFD-PEG.

Tumor Mouse Model. All animal experiments were performed in compliance with the Guidelines established by the Institutional Animal Care and Use Committee (IACUC, Sing Health). To establish tumor models in five-week-old female nu/nu mice, two million 4T1 cells suspended in 50 mL of 50% v/v mixture of Matrigel in supplemented DMEM containing 10% FBS 100 U ml^{-1} penicillin and 100 μg mL^{-1} streptomycin were injected subcutaneously in the shoulders of the mouse. Tumors were grown until a single aspect was ~8 mm (15 days) before used for *in vivo* imaging experiments.

In Vivo PA Imaging of Tumor. 4T1 tumor xenografted nude mice were anesthetized using 2% isoflurane in oxygen, and a catheter was applied to the tail vein. The experimental mice were put in the Endra Nexus128 PA imaging system, and were scanned to detect the endogenous signal of tumors at 790 nm before systemic administration with PCD-PEG (150 μg in 200 μL) (n=3) or saline (200 μL) (n=3) through catheter. Data was acquired through a continuous model that took 12 s to obtain one data set. At different time point (0 h, 8 h, 24 h and 32 h), the PA signals of mice were measured. For *ex vivo* PA imaging, mice were sacrificed by CO_2 asphyxiation, and organs were embedded in agar phantom and acquired immediately with PA imaging system. Three-dimensional PA image was rebuild off-line using data acquired from all 128 transducers at each view. The rebuild raw data was analyzed by using OSiriX software.

3.1.3 Results and Discussions

PEG-grafted poly(cyclopentadithiophenealt-diketopyrrolopyrrole) (PCD-PEG) and PEG-grafted poly-(fluorene-*alt*-diketopyrrolopyrrole) (PFD-PEG), were synthesized *via* a graft-on approach (Scheme 3). The Monomor 2,6-dibromo-4,4-bis-(6-bromohexyl)-4H-cyclopenta-[2,1-b:3,4-b']-dithiophene was synthesized by 2,6-dibromo-4H-cyclopenta-[2,1-b:3,4-b’]-dithiophene and 1.6-dibromohexane under basic conditions. 2,6-dibromo-4,4-bis-(6-bromohexyl)-4H-cyclopenta-[2,1-b:3,4-b']dithiophene (monomer 1) was polymerized with 2,5-bis(2-ethylhexyl)-3,6-bis(5-(trimethyl-stannyl)-thiophen-2-yl)-2,5-dihydropyrrolo[3,4-c]pyrrole-1,4-dione (monomer 2) to yield PCD-Br via Pd-catalyzed Stille coupling reaction, while 2,2'-(9,9-bis(6-bromohexyl)-9H-fluorene-2,7-diyl) bis(4,4,5,5-tetramethyl-1,3,2-dioxaboroane) (monomer 3) was polymerized with 3,6-bis(5-bromothiophen-2-yl)-2,5-bis(2-hexyldecyl)-2,5-dihydropyrrolo[3,4-c]pyrrole-1,4-dione (monomer 4) to yield PFD-Br via Pd-catalyzed Suzuki polymerization. Then, PCD-Br and PFD-Br were respectively reacted with NaN_3 to obtain PCD-N_3 and PFD-N_3.

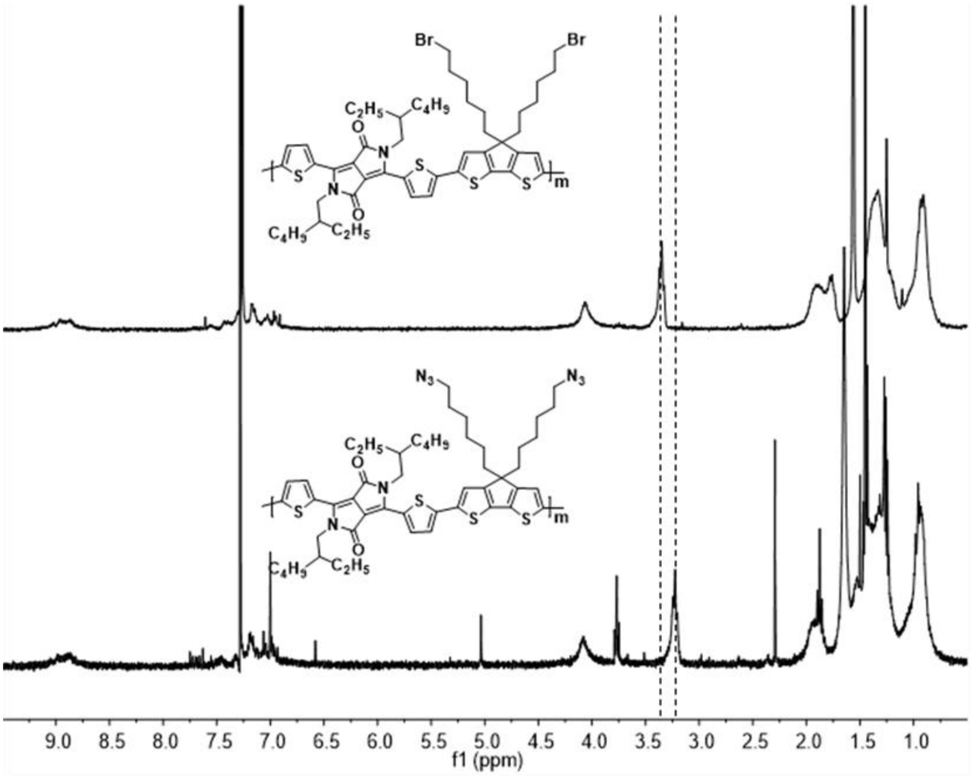

Figure 1. ^1H NMR spectra of PCD-Br (top) and PCD-N_3 (bottom) in $CDCl_3$.

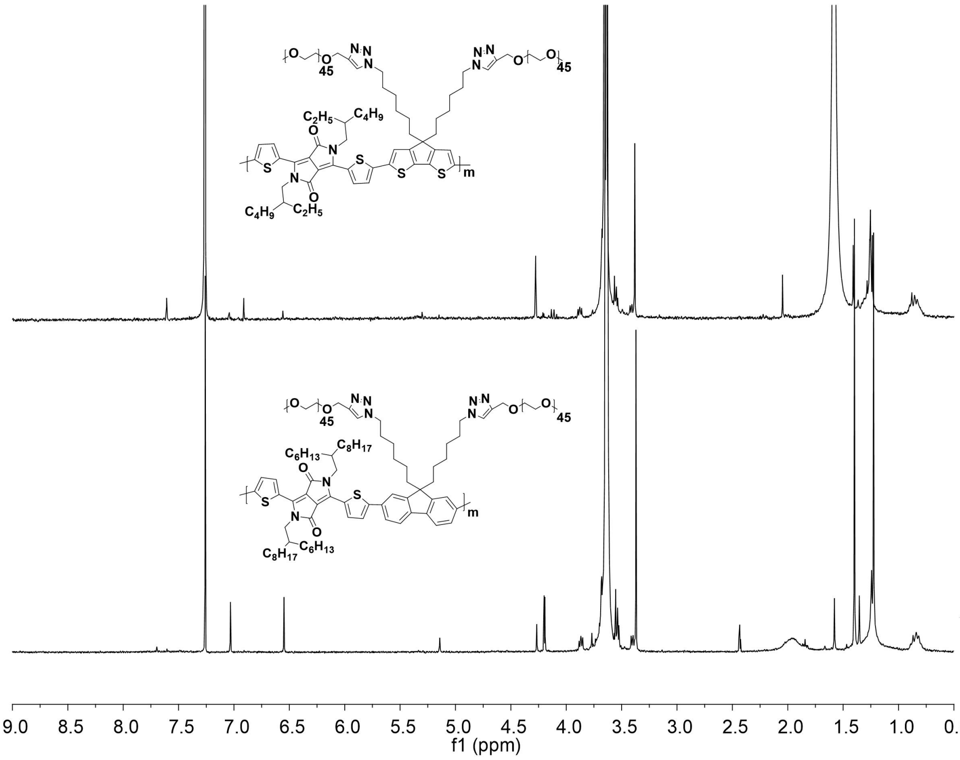

Figure 2. ^1H NMR spectra of PCD-PEG (top) and PFD-PEG (bottom) in $CDCl_3$.

The ^1H NMR spectrum of PCD-N_3 showed that the proton resonance of $-CH_2-N_3$

changed from 3.36 of –CH_2–Br to 3.21, implying that the bromide group was completely substituted by the azide group (Figure 1). Finally, PCD-N_3 and PFD-N_3 were reacted with methoxy-PEG-alkyne (Mn = 2000) *via* Copper(I) catalyzed alkyne–azide cycloaddition (CAAC) reaction to obtain the final amphiphilic polymers: PCD-PEG and PFD-PEG. The chemical structures of PCD-PEG and PFD-PEG were also confirmed by ^{1}H NMR (Figure 2).

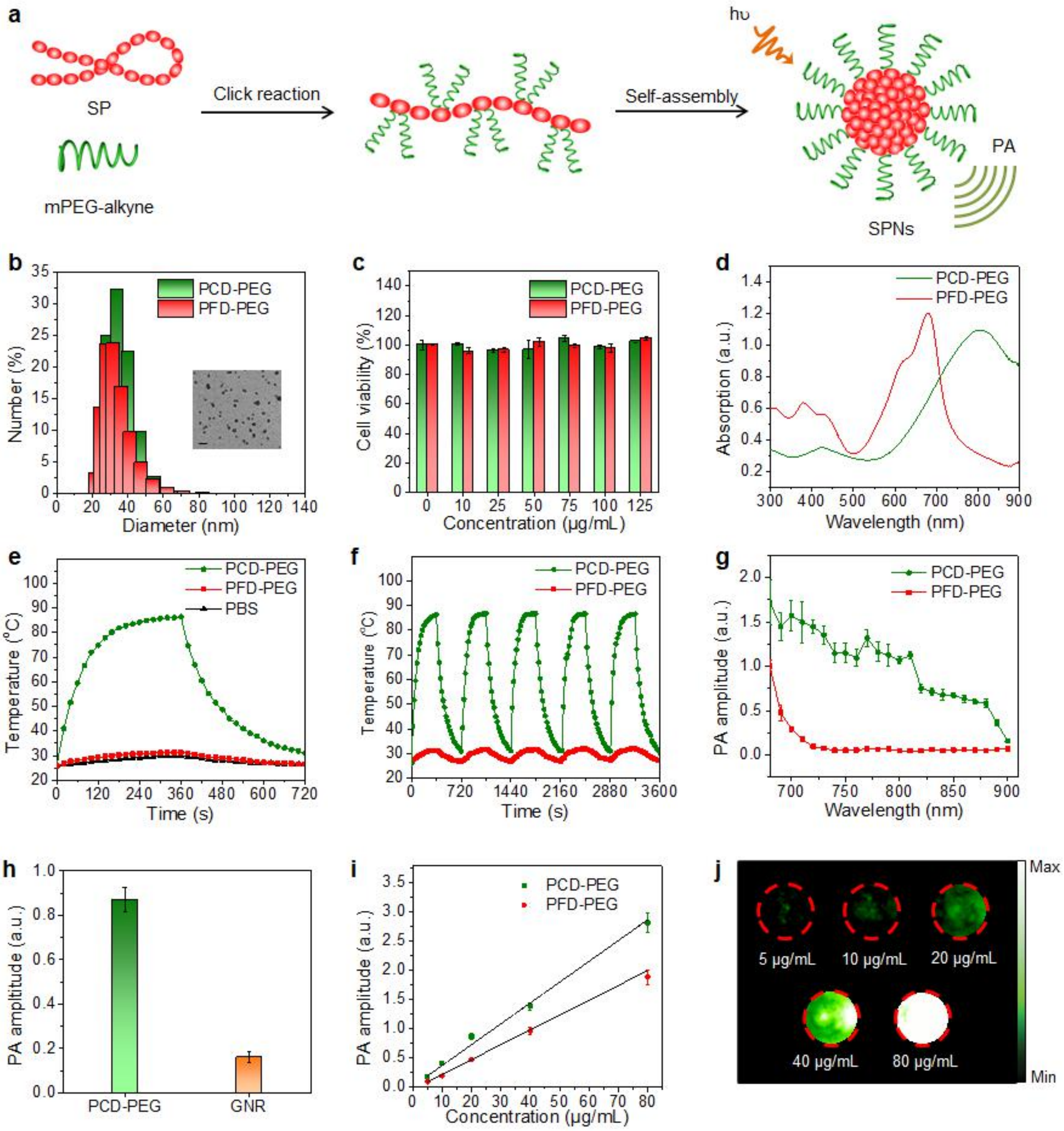

Figure 3. *In vitro* characterization of PCD-PEG and PFD-PEG. a) Schematic illustration of synthesis of amphiphilic SP nanoparticles. b) DLS of PCD-PEG and PFD-PEG. (Insets is TEM

image of PCD-PEG nanoparticles.) c) Cell viability of 4T1 cells after incubation with PCD-PEG or PFD-PEG solutions at various concentrations. d) UV-visible-NIR absorption spectra of PCD-PEG and PFD-PEG. e) Photothermal temperatures of PCD-PEG and PFD-PEG solutions as a function of laser irradiating time. f) Stability study of PCD-PEG and PFD-PEG under photothermal heating and cooling cycles. g) PA spectra of PCD-PEG and PFD-PEG in PBS (pH = 7.4). h) PA signals of PCD-PEG and GNR at 790 nm at the same mass concentration of the optical components. i) PA amplitudes as a function of concentrations of PFD-PEG (680 nm) or PCD-PEG (790 nm). j) PA images of PCD-PEG solutions at different concentrations. Error bars represent the standard deviations (SD) of five separate measurements (n=5).

Both amphiphilic SPs could be dispersed very well in PBS and self-assembly to form amphiphilic PCD-PEG and PFD-PEG (Figure 3a). DLS showed that the average hydrodynamic diameters of PCD-PEG and PFD-PEG were 39 nm and 29 nm, respectively, while TEM images showed that PCD-PEG and PFD-PEG had uniform spherical morphology with diameters of 40 and 30 nm, respectively (Figure 3b). The zeta potentials of PCD-PEG and PFD-PEG were measured to be -4.29 and -2.82 mV, respectively. MTS assay showed that both SPs were non-cytotoxic to 4T1 cells (Figure 3c). These results indicated that these SP nanoparticles had ideal aqueous stability and cytocompatibility for biological applications. The absorption, photothermal, and photoacoustic properties of PCD-PEG and PFD-PEG were tested in PBS solution. At the same concentration of the optical components, the maximum absorption peaks of PCD-PEG and PFD-PEG and were at 803 and 675 nm, respectively (Figure 3d). The red-shifted absorption of PCD-PEG relative to that of PFD-PEG was attributed to the stronger electron-donating ability of cyclopentadithiophene as compared with that of fluorene. Both PCD-PEG and

PFD-PEG showed gradually increasing solution temperatures and attained a plateau at 360 s under continuous laser irradiation at 808 nm (Figure 3e). The maximum photothermal temperature for PCD-PEG was 86 ºC, which was 2.7-fold higher than that for PFD-PEG (32 ºC) (Figure 3e). The photothermal conversion efficiency was calculated according to the natural cooling curve. The photothermal conversion efficiency of PCD-PEG at 808 nm was 37%, 6.17-fold higher than that of PFD-PEG (6%). To study the photothermal stability, both PCD-PEG and PFD-PEG solutions underwent reversible heating and natural cooling 5 times (Figure 3f). Their maximum temperature remained nearly the same, indicating that PCD-PEG was a better photothermal agent as compared to PFD-PEG, probably because of the stronger electron delocalization of the PCD backbone. The PA spectra of both polymers were close to their absorption, showing the maximum intensities at 680 and 790 nm for PFD-PEG and PCD-PEG, respectively. At the same concentration of optical components, the PA amplitude of PCD-PEG at 790 nm was 1.69-fold higher than that of PFD-PEG at 680 nm with the same concentration of optical components (Figure 3g). In addition, the PA amplitude of PCD-PEG was 5.34-fold higher than those of gold nanorods (GNRs) with the absorption maximum close to 790 nm (Figure 3h). The PA amplitudes and images of PCD-PEG at 790 nm were tested at a series of concentrations of the optical components from 5 to 80 mg mL^{-1} (Figure 3i and j), showing a good linear relationship between the PA signals and the polymer concentrations (Figure 3i). These PA data were consistent with the photothermal results. These PA data were consistent with the photothermal results, further proving that PCD-PEG was a better agent than PFD-PEG to convert light energy into heat. Thus, PCD-PEG was chosen for further using *in vivo* PA imaging of tumor.

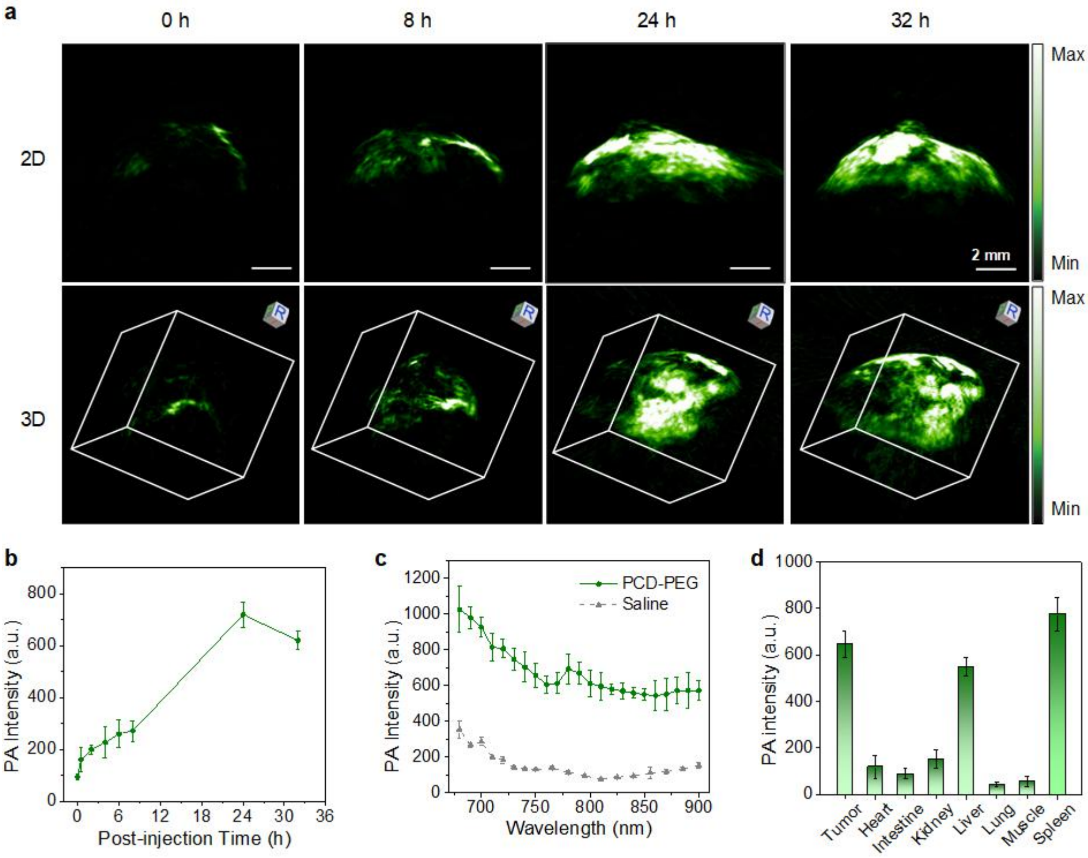

Figure 4. *In vivo* PA imaging of PCD-PEG. a) Representative PA maximum imaging projection (MIP) (upper) and 3D (lower) images of tumor of a living mouse after 0, 8, 24 and 32 h post-injection of PCD-PEG (30 mg mouse^{-1}) via tail vein. b) PA intensities of tumors in PCD-PEG injected living mice as a function of post-injection time. c) *In vivo* real-time PA spectra extracted from the tumors of living mice after systemic administration of PCD-PEG or saline for 24 h. d) *Ex vivo* quantification of major organs from mice 32 h after systemic administration of PCD-PEG. Error bars represent the standard deviations of three separate measurements (n=5).

The PA signals in the tumor areas gradually increased over time after systemic administration of PCD-PEG through intravenous injection (Figure 4a and 4b). In contrast, only weak PA signals of control mice at 790 nm could be detected in the tumor areas due to the low absorption of hemoglobin molecules in the NIR region (Figure 4a). After 2 h post-injection, the PA signals in the tumor areas were 2-fold higher than the background signals, indicating that PCD-PEG quickly accumulated into the tumor site (Figure 4b). At t = 24 h post-injection, the maximum PA signals in the tumor sites were found, showing 7-fold higher than that of the background signals (Figure 4b). At such a time point, the maximum intensity projection (MIP) and 3D PA images obviously illustrated that PA signals originated the areas both within and outside the blood vessels of the tumor (Figure 4a). Thereby, these images and quantified signals showed that PCD-PEG not only passively targeted the tumor but also partially extravasated from tumor vasculatures possibly due to their relatively small diameter (40 nm). In the following, *in vivo* PA spectra were extracted from the tumor areas of PCD-PEG-injected mice to further confirm the nanoparticles accumulation in tumor sites. The PA spectra of PCD-PEG-injected mice clearly differed from that of saline-injected mice, but resembled that of PCD-PEG in aqueous solution (Figure 3g and 4c). The *ex vivo* biodistribution at t = 32 h post-injection showed that PCD-PEG was mainly accumulated in spleen, tumor and liver. Note that the tumor had a relatively strong PA signal which was even higher than that of the liver. The ideal biodistribution of PCD-PEG should be attributed to its non-dissociable nanostructure passivated by a dense PEG shell that reduced the reticuloendothelial uptake and promoted EPR effect. Due to its high PA brightness, PCD-PEG could delineate the tumors of living mice in a clear way (tumor SBR = 7) as compared with previously reported SPNs (tumor SBR = 2 to 5).

3.1.4 Conclusion

In conclusion, we successfully designed and synthesized two NIR-absorbing amphiphilic SPs PCD-PEG and PFD-PEG. Composed of a hydrophobic SP backbone grafted by hydrophilic PEG chains, their photothermal and PA properties were studied. With a stronger charge transfer backbone, PCD-PEG had higher photothermal conversion efficiency (37%) and 1.69-fold higher PA brightness as compared with PFD-PEG. Moreover, the strong PA brightness of PCD-PEG allowed it to image the tumor of living mice with a tumor SBR (SBR = 7). By virtue of low liver uptake, PCD-PEG could be applied for other PA imaging tasks.

3.2 Thermo-responsive SPN for Contrast-Enhanced PA Imaging

3.2.1 Background

As tissues have native chromophores such as hemoglobin and melanin that can efficiently absorb the photoenergy and generate ineluctable background signals, molecular strategies to enhance the SBR have long been desired for PA imaging. For instance, activatable PA probes that change their signals in response to the biomolecule of interest have been developed for sensitive imaging of enzymes,[107] small molecule mediators,[108] and pH[42] in living mice. However, the SBR for such probes still heavily rely on the concentration difference of endogenous biomarkers between diseased and normal tissues. By contrast, external stimulus is irrelevant to the location and status of PA agents, and can provide a manual way to noninvasively control the signal generation from the PA imaging agent, offering extra opportunities to enhance the imaging sensitivity. However, stimuli-responsive agents have been rarely exploited for PA imaging.

In this work, we designed and synthesize thermo-responsive SPNs for *in vivo* PA imaging of tumor. These PA agents are self-assembled from the semiconducting polymer brushes composed of poly(N, N-dimethylacrylamide)-r-(hydroxypropyl acrylate) (PDMA-*r*-HPA) grafts. Thermo-responsive PDMA-*r*-HPA can undergo reversible phase transition in response to the change in environmental temperature. Thus, the resulted SPNs (SPNph1 and SPNph2) had lower critical solution temperatures (LCSTs), above which phase separation occurs to induce the aggregation of these nanoparticles. When the size increases, the heat dissipation is promoted and thus the PA signal is amplified (Figure 9a and 9b). As such, the PA signals of thermo-responsive SPNs can be enhanced by heating, providing a way to remotely enhance the SBRs of PA imaging.

3.2.2 Experiment sections

Synthesis of prop-2-yn-1-yl 2-bromo-2-methylpropanoate. 2-Propyn-1-ol (222 mg, 4 mmol) and triethylamine (878 mg, 8.8 mmol) were dissolved in DCM (10 mL), then α-bromoisobutyryl bromide (2g, 8.8 mmol) was added to the above solution dropwise at 0 ºC. The reaction was carried out at room temperature for 24 h. The resulting solution was washed with water and brine for three times and dried over anhydrous Na_2SO_4. The crude product was purified *via* silica chromatography column (hexane/ DCM = 3/1). The product was obtained as colorless liquid (1.07g, 97 % yield). ^{1}H NMR (300 MHz, $CDCl_3$) δ 4.77 (d, *J* = 2.5 Hz, 2H), 2.51 (t, *J* = 2.4 Hz, 1H), 1.96 (s, 3H).

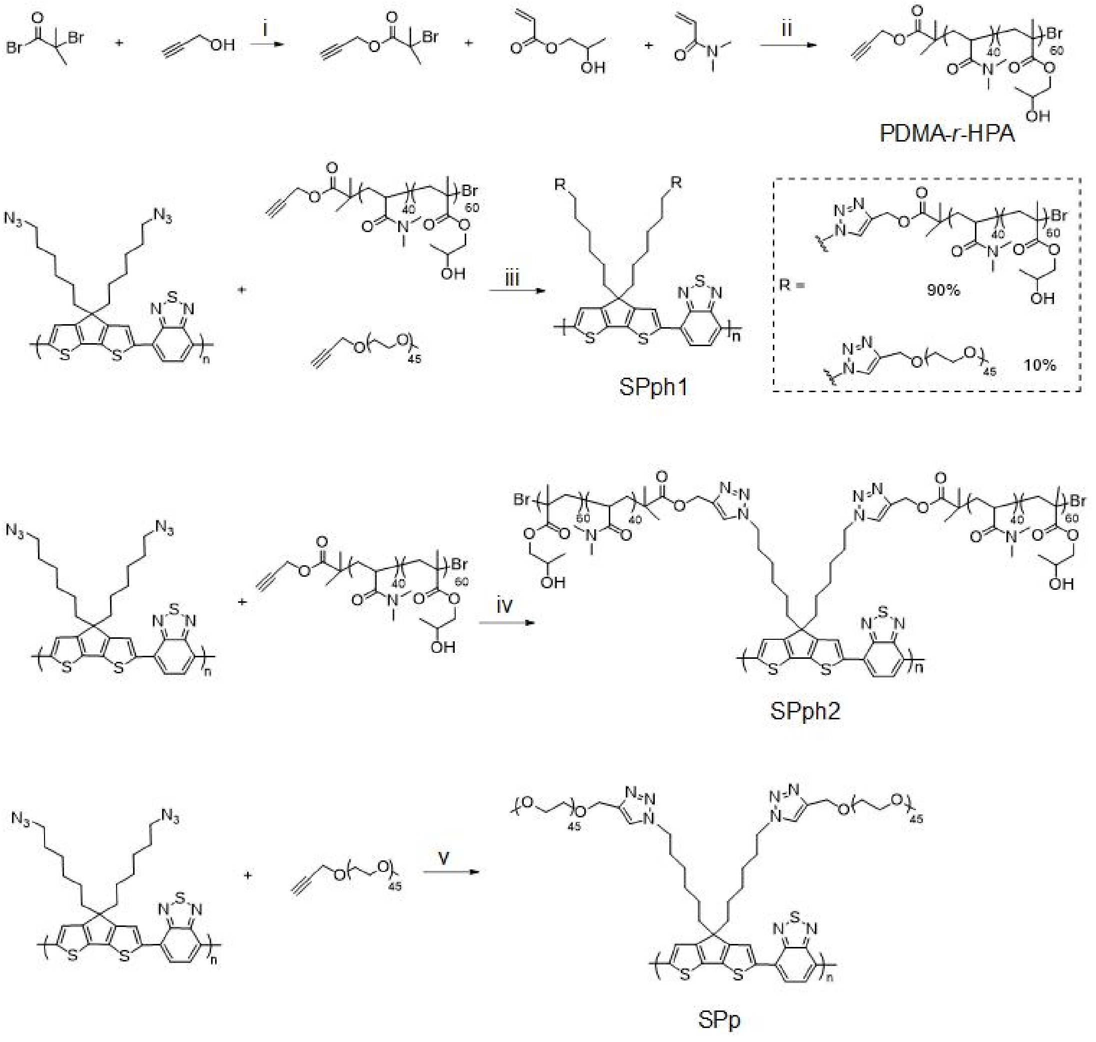

Scheme 4. Synthetic routes for thermo-responsive polymer brushes (SPph1 and SPph2) and the control polymer SPp. Reagents and conditions: i) α-bromoisobutyryl bromide, 2-propyn-1-ol, triethylamine (TEA), DCM, 0 °C, room temperature, 24 h; ii) N,N-dimethylacrylamide (DMA), 2-hydroxypropyl acrylate (HPA), copper (I) bromide (CuBr), 1,4,8,11-tetraazacyclotetradecane (Me_4Cyclam), toluene/ DMF (v/v, 9/1); iii) CuBr, PMDETA, THF, 25 °C, 24 h. iv) CuBr, PMDETA, THF, 25 °C, 24 h; v) CuBr, PMDETA, THF, 25 °C, 24 h.

Synthesis of poly (dimethylacrylamide)$_{40}$-r-(hydroxypropyl acrylate)$_{60}$ (PDMA-r-HPA). N, N-Dimethylacrylamide (500 mg, 5.01 mmol), 2-Hydroxypropyl acrylate (984 mg, 7.56 mmol), CuBr (18.1 mg, 0.13 mmol) and Me_4Cyclam (33.2 mg, 0.13 mmol) were added into a 50 mL Schlenk tube. The reaction system was degassed *via* freeze-pump-thaw cycles for three times. Then the toluene/DMF solution of prop-2-yn-1-yl 2-bromo-2-methylpropanoate (25.84 mg, 0.13 mmol) were added into the tube and degassed *via* freeze-pump-thaw cycles for three times. The mixture was stirred at 90 ºC for 48 h. The solvent was evaporated under vacuum. The crude product was precipitated into diethyl ether. The product was obtained as white solid (1.27g, 84.6% yield). ^{1}H NMR (300 MHz, methanol-D_4) δ 3.99 (s, 120H), 3.59 (s, 40H), 3.05 (d, J = 14.1 Hz, 120H), 2.94 (s, 180H), 2.35 (d, J = 47.0 Hz, 80H), 1.69 (t, J = 61.9 Hz, 220H), 1.21 (s, 180H).

Synthesis of SPph1. PDMA-*r*-HPA (207.8 mg), PCPDTBT-N_3 (was synthesized according to the previous literature) [109] (5.20 mg) and methoxy-PEG-alkyne (Mn = 2000) (2 mg) were dissolved in THF. CuBr (5.5 mg, 0.04 mmol), PMDETA (33.4 mg, 0.2 mmol) were added into previous solution subsequently. The mixture was stirred at room temperature for 48 h. The solvent was evaporated and the residue was dissolved into water. The resulting solution was dialysis against DI water. The SPph1 was obtained after lyophilization. ^{1}H NMR (300 MHz, methanol-D_4) δ 6.45 (m, 4H), 3.89 (d, J = 66.9 Hz, 216H), 3.66 (s, 80H), 3.60 (s, 45H), 3.02 (d, J = 40.7 Hz, 640H), 2.36 (d, J = 45.5 Hz, 128H), 1.65 (d, J = 47.2 Hz, 320H), 1.12 (d, J = 60.9 Hz, 480H).

Synthesis of SPph2. PDMA-*r*-HPA (215.2 mg), PCPDTBT-N_3 (5.18 mg) were dissolved in THF. CuBr (5.5 mg, 0.04 mmol), PMDETA (33.4 mg, 0.2 mmol) were added into previous solution subsequently. The mixture was stirred at room temperature for 48 h. The solvent was evaporated and the residue was dissolved into water. The resulting solution was dialysis against DI water. The SPph2 was obtained after lyophilization. ^{1}H NMR (300 MHz, methanol-D$_4$) δ 7.83 (m, 4H), 3.99 (s, 240H), 3.59 (s, 80H), 3.05-2.94 (m, 600H), 2.35 (d, J = 47.0 Hz, 160H), 1.69 (t, J = 61.9 Hz, 440H), 1.21 (s, 560H).

Synthesis of SPp. PCPDTBT-N$_3$ (5.18 mg) was dissolved in THF. CuBr (5.5 mg, 0.04 mmol), PMDETA (33.4 mg, 0.2 mmol) and compound 4 (Mn = 2000, 40 mg, 0.02 mmol) were added into previous solution subsequently. The mixture was stirred at room temperature under nitrogen atmosphere for 48 h. The solvents were removed and the residue was dissolved into water. The resulting solution was dialysis against DI water for 12 h. The PCDPTBT-PEG was obtained after lyophilization. ^{1}H NMR (300 MHz, CDCl$_3$) δ 7.71 (s, 1H), 7.61 (s, 1H), 7.53 – 7.42 (m, 2H), 4.00 – 3.39 (m, 320H), 1.76 (d, J = 53.7 Hz, 32H), 1.31 (d, J = 33.2 Hz, 32H), 0.87 (d, J = 7.3 Hz, 24H).

Characterization. UV – vis spectra were performed on a Shimadzu UV-2450 spectrophotometer. Fluorescence experiments were carried out on a Fluorlog correlated single photon counting (TCSPC) spectrofluorometer. DLS and zeta potential measurements were performed on a Malvern Nano-ZS Particle Size at different temperature (30, 32, 34, 36, 38, 40, 42, 44, 46, 48, 50 and 52 ºC). TEM images were obtained by using a JEM 2100 PLUS transmission electron microscope with an accelerating voltage from 100 to 200 kV. The samples were incubated at 50 ºC in a water bath for 10 min or room temperature and then dropped onto the specimen grids. GPC was conducted by a Shimadzu LC-VP system with high performance liquid chromatography (HPLC) grade THF as the eluent and polystyrenes as the standard. NMR spectroscopy was obtained on a BRUKER Advance 300 NMR (^{1}H, 300 MHz) system with $CDCl_3$ or methanol-D_4 as the solvent. The spectrum was internally referenced to the tetramethylsilane signal at 0 ppm.

Cell Culture and Cytotoxicity Assay. The *in vitro* cytotoxicity of 4T1 cancer cells was measured using MTS viability assay. 4T1 cancer cells were cultured in DMEM containing 10% FBS at 37 °C and 5% CO_2. 4T1 cells were seeded in 96-well plates (Costar, IL, USA) at a density of 1×10^4 cells per well. After 24 h culture, the medium was replaced by fresh medium containing SPNph1 and SPNp at different concentrations (0, 10, 20, 50, 75, 100 μg mL^{-1}). Then, the cells were incubated for 24 h. After that, MTS reagent was added into cell culture medium (v/v, 1/10) and the cells were incubated for another 3 h. Then the absorbance of cell culture medium at 490 nm was measured and applied to calculate the cell viability.

In Vitro Photothermal Studies. PBS solution (pH = 7.4) containing SPNph1, SPNph2 and SPNp (200 μL, 30 μg mL^{-1}) was exposed to laser irradiation at 808 nm (0.8 W cm^{-2}). The temperature was monitored using an IR thermal camera (FLIR T420) every 20 s until reaching maxima after approximately 8 min. After laser irradiation, the temperature of solution was continuously monitored every 20 s for 8 min. The photothermal stability of SPNph1 and SPNp were tested by the heating and cooling curve with five times repeatment. The photothermal conversion efficiencies were calculated according to following equation: $\eta = [h*S*(T_{max}-T_{surr})-Q_{dis}]/[I*(1-0.1^{A808})]$, I is the laser power for PTT, A is the absorbance of the nanoparticle at 808 nm, and h*S is calculated according to the cooling curve.

In Vitro PA Studies. PBS solution containing SPNph1 or SPNp at 50μg mL^{-1} were placed inside a low-density polyethylene LDPE tube (inner diameter: 0.59 mm; outer diameter: 0.78 mm). The generated PA signals in LDPE tube was coupled to the single-element ultrasound transducer, UST (V323-SU 2.25 MHz^{-1}, 13 mm active area, and 70% nominal bandwidth, Panametrics). Both the tube and UST were immersed in aqueous medium and incubated in a water bath to change the temperature from 25 to 55 ºC. PBS solution containing SPNph1 and SPNp at different concentration (6, 12, 25, 50, 100, 200, 500 μg mL^{-1}) were placed inside LDPE tube with or without laser irradiation at 808 nm (0.8 W cm^{-2}) and imaged using the Endra Nexus 128 PA imaging system.

Tumor Mouse Model. All animal experiments were performed in compliance with the Guidelines established by the Institutional Animal Care and Use Committee (IACUC), Sing Health. To establish tumor models in six-week-old female Ncr nude mice, two million 4T1 cells suspended in DMEM cell culture medium were subcutaneously injected into the shoulder of each mouse. Tumors were grown for 1 week and then the tumor-bearing mice were used for *in vivo* imaging experiments.

In Vivo PA Imaging of Tumor. 4T1 tumor-bearing nude mice were systemically administrated with SPNph1 or SPNp (200 μL, 400 μg mL^{-1}) (n = 3). At before (0 h) and after injection of nanoparticles at different time point (8 h, 24 h and 32 h), the tumors of mice were irradiated by an NIR laser at 808 nm (0.8 W cm^{-2}) for 1 min., An IR thermal camera was applied to monitor the temperature changes in tumor sites during laser irradiation. The tumors of mice with or without NIR laser irradiation were imaged using the Endra Nexus 128 PA imaging system at 680 nm. For *ex vivo* PA imaging, mice were sacrificed by CO_2 asphyxiation, and the tumors and major organs were extracted and immediately imaged using the Endra Nexus128 PA imaging system.

H&E staining. 4T1 tumor-bearing mice after 3 days intravenous injection of SPNp or SPNph1 (200 μL, 400 μg mL^{-1}) were euthanized and the major organs (heart, liver, spleen, lung, and kidney) were extracted for HE staining. The organs were fixed with 4% paraformaldehyde for 24 h, dehydrated in a series of ethanol solution, immersed in xylene, embedded in paraffin and then cut into sections at a thickness of 10 μm. The sections were dried at 40 °C overnight before staining. The dried sections were sequentially immersed in xylene, ethanol and water. After that, the sections were stained with hematoxylin working solution for 5 min and eosin working solution for 5 min. The images of stained sections were captured using a Nikon ECLIPSE 80i microscope (Nikon Corporation, Towa Optics, New Delhi, India).

Data analysis. PA signal amplitudes were detected by region-of-interest (ROS) analysis using OsiriX. Results are expressed as the mean ± SD deviation unless otherwise stated. Statistical comparisons between two groups were determined by

Students t-test. A p value of 0.05 was chosen as the level of significance. And the data were classified according to their p values and denoted by (*) for $p < 0.05$.

3.2.3 Results and Discussions

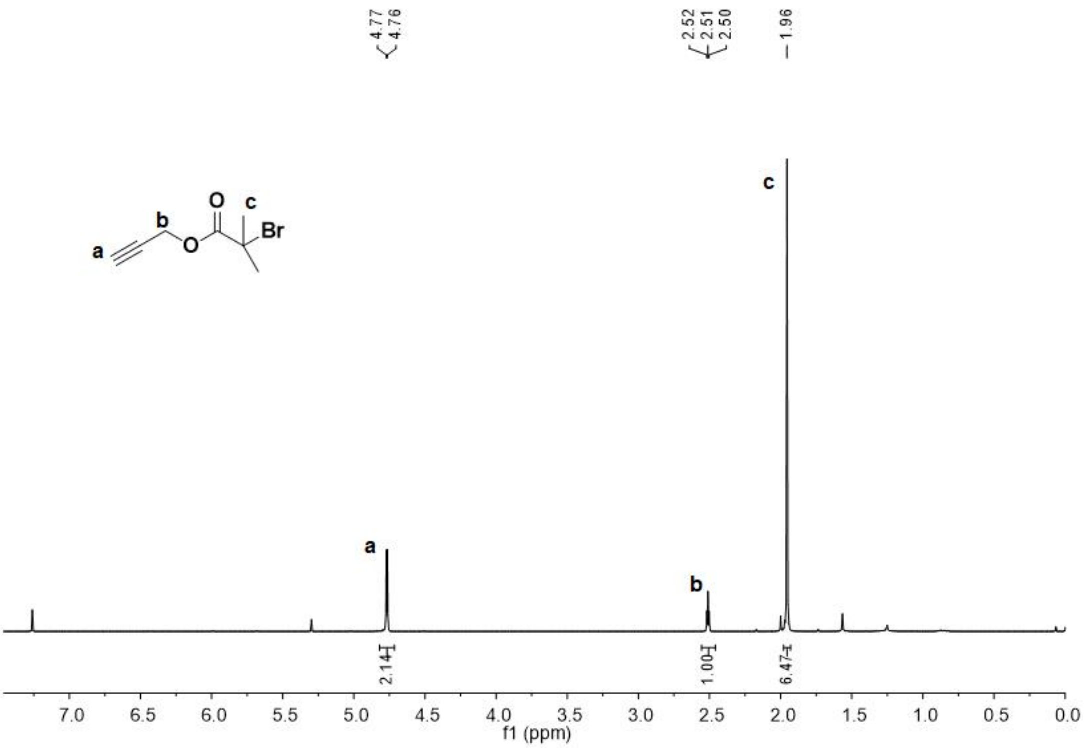

Figure 5. ^{1}H NMR spectra of prop-2-yn-1-yl 2-bromo-2-methylpropanoate in $CDCl_3$.

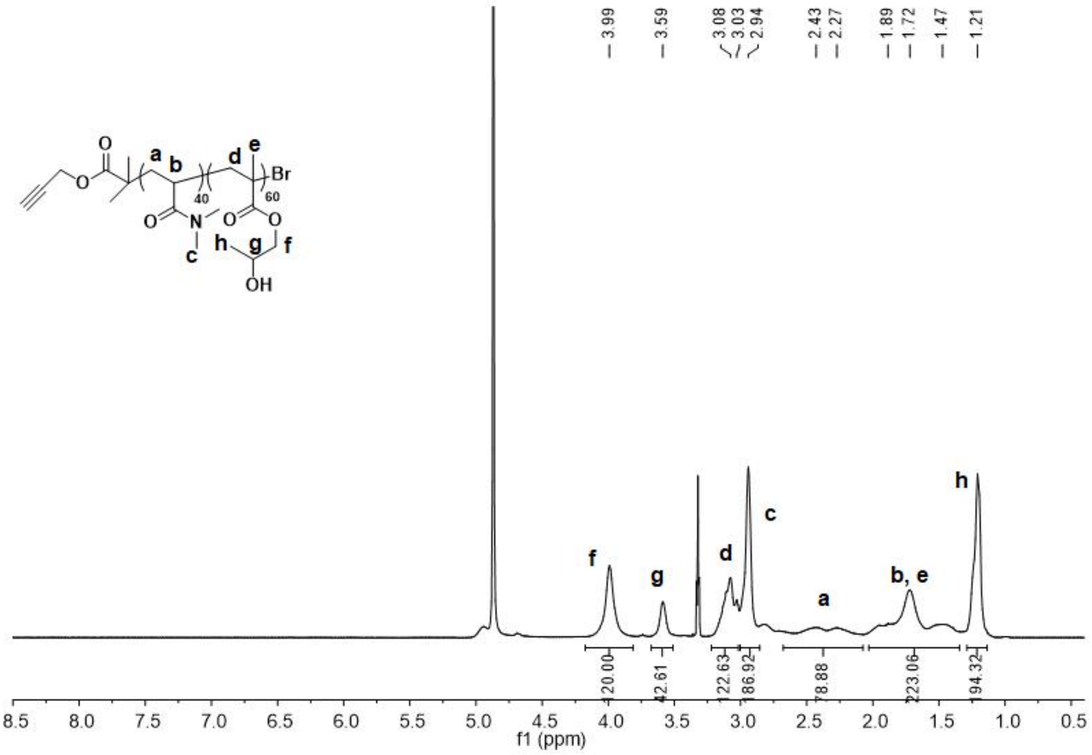

Figure 6. ^{1}H NMR spectra of PDMA-*r*-HPA in methanol-D_4.

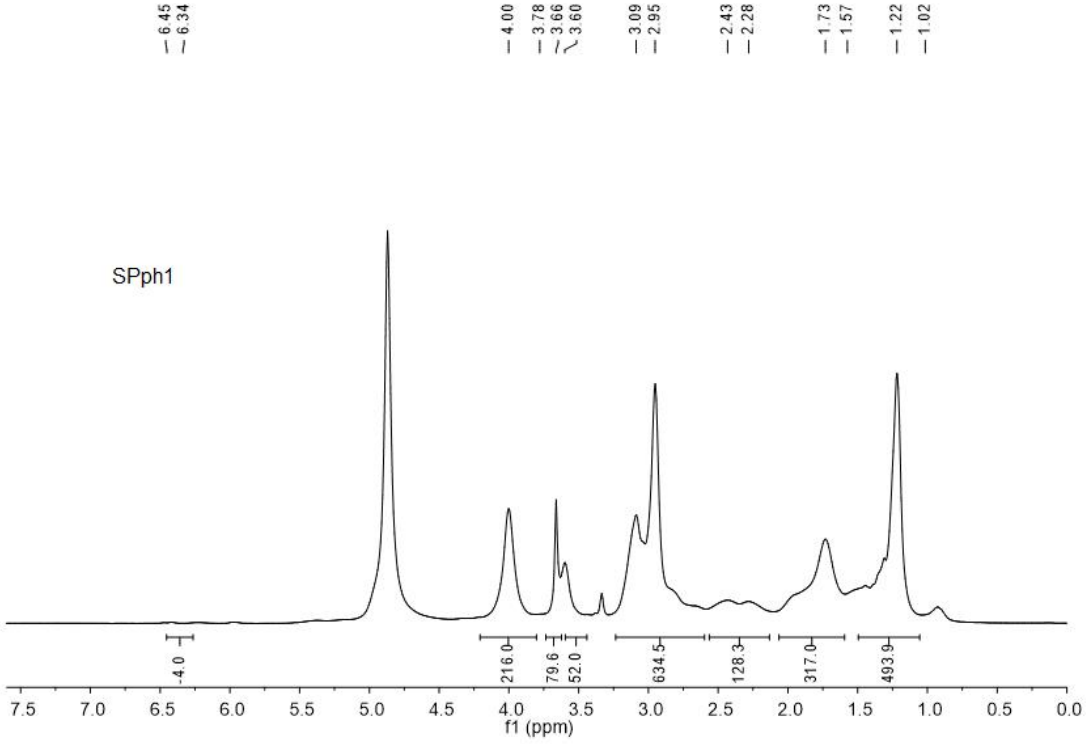

Figure 7. ^{1}H NMR spectra of SPph1 in methanol-D_4.

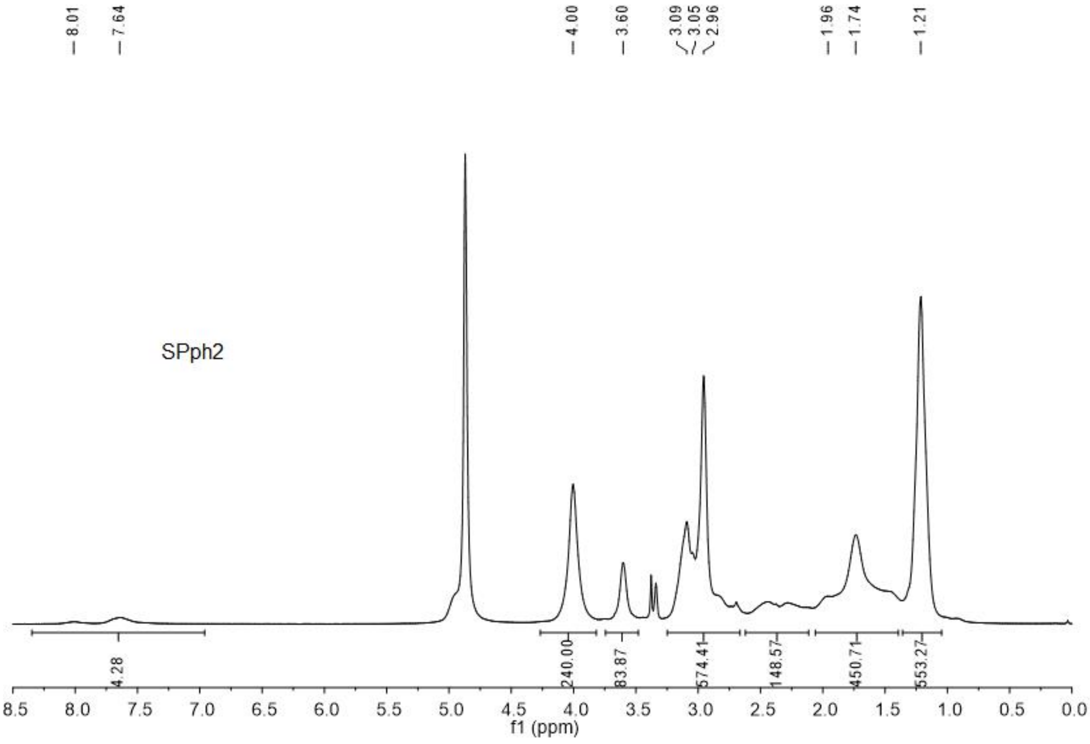

Figure 8. ^{1}H NMR spectra of SPph2 in methanol-D_4.

Sample	Mn (g/mol)	Mw (g/mol)	PDI
PDMA-*r*-HPA	10393	13760	1.32
SPp	22994	33741	1.46
SPph1	78553	128041	1.63
SPph2	122130	188079	1.54

Table 1. GPC data of polymers.

The thermo-responsive semiconducting polymer brushes (SPph1 and SPph2) and the control polymer with only PEG grafts were synthesized *via* a graft-on approach (Scheme 4). As the initiator, prop-2-yn-1-yl-2-bromo-2-methylpropanoate was synthesized *via* alkyne modification of α-bromoisobutyryl bromide, followed by atom transfer radical polymerization (ATRP) using DMA and HPA as monomers, CuBr and Me_4Cyclam as catalyst and ligand, respectively. The ^{1}H NMR spectrum confirmed the right chemical structure of initiator with the characteristic proton resonance peaks at 4.77, 2.51 and 1.96 ppm (Figure 5). The ^{1}H NMR spectrum also showed that the characteristic proton resonance peaks of DMA was found at 3.05, 2.35 and 1.89 ppm, while those of HPA were found at 3.99, 3.59, 2.94, 1.69 and 1.21 ppm (Figure 6). GPC data showed that the number-average molecular weight of PDMA-*r*-HPA was 10,393 with a good polydispersity (PDI), which was close to its designed molecular weight (11954) (Table 1). SPph1 was synthesized by grafting PDMA-*r*-HPA and mPEG-alkyne on azide-modified polymer PCPDTBT-N_3 (the molar ratio of PDMA-r-HPA to mPEG-alkyne was 9:1) via copper(I)-catalyzed alkyne–azide click reaction. Similarly, SPph2 was synthesis via click reaction of PDMA-r-HPA and PCPDTBT-N_3, while the control polymer SPp was obtained via click reaction of PCPDTBT-N_3 and mPEG-alkyne. The ^{1}H NMR spectrum (Figure 7) showed that the characteristic proton resonance peaks of the grafted polymer 2 were found at 3.99, 3.59, 3.05, 2.94, 2.35, 1.89-1.69 and 1.21 ppm, -O-CH_2-CH$_2$-, -O-CH$_2$-CH_2- in PEG were found at 3.66 ppm and the peaks of polymer 3 were found between 8.5-7.0 ppm, implying the correct structure of SPph1. The chemical structures of SPph2 and SPp were also confirmed by ^{1}H NMR (Figure 8). SPph1, SPph2 and SPp could be dissolved in aqueous solutions and spontaneously self-assemble into the corresponding nanoparticles termed as SPNp, SPNph1 and SPNph2, respectively (Figure 9a and 9b).

The optical properties of SPNph1, SPNph2, and SPNp were tested in PBS solution. All SPNs had similar absorption peak ranging from 500 to 900 nm with the maximum at 700 nm (Figure 9c). The fluorescence maximum peaks of SPNp, SPNph1, and SPNph2 were different, which were at 820, 830, and 840 nm, respectively (Figure 9d). This should be attributed to the different conformations of semiconducting polymer backbones governed by the different hydrophobicity/hydrophilicity between PEG and PDMA-*r*-HPA in aqueous solution. The temperature dependent DLS measurements all SPNs had similar hydrodynamic diameters (35 nm) at low temperature (25 °C) (Figure 9e). Upon increasing the solution temperature, a sharp size was observed for both SPNph1 and SPNph2, which was followed by the saturation at the size of 830 nm. By contrast, SPNp did not show such a phase transition behavior. Accordingly, the LCSTs of SPNph1 and SPNph2 were at 48, 42 °C respectively. The lower LCST for SPNph2 relative to SPNph1 was attributed to the higher PDMA-*r*-HPA grafting density. Due to larger PA signal enhancement induced by the higher LCST, SPNph1 was applied for the further studies along with the control nanoparticle (SPNp).

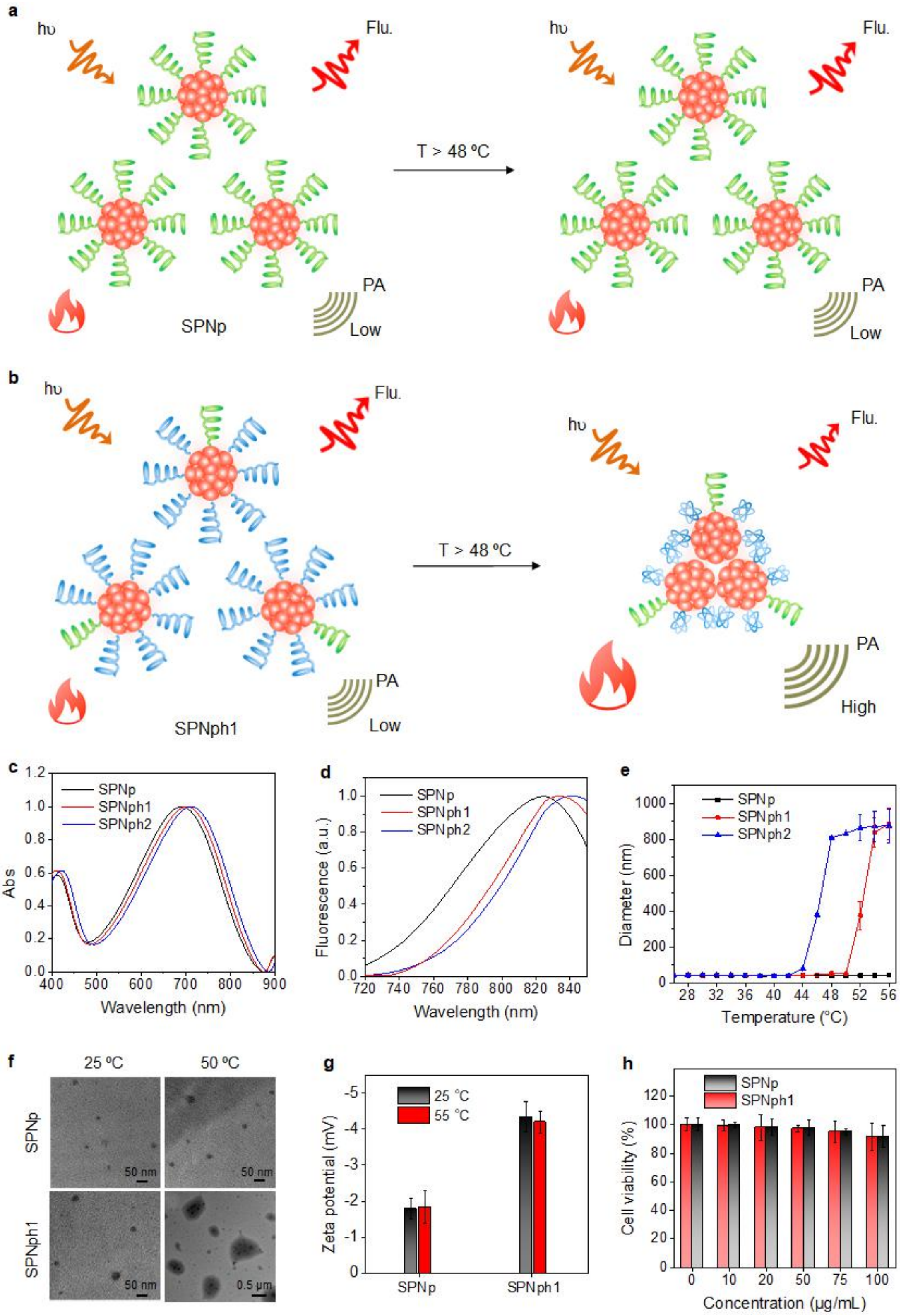

Figure 9. *In vitro* characterization. a) and b) Schematic illustration of heat-amplified PA signals of the thermoresponsive SPNs (SPNph1 and SPNph2) in comparison with the control nanoparticle (SPNp). c) UV−vis absorption and d) fluorescence spectra of SPNs. e) DLS data of

different concentration of SPNs as a function of incubation temperature in PBS (pH = 7.4). f) TEM images of SPNph1 and SPNp after incubation at 25 ºC or 50 ºC. g) Zeta-Potentials of SPNph1 and SPNp after incubation at 25 ºC or 50 ºC. h) Cell viability of 4T1 cells after incubation with SPNph1 or SPNp solutions at various concentrations. Error bars represented standard deviations of three separate measurements.

TEM images also showed that both SPNph1 and SPNp had uniform spherical morphology with an average diameter of about 30 nm at 25 ºC (Figure 9f), while the aggregation was only observed for SPNph1 at elevated temperature. In addition, SPNph1 and SPNp had the zeta potentials of -4.2 and -1.9 mV, respectively (Figure 9g). When the solution temperature was above 50 ºC, the zeta potential of SPNph1 showed non-significant changing. MTS assay showed that both SPNs were non-cytotoxic to 4T1 cells even at a high concentration of 100 µg mL^{-1} (Figure 9h).

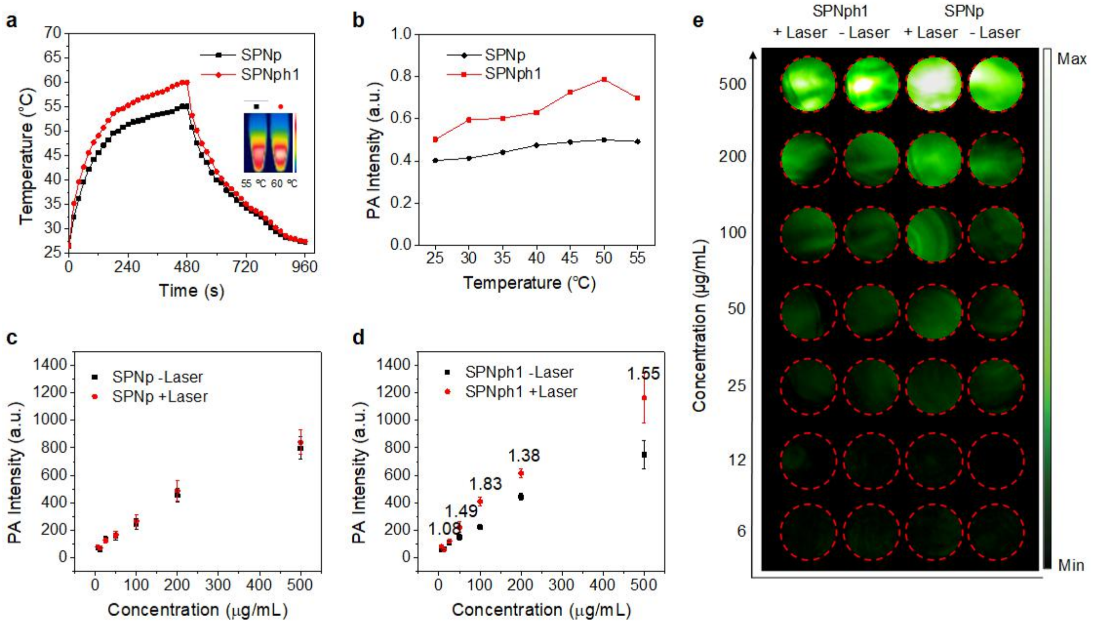

Figure 10. *In vitro* photothermal and PA characterization of SPNph1 and SPNp. a) Photothermal temperatures of SPNph1 and SPNp solutions as a function of laser irradiating time. Insets is IR thermal images of SPNph1 and SPNp at their respective maximum temperatures. b) PA intensity of SPNph1 and SPNp (50 µg mL^{-1}) solutions as a function of surrounding temperatures. PA

intensity as a function of different concentrations of c) SPNp and d) SPNph1 With or without laser irradiation (808 nm, 0.8 W cm^{-2}). e) PA images of SPNph1 and SPNp solutions at different concentrations with or without laser irradiation (808 nm, 0.8 W cm^{-2}).

SPNph1 and SPNp showed increased solution temperature and reached the respective maximum photothermal temperature at 60.0 ºC and 55 ºC at 8 min under continuous laser irradiations at 808 nm (Figure 10a). The photothermal conversion efficiency of SPNph1 was calculated as 34.9%, higher than that of SPNp (26.7%). Due to the higher photothermal conversion efficiency, the PA intensity of SPNph1 was higher than that of SPNp at same concentration (Figure 10b). As the solution temperature increasing, the PA intensity of SPNph1 was significantly increased to the maximum at 50 ºC (consistent with its LCST), which was 1.57 folds higher than that of SPNph1 at 25 ºC. However, the PA intensity of SPNp showed no obviously change with increased solution temperature (Figure 10b). Such PA enhancement of SPNph1 was attributed to its aggregation and formation of large nanoparticles at elevated temperature above LCST. The PA amplitudes and images of SPNph1 and SPNp at 680 nm with or without laser irradiation were determined at a series of concentrations of the optical components from 6 to 500 μg mL^{-1} (Figures 10c, 10d and 10e), showing a good linear relationship between the PA signals and the polymer concentrations. Moreover, compared with no laser irradiation treated SPNph1, the PA amplitudes were respectively increased to 1.49, 1.83, 1.38 and 1.55 folds at the concentration of 50, 100, 200, 500 μg mL^{-1} after laser irradiation. By contrast, laser irradiation had no obvious influence on the PA amplitude for different concentration of SPNp. These data clearly demonstrated that SPNph1 was a better

PA agent with higher conversion ability of light to heat relative to the control (SPNp), and SPNph1 could exhibit PA enhancement with temperature stimuli.

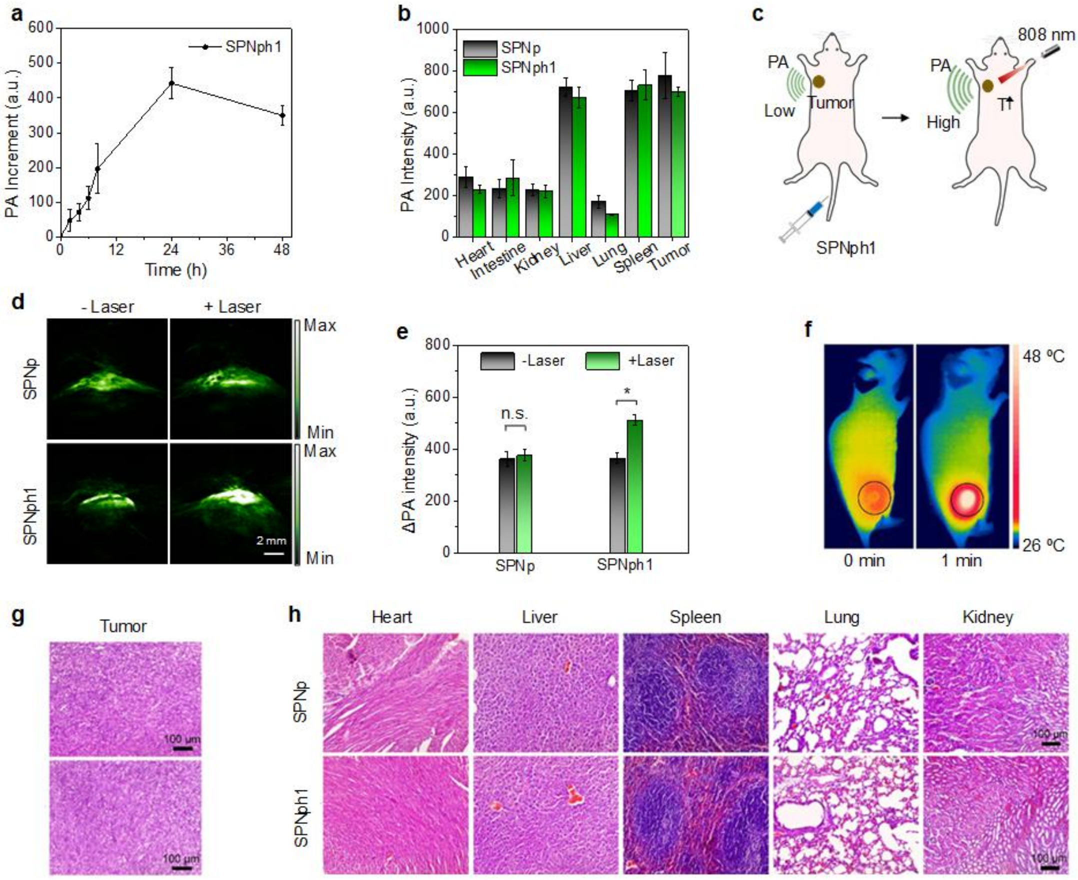

Figure 11. *In vivo* PA imaging. a) PA intensities of tumors in SPNph1 (200 μL, 400 μg mL^{-1})-injected living mice as a function of post-injection time. b) *Ex vivo* quantification of PA of major organs or tumors from mice 32 h after systemic administration of SPNph1 or SPNp. c) Schematic illustration of amplified PA imaging of SPNph1 treated mice tumor. d) PA images of tumor of a living mouse 24 h postinjection of SPNph1 or SPNp (400 μg mL^{-1}, 200 mL) via tail vein with or without laser irradiation (808 nm, 0.8 W cm^{-2}). Scale bar = 2 mm. e) PA intensities of tumors in SPNp or SPNph1 (400 μg mL^{-1}, 200 mL) treated living mice via tail vein with or without laser irradiation (808 nm, 0.8 W cm^{-2}). f) IR thermal images of tumors in 4T1 tumor-bearing mice after intravenous injection of SPNph1 (200 μL, 400 μg mL^{-1}) under a 808 nm laser irradiation (0.8 W cm^{-2}) for 1 min. g) H&E staining images of tumor in 4T1 tumor-bearing mice after intravenous injection of SPNph1 (200 μL, 400 μg/mL) with or without an 808 nm laser irradiation for 1 min. h) H&E staining of the major organs including heart, liver,

spleen, lung and kidney in 4T1 tumor-bearing mice after intravenous injection of SPNp and SPNph1 (200 μL, 400 μg mL^{-1}). Error bars represent the standard deviations of three separate measurements.

SPNph1 and SPNp were evaluated for *in vivo* PA imaging in the subcutaneous 4T1 xenografted tumor model. After systemic administration of SPNph1 or SPNp into the living mice through tail veil, the PA signal was obtained at 680 nm. The PA signals in the tumor areas gradually increased over time after systemic administration of SPNph1 through intravenous injection (Figure 11a). At 24 h post-injection, the maximum intensity projection (MIP) PA images were obtained (Figure 11a), and *ex vivo* biodistribution at t = 32 h post-injection showed both SPNph1 and SPNp were mainly accumulated in spleen, tumor and liver. In addition, tumor had a relatively strong PA signals, which was than that of liver (1.1-fold) (Figure 11b). To further study the thermo-responsive PA amplification of SPNph1, an 808 nm NIR light laser was applied to elevate the temperature of tumors (Figure 11c). After laser irradiation for 1 min, the PA signals of SPNph1 treated tumor was significant enhanced, while that of SPNp treated tumor had no obviously change (Figure 11d). The quantitation data further confirmed that the PA intensity of SPNph1 treated tumor was 1.37-fold increased with laser irradiation, while the PA intensity of SPNp treated tumor remained nearly unchanged (Figure 11e). Thus, the SBR for SPNph1 is increased from 4.16 to 6.12 after laser-mediated heating, showing the advantage of thermo-responsive PA agents in sensitive PA imaging.

Note that the short time (1 min) of elevated temperature (48 ºC) did not cause damage of tumor (Figure 11f and 11g). Without laser irradiation, both of SPNph1 and SPNp showed relative lower PA signals of the tumors (Figure 12a). Moreover, the biosafety of SPNp and SPNph1 was evaluated by hematoxylin and eosin (H&E) staining. No abnormal morphologies for the major organs (heart, liver, spleen, lung, and kidney) were observed in mice after injection of SPNp and SPNph1 (Figure 11h), suggesting their good biocompatibility for PA imaging.

3.2.4 Conclusion

In summary, we have successfully synthesized PDMA-*r*-HPA grafted semiconductor polymer brushes self-assembled into thermo-responsive PA agents for contrast enhanced *in vivo* imaging. By grafting PDMA-*r*-HPA, SPNph1 had LCST at 48ºC and underwent phase separation to form large nanoparticles. Therefore, SPNph1 had thermo-responsive PA characteristic and showed a signal increase of 1.6 times when the temperature is higher than LCSTs. In contrast, SPNph1 photothermal conversion efficiency is 1.3 times higher than that of SPNp without PDMA-*r*-HPA grafting, resulting in higher PA strength at the same concentration. Due to the small molecule (35 nm) located underneath, SPNph could thermo-respond to the PA characteristics of SPNph1 making it possible to remotely control the PA signal in situ by heating mediated by laser laser-irradiation-mediated heating, resulting in a 1.43-fold enhancement in tumor SBR. Therefore, this study introduces a new generation of organic PA nano-agents with thermo-response signals for high contrast tumor imaging.

4. SPNRs for NIR Chemiluminescence Imaging of Immunoactivation

4.1 Background

Chemiluminescence imaging relies on the energy release from chemical reactions has become an ideal technique for various biological analysis and disease diagnosis.[93] Chemiluminescence could be described as a phenomenon in which electrons emit photons when an electron returns from the excited state to the ground state during a chemical reaction.[110] Therefore, the main advantage of chemiluminescence imaging is that requiring no external light source so as to avoid light damage and ignore background noise from biological tissue, allowing it for deep tissue imaging with a relatively high SBR.[111] Until now, a variety of biomarkers including enzymes, ROS, and some small molecular have been detected by using chemiluminescence probes. Recently, we and others have demonstrated that SPNs doped with peroxalate compounds could emit light through chemical reactions without the need of light excitation. SPN-based chemiluminescence imaging has enabled detections of ROS in animal models of hepatotoxicity,[83] peritonitis,[112] neuroinflammation,[113] arthritis,[114] and tumor.[115] For instance, an intraparticle energy transfer approach was reported to amplify the chemiluminescence signals of poly(2,7-(9,9-dioctylfluorene)-alt-4,7-bis(thiophen-2-yl)benzo-2,1,3-thiadiazole) (Scheme 2, SP10) by doping with chemiluminescent substrate peroxalate bis(2,4,6-trichlorophenyl)oxalate for ultrasensitive detection of hydrogen peroxide (H_2O_2).[113] Some researchers also encapsulated organic dye IR775S and bis-(2,4,5-trichloro-6-(pentyloxycarbonyl)-phenyl)oxalate into the SP3 matrix to form SPN3, affording *in vivo* detection of isoniazid (INH) induced hepatotoxicity and anti-pyretic acetaminophen (APAP).[83]

Immunotherapy or biological therapy that aims to train host immune cells to kill malignant cells provides new treatment options for various cancer types. However, immunotherapy often encounters the dilemma of limited patient response rate in the clinic.[116] To optimize immunotherapeutic benefits, approaches to monitor the immune responses in living subjects are highly desired. Current methods include measurements of lymphocytes and immunocytokines from whole blood and biopsies from tumor tissues, which are invasive and not effective in reflection of the dynamic and spatial therapeutic information.[117] At this point, molecular imaging is promising for real-time evaluation of immunoactivation in living subjects.[118] Till now, several antibodies/ligand-based imaging agents have been developed to target immune cell subsets and visualize their presence and abundance.[119] However, due to the "always on" signals of these agents, detection is relied on their passive accumulation and retention in tumors, and thus have poor correlation with the extent of immunotherapeutic response.[120] By contrast, activatable imaging probes that specifically activate signals corresponding to the targeted biomarkers bypass this tissue and possess relatively high signal specificity. However, activatable probes have been rarely exploited for *in vivo* imaging of immunotherapeutic responses.

As we known. ROS are chemically reactive molecules derived from oxygen metabolism in living systems.[121] Through preferential reaction with certain groups in biomolecules, they play a crucial role in regulation of biological functions ranging from cell homeostasis to cell death. More importantly, ROS are essential for activation of immune response.[122] In innate immune response, phagocytes (such as neutrophils and macrophages) spontaneously increase the production of ROS to fight against infections *via* oxidative mechanisms,[123] while in adaptive immune response, T cell receptor (TCR) activation triggers the generation of ROS inside T cells to support T cell activation and cytokine secretion.[124] Thus, ROS can be used as a biomarker for monitoring of immunoactivation. Although fluorescent probes are available for ROS detection,[125] they are rarely exploited for detection of ROS in immune cells, let alone *in vivo* imaging of immunoactivation, probably because of their inadequate biodistribution and poor sensitivity.

Recently, Shabat's group discovered that by addition an electron-withdrawing substituent on the phenol donor of Schaap's chemiluminescent dioxetanes, dramatically improved the luminescence efficiency by three orders of magnitude in aqueous medium.[126] Significant advance has substantially promoted the application of chemiluminescence probes for *in vivo* molecular imaging. In this study, we report the development of a series of $O_2^{\bullet-}$-activatable chemiluminescent semiconducting polymer nanoreporters (SPNRs) and demonstrate their ability in *in vivo* imaging of immunoactivation within cancer immunotherapy.

4.2 Methods

Synthesis procedure

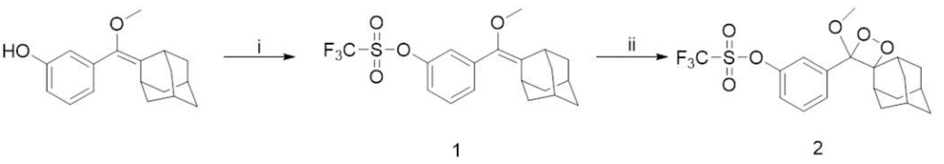

Scheme 5. Synthesis route of chemiluminescence substrate. Conditions: i) Trifluoromethanesulfonic anhydride (Tf_2O), pyridine, DCM, -78 ºC – 25 ºC; ii) methylene blue, MeOH, light irradiation, 0 ºC.

Synthesis of 3-((1r,3r,5r,7r)-4'-methoxyspiro[adamantane-2,3'-[1,2]dioxetan]-4'-yl)-phenyl trifluoromethanesulfonate (Chemiluminescence substrate; 2). 3-(((1r,3r,5R,7S)-adamantan-2-ylidene)(methoxy)methyl)phenol (27 mg, 0.1 mmol) and pyridine (0.75 mL) were dissolved in DCM (2 mL). Tf_2O (100 µL, 0.5 mmol) was added to the above solution at -78 °C. After 1 h, the reaction was carried out at room temperature for another 5 h. The solvent was removed under vauum. The crude product was extracted with DCM and purified *via* colume/silica with hexane/ethyl acetate (v/v, 10/1). Compound 1 was obtained as colorless liquid (48 mg, yield 85.7 %). ^{1}H NMR (300 MHz, $CDCl_3$) δ = 7.53 – 6.75 (m, 4H), 3.53 (m, 3H), 2.02 – 1.66 (m, 3H), 1.30 – 1.03 (m, 11H).

Compound 1 (5 mg) was dissloved in DCM at 0 °C. Methylene blue (3 mg) was added to the above solution. The reaction was carried out under light irradiation for 4 h. Excess methylene blue was removed by flash colume/ silica. Compound 2 was collected as colorless liguid (3 mg, yield 59%). ^{1}H NMR (300 MHz, $CDCl_3$) δ = 7.55 – 6.99 (m, 4H), 3.20 (d, J=20.4, 3H), 1.93 (t, J=21.0, 3H), 1.81 – 1.64 (m, 4H), 1.48

(d, J=20.2, 2H), 1.26 (s, 2H), 1.20 (d, J=8.6, 3H), 0.93 – 0.64 (m, 2H).

Prepartion of SPNRs. Three kind of SPs including poly[(9,9'-dioctyl-2,7-divinylene-fluorenylene)-alt-(2-methoxy-5-(2-ethylhexyloxy)-1,4-phenylene)] (PFPV), poly[(9,9'-dioctylfluorenyl-2,7-diyl)-alt-(benzo[2,1,3] thiadiazol-4,7-diyl)] (PFBT), and poly[2,7-(9,9'-dioctyl-fluorene)-alt-4,7-bis(thiophen-2-yl)benzo-2,1,3-thiadiazole (PFODBT) were used for the preparation of SPNRs. Chemiluminescence substrate 2, PFPV/PFBT/PFODBT and PEG-*b*-PPG-*b*-PEG (m/m/m, 1/40/400) were dissolved in THF (1.5 mL). The obtained solution was rapidly injected into a mixture of DI water (9 mL) and THF (1 mL) under continuous sonication. Then, the solvent was removed by a gentle nitrogen flow. The resulting solution was purified by filtration through a 0.22 μm polyvinylidene fluoride syringe driven filter (Millipore). The obtained nanoparticles solutions were concentrated through ultrafiltration and then diluted by PBS (pH = 7.4) to prepare solutions of different concentrations.

Calculation of quantum yield of SPNR. Using ICG as the reference, the quantum yield of SPNR3 was calculated via following formula: $Q = Q_{ICG} \times I \times OD_{ICG} \times N^2/(I_{ICG} \times OD \times N_{ICG})$, where Q is fluorescence quantum yield, I is the integrated fluorescence intensity, N is the refractive index of solvent (PBS), and OD is the optical density (absorption). Q_{ICG} in PBS is 0.027.

Characterization. DLS was obtained on the Malvern Nano-ZS Particle Size. TEM images were obtained on a JEM 1400 transmission electron microscope. UV-Vis spectra were collected on a UV-2450 spectrophotomete (Shimadzu). Fluorescence experiments were carried out on a Fluorolog correlated single photon counting (TCSPC) spectrofluorometer. Fluorescence and chemluminescence images and spectra were acquired by using an IVIS Spectrum imaging system. NMR spectroscopy was conducted on a BRUKER Advance 300 NMR (^{1}H, 300 MHz) system with $CDCl_3$ as the solvent. The spectrum was internally referenced to the tetramethylsilane signal at 0 ppm. HPLC analysis were performed on an Agilent 1260 system equipped with a G1311B pump, a UV detector and an Agilent Zorbax SB-C18 RP (9.4 × 250 mm) column, with methanol (0.1% of trifluoroacetic acid) and H_2O (0.1% of TFA) as the eluent. ALSM800 confocal laser scanning microscope (Carl Zeiss, Germany) was used to capture the fluorescence images.

Cell Culture and Cytotoxicity Assay. Mouse breast cell line 4T1/normal dermal fibroblasts (NDF) cells were cultured in DMEM containing 10% FBS in a humidified environment containing 5% CO_2 and 95% air at 37 °C. NK cells were cultured in DMEM contaning 10% FBS and 10% IL-2 in a humidified environment containing 5% CO_2 and 95% air at 37 °C. CD^{8+} T cells were isolated from spleen of Balb/c mouse by using the Dynabeads® Untouched™ Mouse CD8 Cells kit, and cultured in RPMI 1640 culture medium in a humidified environment at 37 °C which contains 5% CO_2 and 95% air. The *in vitro* cytotoxicity was measured using MTS viability assay in 4T1 cell line/ NDF cell line. 4T1/NDF cells were seeded in 96-well plates (Costar, IL, U.S.A.) at an intensity of 3×10^4 cells/mL. After 24 h incubation, the medium was replaced by fresh medium containing SPNR3 suspensions at different concentrations (0, 2.5, 5, 10, 20, 50, 100 µg/mL) and the cells were then incubated for 24 h. After the designated time intervals, MTS reagent was added into cell culture medium in 1 to 10 volume ratios for cell incubation. UV measurement (490 nm) was taken after 3 h in an incubator and normalized against untreated samples to the cell viability.

In Vitro chemiluminescence Imaging and Cell Uptake Assay. 4T1 cancer cells, NDF cells and cytotoxic T cells were incubated with SPNR3 at the concentration of 20 µg/mL for 2 h. Then the cell culture medium was removed and the cells were washed with PBS to remove the free nanoparticles. After that, chemiluminescence imaging of treated cells was immediately conducted using a LX71 inverted microscope (Olympus) equipped with infinity (Lumenera) CCD camera. To detect the endogenous intracellular $O_2^{\bullet-}$ level variation, 4T1 cancer cells were pre-treated with BEC (100 mM) for 2 h and/or N-acetyl L-cysteine (NAC, 100 mM) for 0.5 h, followed by incubation with SPNR3 at the concentration of 20 µg/mL for 2 h. chemiluminescence images of treated 4T1 cancer cells was also captured. For NIR fluorescence imaging, 4T1 cancer cells with or without treatments of BEC or NAC, NDF cells and cytotoxic T cells were incubated with SPNR3 at the concentration of 20 µg/mL for 12 h. The cells after treatments were washed with PBS and fixed with 4% paraformaldehyde followed by staining with DAPI. A LSM800 confocal laser scanning microscope (Carl Zeiss, Germany) was used to capture the fluorescence images of cells.

Mouse Tumor Model. All animal studies were conducted in compliance with the guidelines established by the Institutional Animal Care and Use Committee (IACUC), Sing Health. Four-week-old BALB/c mice were purchased from InVivos (Singapore). To establish tumor models, 4T1 cancer cells suspended in DMEM cell culture medium were subcutaneously implanted into the right back of mice (2×10^6 cells/mouse).

In Vivo Tumor NIR Fluorescence and chemiluminescence Imaging. After 6 days of tumor implantation, 4T1 tumor-bearing BALB/c mice were randomly divided into two groups (n = 3). For one group, the mice were injected with saline (200 μL) through tail vein. For another group, the mice were injected with BEC (200 μL, 20 mg kg^{-1} body weight) through the tail vein a time interval of 2 days for 3 times. After that, the mice in each group were intravenously injected with 200 μL PBS solutions of SPNR3 (500 μg/mL). At before (0 h) and different post-injection timepoints, *in vivo* imaging was performed. Fluorescence images were acquired using an IVIS spectrum imaging system with excitation wavelength at 520 nm and emission wavelength at 700 nm. Chemiluminescence images were acquired under bioluminescence mode with an open filter and an acquisition time of 240 s. The fluorescence and chemiluminescence intensities of tumors in each mouse was quantified using a Living Image software.

Ex Vivo Biodistribution. At 60 h post-injection of SPNR3, 4T1 tumor-bearing mice in each group were euthanized (n = 3). The tumors and major organs inclusing heart, liver, spleen, lung, and kidney were extracted and imaged using the IVIS imaging system with excitation wavelength at 520 nm and emission wavelength at 700 nm.

The fluorescence intensities of the tumors and organs were quantified using a Living Image software.

Immunofluorescence Staining. The tumor tissues extracted from each mouse were fixed with 4% paraformaldehyde for 24 h. Then tumors were dehydrated with 30% sucrose, embedded in frozen optimal cutting temperature (O.C.T.) medium and cut into sections at a thickness of 10 μm using a cryostat (Leica, CM1950). The sections were dried at room temperature for 60 min, and washed with PBS containing 0.1% Triton X-100, following by incubation with 3% bovine serum albumin (BSA) solution at room temperature for 60 min. The sections were washed with PBS and incubated with Alexa Fluor 488 conjugated anti-CD8 antibody or Alexa Fluor 560 conjugated anti-CD4 antibody at 4 ºC for 12 h. Subsequently, the tumor sections were washed with PBS to remove unbound antibody and then further incubated with DAPI solution at room temperature for 20 min. Fluorescence images of stained sections were captured using a LSM800 confocal laser scanning microscope.

H&E Staining. The major organs (heart, liver, spleen, lung, and kidney) extracted from each mouse were fixed with 4% paraformaldehyde for 48 h. The fixed organs were dehydrated in a series of ethanol solution, immersed in xylene, embedded in paraffin and then cut into sections at a thickness of 10 μm. For H&E staining, the sections were sequentially immersed in xylene, ethanol and water. Then the sections were immersed in hematoxylin working solution for 5 min. After water washing, the sections were then immersed in eosin working solution for 3 min. The images of stained sections were captured using a Nikon EchemiluminescenceIPSE 80i microscope.

4.3 Results and Discussions

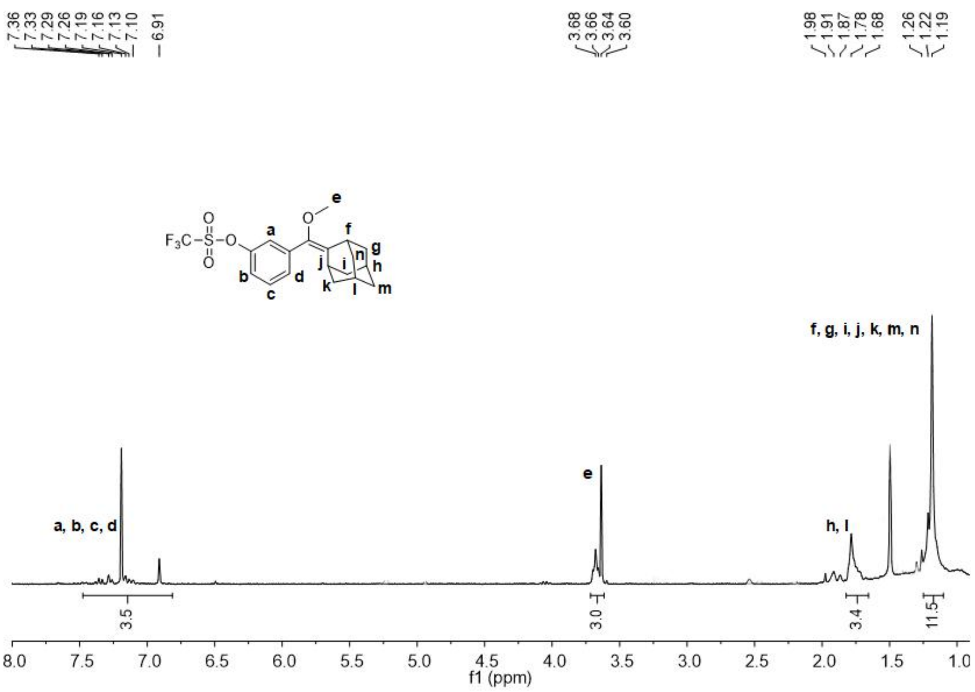

Figure 12. ^{1}H NMR spectra of compound 1 in $CDCl_3$.

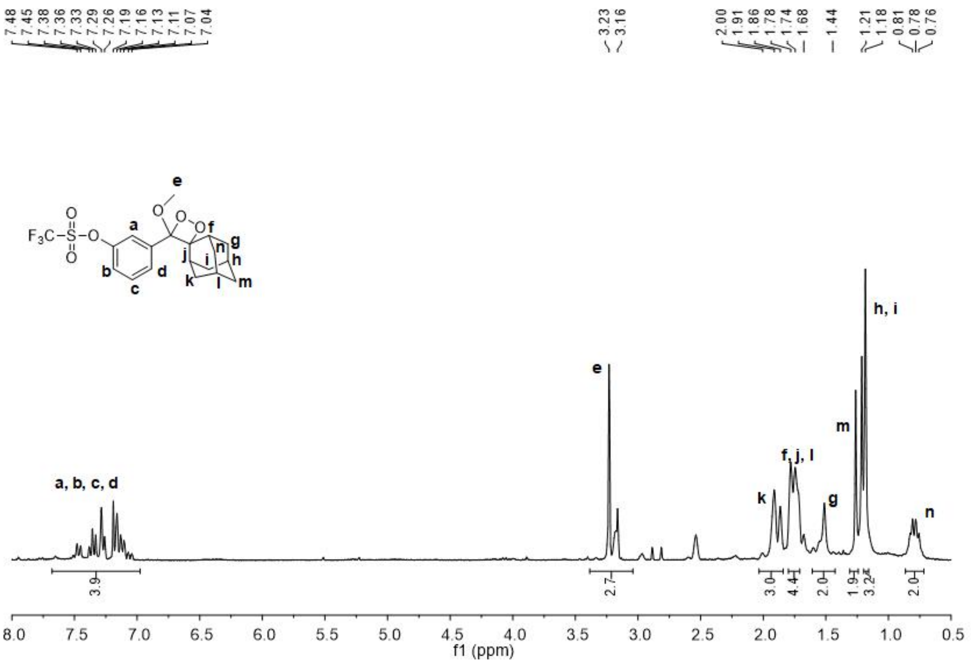

Figure 13. ^{1}H NMR spectra of compound 2 in $CDCl_3$.

To prepare chemiluminescent SPNRs, Tf group caged chemiluminescence dioxetane, 3-((1r,3r,5r,7r)-4'-methoxyspiro[adamantane-2,3'-[1,2]dioxetan]-4'-yl)phenyl-trifluoro-methanesulfonate, was first synthesized (Scheme 5), and the chemical structures were confirmed by ^{1}H NMR spectra (Figure 12 and 13). SPNRs were preparation *via* nanoprecipitation of caged chemiluminescence dioxetanes and the respective SP in the presence of an amphiphilic triblock copolymer (PEG-*b*-PPG-*b*-PEG). Three SPs including PFPV, PFBT, and PFODBT were used for the preparation of SPNRs, affording the water-soluble nanoparticles termed as SPNR1, SPNR2 and SPNR3, respectively. The doping amount ratio of the chemiluminescence dioxetanes to the SP in each SPNR was fixed at 1/40, wherein the chemiluminescence signal was optimized to be maximum. In addition, quantum yield of SPNR3 with different doping amount were calculated as 0.695 ± 0.014, showing no significant difference with PEG-*b*-PPG-*b*-PEG encapsulated PFODBT nanoparticle without chemiluminescence substrate doping (0.721).

$O_2^{\bullet-}$ is a primary ROS and severs as a third signal for activation of helper T cells (CD4$^+$ T cell) and cytotoxic T cells (CD8$^+$ T cells).[127] $O_2^{\bullet-}$ thus can be used as the immunoactivation biomarker. SPNRs consist of a SP and a custom-designed $O_2^{\bullet-}$-responsive chemiluminescence substrate (Figure 14a and 14b). The chemiluminescence substrate is a dioxetane derivative whose phenol is caged with a $O_2^{\bullet-}$-cleavable trifluoromethanesulfonate (Tf) group to inhibit its activity.[128] Upon specific reaction with $O_2^{\bullet-}$, the sulfonate ester of caged dioxetanes within SPNRs is specifically cleaved to induce the deprotection of Tf group, resulting in the formation of high-energy unstable phenolate-dioxetane derivatives. Subsequently, intraparticle chemiluminescence resonance energy transfer (iCRET)[83] from the unstable derivatives to the SP occurs, leading to the generation of chemiluminescence signals at the long wavelength range of the SP (Figure 14c). In particular, SPNR3 emits chemiluminescence at 700 nm and represents the first NIR chemiluminescent molecule responding to $O_2^{\bullet-}$.[129]

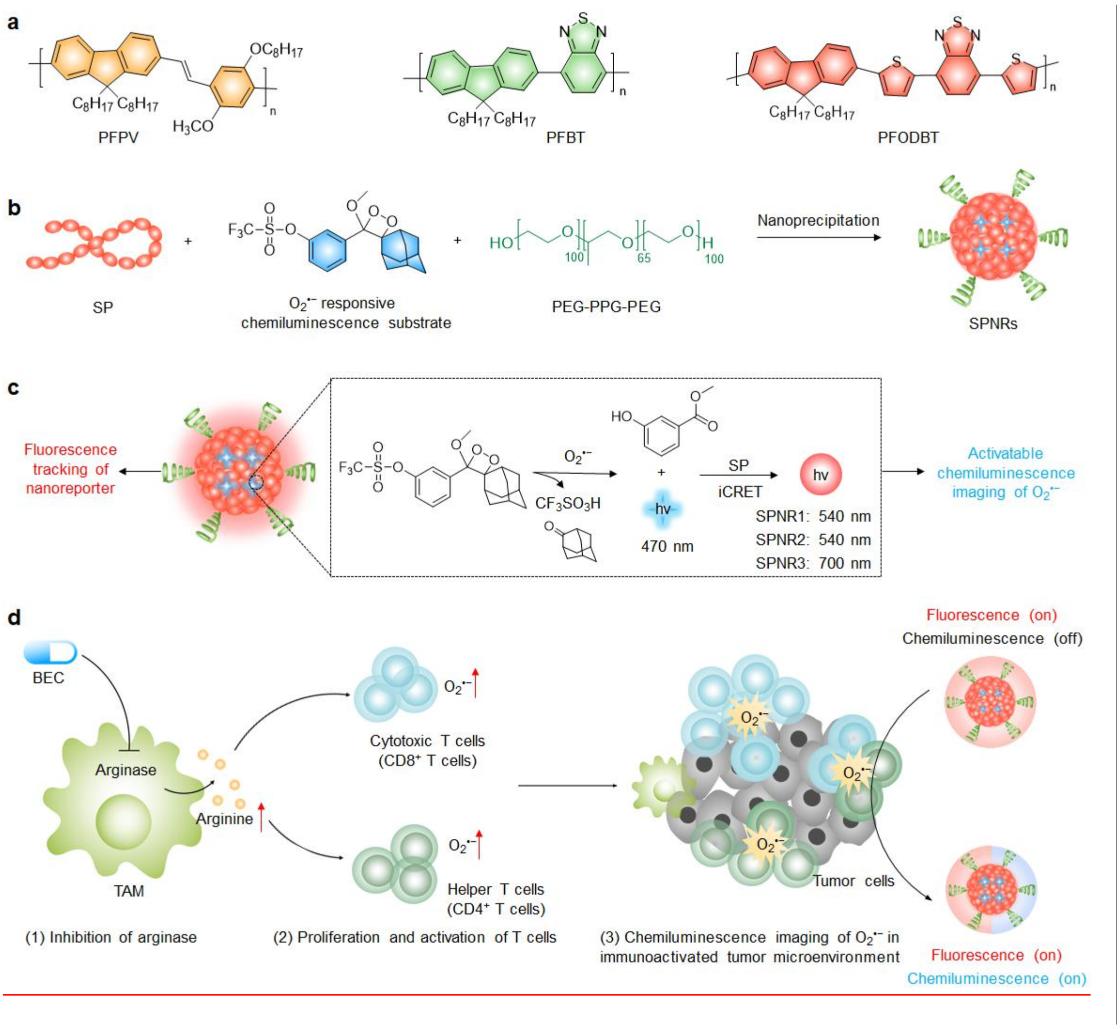

Figure 14. Preparation of SPNRs for chemiluminescence imaging of immunoactivation. a) Chemical structures of SPs (PFPV, PFBT and PFODBT). b) Schematic illustration of the preparation of SPNRs *via* nanoprecipitation. c) Illustration of the mechanism of $O_2^{\bullet-}$ activated chemiluminescence of SPNRs. d) Illustration of *in vivo* chemiluminescence imaging of $O_2^{\bullet-}$ in tumors after drug-induced immunoactivation.

The ideal nanoreporter (SPNR3) with a NIR luminescence is tested for *in vitro* detection of $O_2^{\bullet-}$ in different cell lines and *in vivo* chemiluminescence imaging of drug-induced immunoactivation. The NIR "always-on" fluorescence and $O_2^{\bullet-}$ activatable chemiluminescence of SPNR3 enables tracking of the reporter location and evaluation of $O_2^{\bullet-}$ levels, respectively. In this case, S-(2-boronoethyl)-L-cysteine hydrochloride (BEC) an immunotherapeutic drug, is used as an example, which is known to inhibit the activity of arginase in tumor microenvironment and thus promotes the proliferation and activation of helper T cells and cytotoxic T cells.[130] Abundant helper T cells and cytotoxic T cells in tumor tissues produce high levels of $O_2^{\bullet-}$, which specifically activate chemiluminescence signal of SPNR3, allowing for real-time imaging of immune response in mouse models.

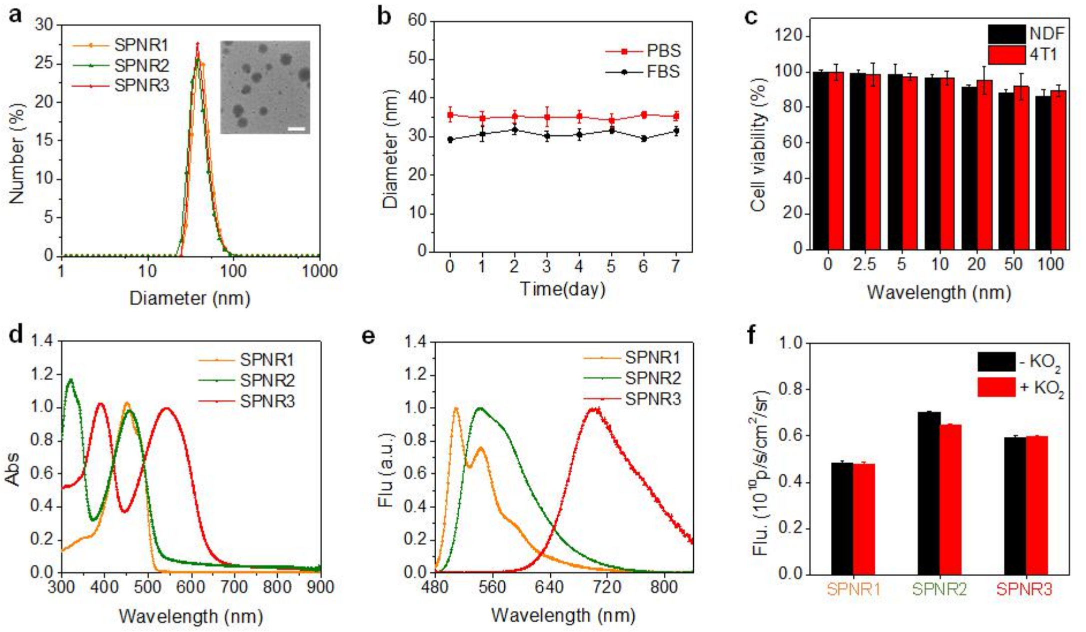

Figure 15. Characterization of SPNRs. a) DLS data of SPNR1, SPNR2 and SPNR3 in PBS buffer (pH = 7.4). Inset is the TEM image of SPNR3 (Scale bar = 50 nm). b) DLS data of SPNR3 as a function of time incubated with PBS (pH = 7.4) and FBS. c) Cell viability of NDF/4T1 cells after incubation with SPNR3 at different concentrations. d) UV-vis absorption and e) fluorescence spectra of SPNR1, SPNR2 and SPNR3 in PBS (20 μg mL^{-1}). f)

Quantification of FL intensities of SPNR1, SPNR2 and SPNR3 (20 μg/mL) with or without $O_2^{\bullet-}$ (40 μM) treatment in PBS. Error bars represent SDs of three separate measurements (n = 3)

The physical and optical properties of SPNRs were studied in PBS (pH = 7.4). DLS measurement showed that the average hydrodynamic diameters of the three SPNRs were similarly ranged from 30 to 40 nm (Figure 15a). TEM image showed that SPNR3 possessed a uniform spherical morphology with an average diameter of ~35 nm (Figure 15a), which was close to the DLS data. No precipitation or obvious change in size was observed for SPNR3 after storage in PBS (pH = 7.4) or fetal bovine serum (FBS) for 7 days (Figure 15b). Note that the cell viability of NDF/4T1 cancer cells after incubation with SPNR3 was good, suggesting its negligible cytotoxicity even at a high concentration of 100 μg/mL (Figure 15c). The absorption (Figure 15d) and fluorescence spectra (Figure 15e) showed that SPNR1, SPNR2 and SPNR3 had the maximum absorption peaks at 450, 460 and 580 nm, respectively; while their maximum emission peaks at 520, 540 and 700 nm, respectively.

The chemiluminescence spectra of SPNRs were measured after addition of excessive KO_2 into the nanoreporter solutions. Note that no obvious chemiluminescence signals were observed for SPNRs in the absence of $O_2^{\bullet-}$. In the presence of $O_2^{\bullet-}$, the maximum chemiluminescence signals were observed at 540, 540 and 700 nm for SPNR1, SPNR2 and SPNR3, respectively (Figure 16a, 16b, and 16c), and the spectral profiles of chemiluminescence were similar to their respective fluorescence spectra (Figure 15e). The chemiluminescence images of SPNR solution acquired by IVIS spectrum imaging system also confirmed the activation of chemiluminescence signals after adding $O_2^{\bullet-}$, showing the chemiluminescence intensity increase by 300-, 500- and 490-fold for SPNR1, SPNR2 and SPNR3, respectively. However, the fluorescence intensities of the SPNRs remained nearly unchanged after adding $O_2^{\bullet-}$ (Figure 15f), proving the stability of SPs in the presence of ROS. These results suggested that $O_2^{\bullet-}$ could specifically activate the chemiluminescence signals of SPNRs without affecting the FL emission.

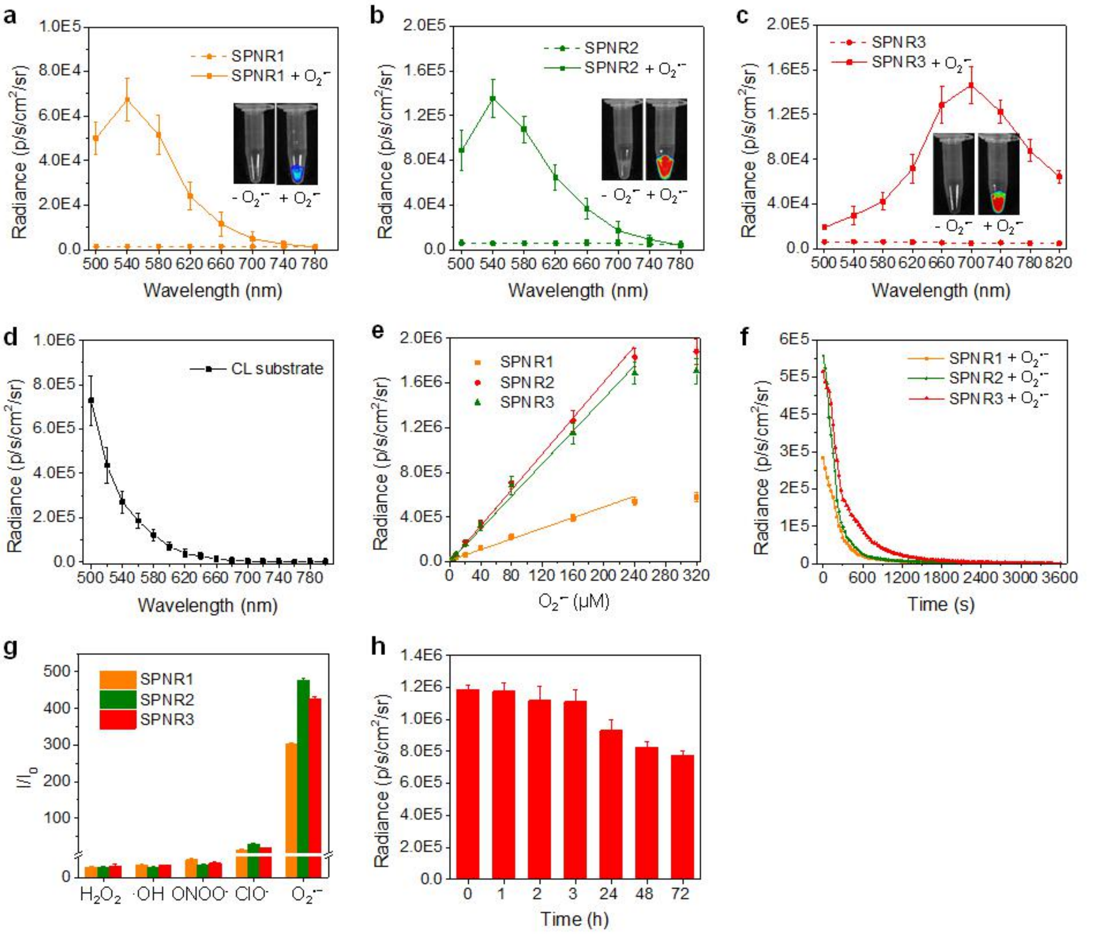

Figure 16. Chemiluminescent characterization of SPNRs. Chemiluminescence spectra of a) SPNR1, b) SPNR2, and c) SPNR3 (20 μg mL^{-1}) in the absence or presence of $O_2^{\bullet-}$ (40 μM) in PBS (pH = 7.4). Insets are chemiluminescence images of the corresponding SPNR with or without $O_2^{\bullet-}$. d) Chemiluminescence spectra of chemiluminescence substrate (20 μg mL^{-1}) after treated with $O_2^{\bullet-}$ for 5 s. e) Chemiluminescence intensities of SPNR1, SPNR2 and SPNR3 as a function of $O_2^{\bullet-}$ concentrations (0, 2, 4, 8, 20, 40, 80 and 160 μM). f) Decay of

chemiluminescence intensities of SPNRs in the presence of $O_2^{\bullet -}$ (20 μM). g) The ratios of chemiluminescence intensity of SPNRs (20 μg mL^{-1}) after incubation with indicated ROS (40 μM) to that without ROS in PBS buffer (pH = 7.4) at 37 °C for 5 s. h) Chemiluminescence intensities of SPNR3 incubation in FBS at various time points (1, 2, 3, 24, 48, 72 h). Error bars represent SDs of three separate measurements (n = 3).

The mechanism of activation of chemiluminescence signal for SPNRs was proposed as shown in Figure 14c. Upon reaction with $O_2^{\bullet -}$, deprotection of Tf group of the chemiluminescence substrate occurred within nanoparticles, following by the formation of a highly unstable phenolate-dioxetane derivative. This intermediate underwent a spontaneous decomposition and released photons with the wavelength at 470 nm (Figure 16d). Then, iCRET happened due to the overlap between the absorption of SPs and the emission of the chemiluminescence substrate, leading to the chemiluminescence signals at the emission wavelength of SPs.

The sensitivity and selectivity of SPNR1, SPNR2 and SPNR3 for chemiluminescence detection of $O_2^{\bullet -}$ were studied in solution. In the presence of $O_2^{\bullet -}$ with the concentrations ranging from 0 to 160 μM, a good linearity between the chemiluminescence intensity and $O_2^{\bullet -}$ concentration was observed for all nanoreporters (Figure 16e), showing their feasibility for quantification of $O_2^{\bullet -}$. According to these curves, the limits of detection (LODs) of SPNR1, SPNR2 and SPNR3 were calculated to be 13.8, 11.3 and 11.8 nM, respectively. The chemiluminescence half-life of all SPNRs was measured to be ~3 min at room temperature, which was long enough for real-time imaging acquisition (Figure 16f). In addition, all SPNRs showed negligible chemiluminescence responses to other

ROS including H_2O_2, hydroxyl radicals (•OH), peroxynitrite ($ONOO^-$) and hypochlorite (ClO^-) (Figure 16g), validating their high selectivity towards $O_2^{\bullet-}$. The chemiluminescence intensity of SPNR3 remain 67 % after incubation in FBS for 72 h, indicating that SPNR3 has good stability under physiological condition (Figure 16h). Because SPNR3 had the NIR fluorescence and chemiluminescence with minimized tissue autofluorescence and enhanced tissue penetration depth relative to SPNR1 and SPNR2, allowing it for the following *in vitro* and *in vivo* imaging experiments.

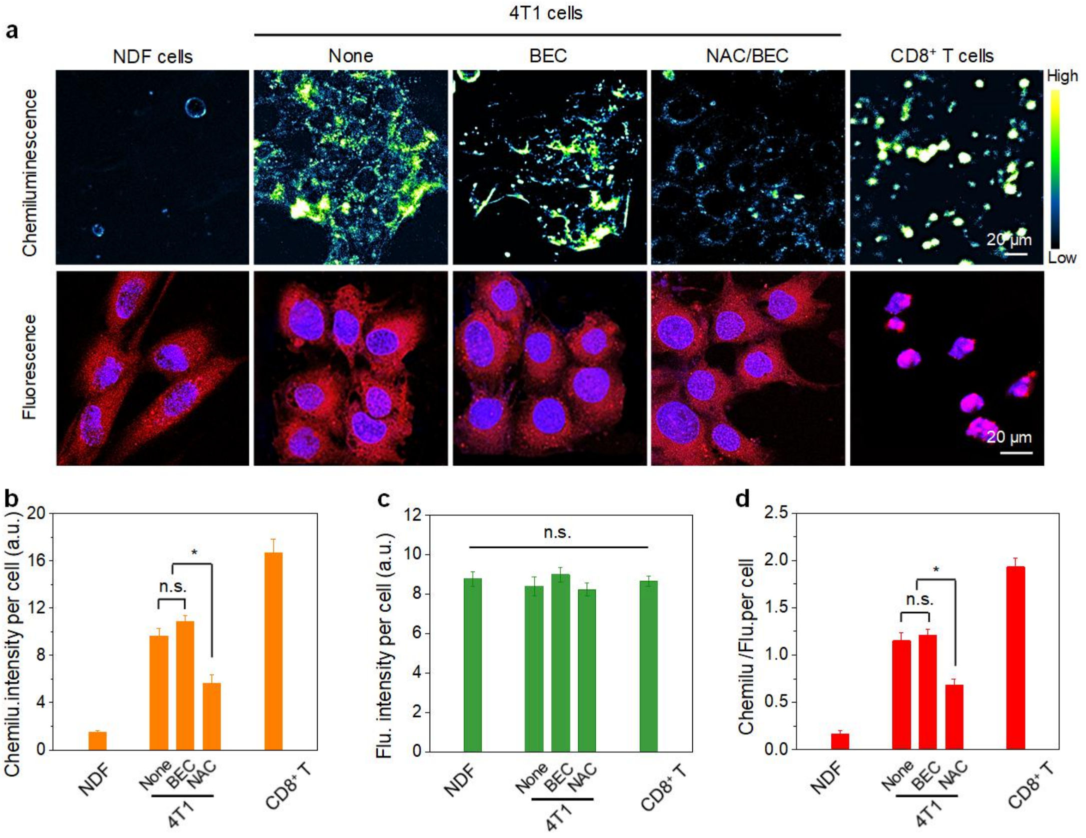

Figure 17. *In vitro* chemiluminescence imaging of intracellular $O_2^{\bullet-}$ in NDF cells, 4T1 cancer cells, and cytotoxic T cells. a) Chemiluminescence and fluorescence images of SPNR3 treated NDF cells, 4T1 cancer cells, and cytotoxic T cells (floating cells) with or without pretreatments of BEC (100 mM) for 2 h and NAC (100 mM) for 0.5 h. For confocal fluorescence microscopy

images, the cell nuclei were stained with 4,6-diamidino-2-phenylindole (DAPI) and indicated in blue. Mean chemiluminescence b) and fluorescence c) intensity of single cell in Figure 17a. d) The chemiluminescence/fluorescence intensity ratio of treated cells (n = 3, *p < 0.05, n.s.: not significant).

The feasibility of SPNR3 for detection of intracellular endogenous $O_2^{\bullet-}$ was tested in different cell lines including normal dermal fibroblasts (NDF), 4T1 cancer cells, and cytotoxic T cells ($CD8^+$ T cells). After incubation with SPNR3, intense NIR fluorescent signals assigned to PFODBT were detected in all the cell lines (Figure 17a) with nearly the same fluorescence intensities (Figure 17b), suggesting the similar cellular uptake of SPNR3 by these cell lines. $CD8^+$ T cells appeared to be spherical in these images due to the fact that they are floating cells. In contrast, obvious chemiluminescence signals from SPNR3 were only observed in 4T1 cancer cells and cytotoxic T cells but not for NDF cells. The 4T1 cancer cells and cytotoxic T cells showed a 5.1- and 9.1-fold higher chemiluminescence intensity relative to NDF cells, respectively (Figure 17c). In addition, the chemiluminescence/fluorescence intensity ratios of the treated cells showed a similar tendency to the chemiluminescence intensities (Figure 17d). These results indicated that 4T1 cancer cells, and $CD8^+$ T cells had high intracellular $O_2^{\bullet-}$ levels relative to normal cells. This is consistent with the fact that cancer cells are known to have increased ROS production mainly because of activation of oncogenes, metabolic aberrance, mitochondrial dysfunction and loss of functional P53.[131] However, the $O_2^{\bullet-}$ level in cytotoxic T cells was higher than that in 4T1 cancer cells, because $O_2^{\bullet-}$ is required for activation of cytotoxic T cells and subsequent production of cytokines.[132] Thus, this results further confirmed that $O_2^{\bullet-}$ could be used as the biomarker to track immunoactivation in the course of cancer immunotherapy.

To test the ability of SPNR3 to sense the variation of endogenous $O_2^{\bullet-}$ level, 4T1 cancer cells were treated with (100 mM) or N-acetyl L-cysteine (NAC, 100 mM). NAC is an antioxidant drug that can efficiently enter cells to scavenge ROS to prevent oxidative stress.[133] The chemiluminescence signal of BEC-treated 4T1 cancer cells was almost the same to that of untreated cells (Figure 17a, 17b), confirming that BEC had no influence on the intracellular $O_2^{\bullet-}$ levels in cancer cells. However, after treatment of NAC, the chemiluminescence signals of 4T1 cancer cells sharply decreased. The fluorescence intensities of BEC-treated cells and NAC-treated cells remained the same as the control (Figure 17c). These results not only validated that SPNR3 was able to detect the small change in endogenous $O_2^{\bullet-}$ level but also revealed that BEC treatment barely affected the intracellular $O_2^{\bullet-}$ level of 4T1 cancer cells.

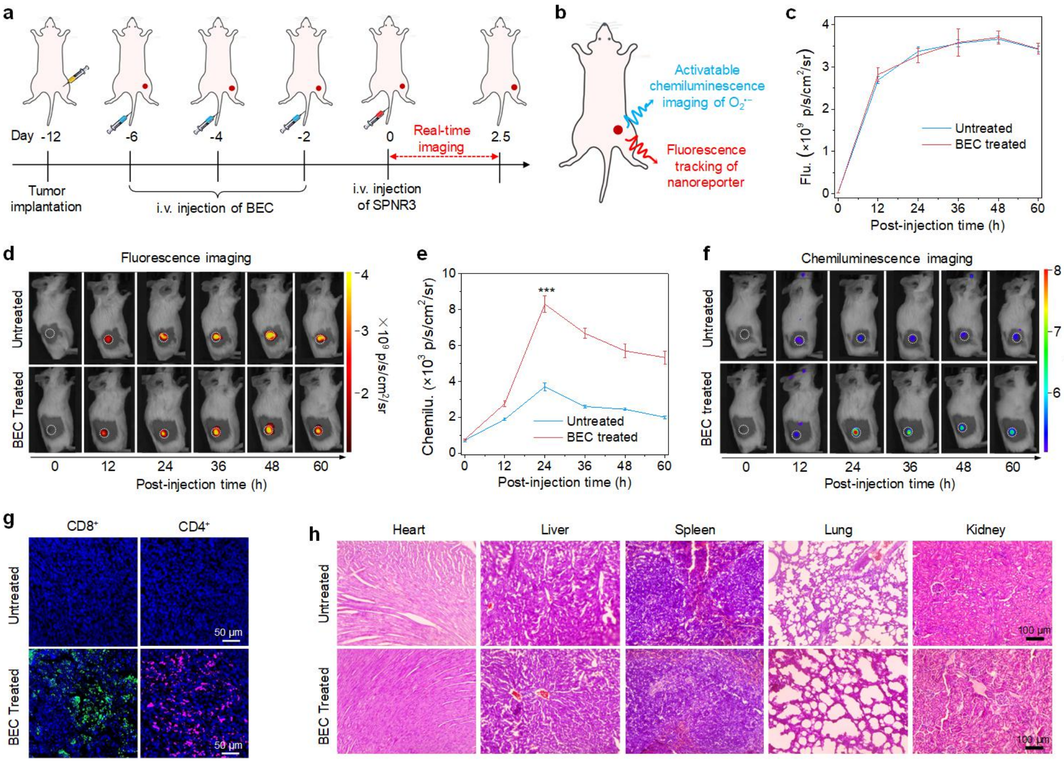

Figure 18. *In vivo* chemiluminescence imaging of $O_2^{\bullet-}$ in the tumors of living mice after BEC-mediated immunotherapy. a) Schematic illustration of establishment of tumor model, BEC treatment, and imaging procedure. b) Schematic illustration of chemiluminescence imaging of $O_2^{\bullet-}$ and fluorescence tracking of SPNR. c) Fluorescence intensities of tumors as a function of post-injection time of SPNR3 in untreated or BEC-pretreated mice (n = 3). d) NIR fluorescence imaging of untreated and BEC-pretreated 4T1 tumor-bearing BALB/c mice at different timepoints after intravenous injection of SPNR3 (200 μL, 500 μg mL^{-1}). e) Chemiluminescence intensities of tumors as a function of post-injection time of SPNR3 in untreated or BEC-pretreated mice (***$p < 0.001$, n = 3). f) Chemiluminescence imaging of untreated and BEC-pretreated 4T1 tumor-bearing mice at different timepoints after the intravenous injection of SPNR3 (200 μL, 500 μg mL^{-1}). g) Confocal fluorescence microscopy images of CD8 and CD4 staining of tumor tissues from untreated and BEC-pretreated tumor-bearing mice after real-time imaging. Blue indicates the cell nucleus stained with DAPI, green indicates the signal of CD8 staining and purple indicates the signal of CD4 staining. h) H&E staining of the major organs including heart, liver, spleen, lung and kidney extracted from untreated and BEC-pretreated tumor-bearing mice after *in vivo* imaging.

To evaluate the capability of SPNR3 for *in vivo* chemiluminescence imaging of $O_2^{\bullet-}$ after immunotherapy, 4T1 tumor-bearing BALB/c mouse model was established by subcutaneously implanting 4T1 cancer cells into the right flank of mouse (Figure 18a). BEC was intravenously injected into the mice every two days for three time to induce immunoactivation, and then SPNR3 was intravenously injected for NIR fluorescence tracking and activatable chemiluminescence imaging of $O_2^{\bullet-}$ (Figure 18b). After SPNR3 injection, fluorescence signals in the tumor tissues gradually increased and reached the similar maximum at 48 h post-injection time for both untreated and BEC-pretreated mice (Figure 18c and 18d). This suggested the similar accumulation of SPNR3 in the tumor for these mice, which should be attributed to the enhanced EPR effect due to its small size (35 nm) and PEG-passivated surface. Similarly, the *ex vivo* fluorescence data confirmed that SPNR3 had similar biodistribution in untreated and BEC-pretreated living mice, and their major accumulation was observed in the tumor, spleen and liver. On the other hand, the chemiluminescence signals of tumors for both untreated and BEC-pretreated mice gradually increased after SPNR3 injection and reached the maximum at 24 h post-injection time (Figure 18e and 18f). However, the chemiluminescence intensity of tumors for BEC-pretreated mice was much higher than that for untreated mice at each time point (Figure 18e and 18f). In particular, at 24 h post-injection of SPNR3, the chemiluminescence intensity of tumors for BEC-pretreated mice was 2.2-fold higher than that for untreated mice. Because the accumulation of SPNR3 in untreated and BEC-pretreated living mice are nearly the same during the imaging process, such increased chemiluminescence signal of SPNR3 should be solely attributed to the increased $O_2^{\bullet-}$ levels in the tumors of living mice after immunotherapy.

To verify if the increased chemiluminescence signals were associated with the BEC-induced activation of immune response, population of T cells in tumor tissues was investigated using immunofluorescence staining. Both distinct cytotoxic T cells ($CD8^+$ T cells, pseudo-green signal) and helper T cells ($CD4^+$ T cells, pseudo-purple signal) were found to distribute in the tumors of BEC-pretreated mice (Figure 18g). In contrast, few cytotoxic T cells or helper T cells were observed in the tumors of untreated mice. Thus, it confirmed that BEC promoted the proliferation and activation of helper T cells and cytotoxic T cells. Abundant T cells in tumor produced high levels of $O_2^{\bullet-}$, leading to increased chemiluminescence signal of SPNR3. Therefore, the chemiluminescence signal of SPNR3 is correlated well with the immunoactivation in the tumor of living mice.

To evaluate the biosafety of SPNR3, the major organs including heart, liver, spleen, lung, and kidney of tumor-bearing mice after imaging were extracted and used for H&E staining. In both untreated and BEC-pretreated mice after an intravenous injection of SPNR3, all these organs displayed normal histology and no damaged regions were observed (Figure 18h), suggesting the good biocompatibility of SPNR3.

4.4 Conclusion

In summary, we have successfully synthesized a class of chemiluminescent nanoreporter (SPNRs) that can detect $O_2^{\bullet-}$ for real-time *in vivo* chemiluminescence imaging of drug-induced cancer immunoactivation. Due to the efficient iCRET, SPNR3 selectively turned on its NIR chemiluminescence signal at 700 nm by 490-fold in the presence of $O_2^{\bullet-}$, showing a LOD as low as 11.8 nM. Such a high selectivity and sensitivity allowed SPNR3 to act as an intracellular nanoreporter to detect the levels of endogenous $O_2^{\bullet-}$ in different cell lines, revealing that cytotoxic T cell has higher endogenous $O_2^{\bullet-}$ level than cancer and normal cells. More importantly, SPNR3 had preferential accumulated in the tumor of living mice after systemic administration, and could turn on the chemiluminescence signals to report the $O_2^{\bullet-}$ level related to the populations of activated cytotoxic T cells and helper T cells in the course of cancer immunotherapy. Thus, this study introduces the first kind of organic chemiluminescent nanoreporters (to the best of our knowledge) that can be used for real-time *in vivo* imaging of cancer immunotherapy and for high throughput screening of immunotherapeutics.

5. SPN-photosensitizer conjugated polymer for Tumor Metastasis Imaging

5.1 Background

Cancer metastasis with its complex cell-biological mechanism, systemic nature, and drug resistance, is the main cause of recurrence and death of most cancer patients.[134] Early diagnosis of metastases thus plays a critical role in the effective treatment of cancer. Radiologic imaging approaches such as MRI, CT, ultrasound, and PET have been used for the diagnosis of tumor metastases.[135] For example, the combination of multiple imaging (CT/PET) has been explored for the detection of tumor metastasis in lymph nodes,[136] and MRI in association with pH-responsive nanoparticles as contrast agents has been used for the detection of liver metastasis.[137] However, because of limited resolution of PET and high potential of false positive signal of MRI, current methods relatively have low specificity and sensitivity.[138]

As an emerging molecular optical imaging method, due to the elimination of real-time light excitation, afterglow or persistent luminescence has attracted much attention for its low background, high SBR and high sensitivity.[139] Generally, afterglow luminescence is caused by the slow release of photons from energy traps in the materials upon thermal stimulation. However, only a few kinds of inorganic nanoparticles doped with rare-earth metals or heavy metals such as europium, praseodymium, and chromium have the ability to emit afterglow signal,[140] and they have been tested for tumor imaging,[141] vascular imaging,[142] *in vivo* cell tracking,[143] and cell targeting.[144] However, these inorganic afterglow nanoparticles have not been exploited for imaging of metastatic tumor tissues in living mice, because of inorganic afterglow nanoparticles limited targeting ability, and they are currently used as accumulation probes. Therefore, contrast is determined by the probe concentration between target tissue and adjacent normal tissue. Moreover, these inorganic contrast agents have the disadvantages of low brightness, short luminescence time and toxicity.

Many biocompatible organic nanoparticles with long lifetime and high brightness have been developed for *in vivo* afterglow imaging applications.[145] After screening many SPs, we found that MEHPPV with strong electron-donating substituents could afford high afterglow amplitude.[146] The mechanism was described as follows: light irradiation of PPVs generated $^1O_2$ that reacted with the vinylene bond to form an unstable dioxetane intermediate, follow by spontaneously degrading into a PPV aldehyde to produce luminescence in visible light region. With 5% amount of 2,3-naphthalocyanine bis(trihexylsiyloxide) (NCBS) doping, SPN-NCBS displayed the highest afterglow intensity due to the increased generation of $^1O_2$ by NCBS, and modulation of the emission into the NIR optical window through the energy transfer, allowed a high penetration depth and contrast afterglow imaging of lymph nodes and tumors in living mice.[146]

We herein report the design and synthesis of PPVs incorporated with a NIR photosensitizer for in vivo afterglow imaging of metastatic tumors in living mice. TPP is used as the NIR photosensitizer and is copolymerized into the polymers, leading to red-shifted emission and relatively small size (~ 25 nm). Moreover, because the afterglow intensity is determined by the amount of high-energy intermediate PPV-dioxetane generated from the $\pi^2 - \pi^2$ cycloaddition reaction between the vinylene bonds and $^1O_2$ incorporation of TPP promotes $^1O_2$ generation and thus amplifies afterglow. In the following, we describe the synthesis of TPP-incorporated PPVs and the preparation of hydrophilic nanoparticles, followed by the analysis of their optical and afterglow luminescence properties. At last, the proof-of concept applications are demonstrated for *in vivo* hypoxia imaging and *in vivo* imaging of metastatic tumors.

5.2 Methods

Synthetic route

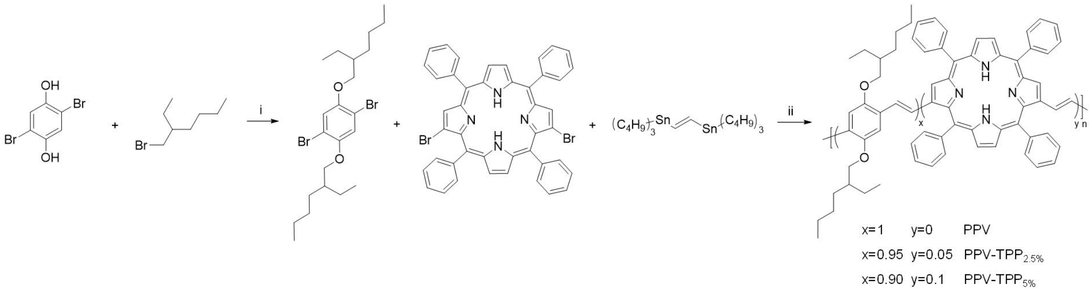

Scheme 6. Synthetic route of PPV-TPPs. i). K_2CO_3, DMF, 80 °C, 12 h; ii) tris(dibenzylideneacetone) dipalladium(0) [$Pd_2(dba)_3$], tri(*p*-toyl)phosphine, chlorobenzene, 100 °C, 24 h.

Synthesis of 1,4-Dibromo-2,5-bis((2-ethylhexyl)oxy)benzene. 2,5-Dibromo-hydroquinone (500 mg, 1.87 mmol), K_2CO_3 (780 mg, 5.61 mmol), and dimethylformamide were added to a 50 mL round-bottomed flask, followed by 3-(bromomethyl)heptane (0.8 mL, 4.58 mmol) addition. The mixture was carried out at 80 °C for 12 h. The product was cooled to room temperature and extracted with DCM. The organic layer was washed with water/brine and dried over anhydrous Na_2SO_4. The solvent was removed under vacuum, and the crude was purified via column chromatography over silica/hexane, yielding 1,4-dibromo-2,5-bis((2-ethylhexyl)oxy)benzene (697.5 mg, 76.3% yield) as a pale viscous oil. ^{1}H NMR (300 MHz, $CDCl_3$) δ 7.08 (s, 2H), 3.82 (d, *J* = 5.6 Hz, 4H), 1.73 (dd, *J* = 12.1, 6.0 Hz, 2H), 1.61–1.20 (m, 16H), 0.93 (t, *J* = 7.5 Hz, 12H).

General Procedure for Synthesis of PPV–TPP. 1,4-Dibromo-2,5-bis((2-ethylhexyl)oxy)benzene,7,18-dibromo-5,10,15,20-tetraphenylporphyrin,trans-1,2-bis (tributylstannyl)ethene, tris(dibenzylideneacetone) dipalladium(0), and tri(*p*-toyl)phosphine were added to a 50 mL Schlenk tube, followed by chlorobenzene addition via syringe (degassed). The tube was charged with argon through freeze−pump thaw cycles for three times. The reaction was carried out at 100 ° C under vigorous stirring for 24 h. The mixture was cooled to room temperature and the solvent was removed under vacuum. The crude product was poured into methanol and the obtained brown solid was washed with methanol for three times. *PPV*: ^{1}H NMR (300 MHz, $CDCl_3$) δ 7.46 (s, 1H), 7.12 (d, *J* = 21.9 Hz, 2H), 3.95 (t, *J* = 29.7 Hz, 4H), 3.40 (s, 1H), 1.89 (s, 2H), 1.30 (d, *J* = 26.2 Hz, 3H), 0.90 (s, 4H). *PPV–TPP*$_{2.5\%}$: ^{1}H NMR (300 MHz, $CDCl_3$) δ 8.22 (s, 1H), 7.77 (s, 2H), 7.42 (d, *J* = 25.4 Hz, 4H), 7.12 (d, *J* = 18.6 Hz, 4H), 4.03 (d, *J* = 30.0 Hz, 7H), 3.43 (d, *J* = 6.7 Hz, 8H), 1.90 (s, 14H), 1.26 (s, 6H), 0.96–0.69 (m, 5H). *PPV–TPP*$_{5\%}$: ^{1}H NMR (300 MHz, $CDCl_3$) δ 8.21 (s, 1H), 7.77 (s, 1H), 7.49 (s, 2H), 7.23−6.97 (m, 2H), 3.95 (t, J = 31.0 Hz, 4H), 3.28 (s, 1H), 1.96 (d, J = 47.6 Hz, 2H), 1.62 (d, J = 34.3 Hz, 6H), 1.27 (t, J = 18.3 Hz, 5H), 1.08–0.67 (m, 5H).

Preparation of SPNs. PPV-TPPs (1 mg) were dissolved in 1 mL of THF. Then 0.25 mL of PPV-TPP THF solution and PEG-b-PPG-b-PEG (20 mg) were added into 0.75 mL of THF. The obtained solution was rapidly injected into a mixture of DI water (9 mL) and THF (1 mL) under continuous sonication. Then THF was removed by a gentle nitrogen flow. The resulting solution was purified by filtration through a 0.22 μm polyvinylidene fluoride syringe driven filter (Millipore). The obtained nanoparticles solutions were concentrated through ultrafiltration and then diluted by 1 × PBS (pH = 7.4) to prepare solutions of different concentrations.

Characterization. GPC was conducted by a Shimadzu LC-VP system with polystyrenes as the standard and HPLC grade THF as the eluent. NMR spectroscopy was recorded on a BRUKER Avance 300 NMR (1H, 300 MHz) system with $CDCl_3$ or D_2O as the solvent. The spectrum was internally referenced to the tetramethylsilane signal at 0 ppm. Afterglow signals and images were collected and obtained with the IVIS spectrum imaging system under bioluminescence (without excitation) mode.

In Vitro Fluorescence and Afterglow Measurement. Fluorescence and afterglow luminescence images, fluorescence and afterglow spectra were acquired by using an IVIS Spectrum imaging system. Fluorescence images were acquired for 0.1 s with excitation at 465 ± 10 nm or 430 ± 10 nm, and emission at 520 ± 20 nm or 720 ± 20 nm. For afterglow luminescence imaging, samples were pre-irradiated by white light for 1 min at a power density of 1 W cm^{-2}.

Animals and Tumor Mouse Model. To establish tumor-bearing mouse model, 4T1 cell suspension (200 µL, 1 × 10^6) was injected subcutaneously in the left shoulder of the nude mice. Tumors were grown for approximately 7 days before imaging experiments. To establish the peritoneal metastases mouse model, 4T1 cell suspension (200 µL, 4 × 10^5) was injected intraperitoneally into nude mice. Tumors were grown for approximately 4 days before imaging experiments.

In Vivo Imaging for Differentiating Hypoxia and Normoxia Environment. After anesthesia, pre-implanting tumor in the left shoulders of nude mice (n=2) were injected in situ with 50 µL of SPN2.5 (100 µg/mL, oxygen was removed via purging the solution with nitrogen). The same SPN2.5 solution was injected subcutaneously in the right shoulder of these mice. The fluorescence images of the mice were acquired at 720 nm upon excitation at 500 nm with the IVIS Spectrum imaging system. After pre-irradiated with white light for 1 min, the afterglow luminescence images of the mice were obtained with a 30s acquisition time under the IVIS Spectrum imaging system bioluminescence (open filter) mode.

*Peritoneal Metastatic Tumor Imaging***.** The healthy mice were injected intravenously with 200 µL of SPN2.5 (400 µg/mL). The mice bearing the 4T1 intraperitoneal metastases were injected intravenously with 200 µL of SPN2.5 (400 µg/mL). At different post injection time point (0 h, 20 min, 40 min, 1 h, 2 h, 4 h), the fluorescence images of the mice were acquired at 720 nm upon excitation at 500 nm, while the afterglow luminescence images were then acquired with a 30s acquisition time with an open filter after irradiated with white light for 1 min. The mice were euthanized at 4 h post-injection, and the fluorescence and afterglow luminescence images of the organs and tumors with skin and peritoneum removed were acquired by applying the same method described above. Fluorescence and afterglow luminescence images were analyzed by ROI analysis using the Living Image 4.0 Software.

Histological Analysis. To confirm the peritoneal metastatic tumor cells, the mice were euthanized and the tumors (tissues) were extracted and fixed in 4% paraformaldehyde. The tumors (tissues) were then embedded in paraffin S15 and cut into sections with a thickness of 10 μm for H&E staining according to the standard protocols. Images of stained slices were captured by a Nikon ECLIPSE 80i microscope (Nikon Corporation, Towa Optics, New Delhi, India).

Statistical Analysis. The fluorescence and afterglow luminescence images were quantified with ROI analysis using Living Image 4.0 Software. Results were expressed as the mean ± standard deviation (SD) deviation ($n = 3$) unless otherwise stated. Statistical comparisons between two groups were determined by Student t-test. For all tests, $p < 0.05$ ($n = 3$) was considered as statistically significant. All statistical calculations were performed using GraphPad Prism v.6 (GraphPad Software Inc., CA, USA).

5.3 Results and Discussions

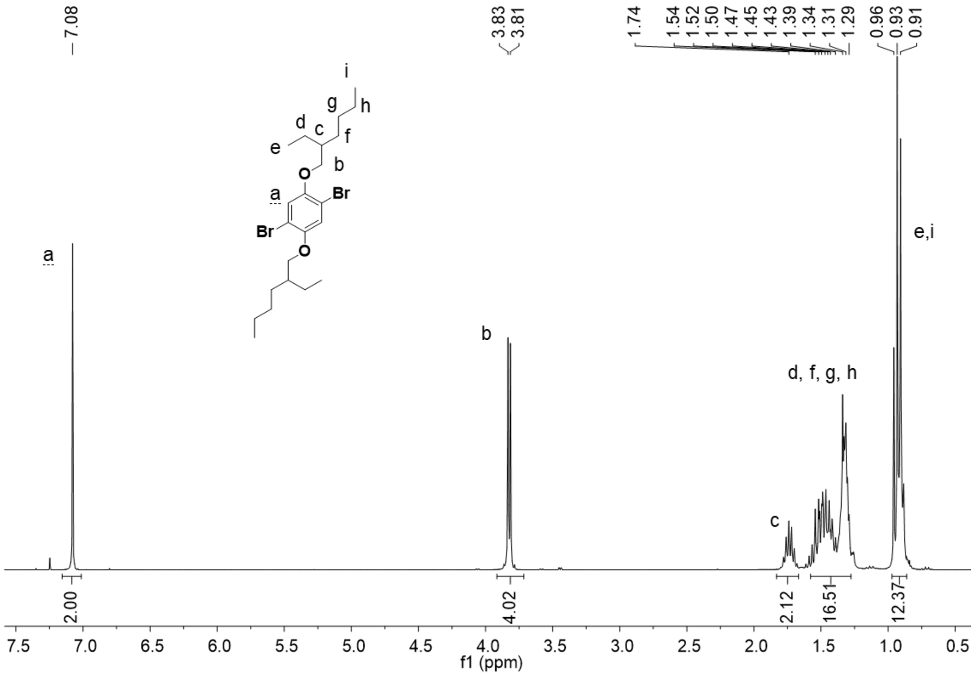

Figure 19. ^{1}H NMR spectra of monomer in CDCl$_3$.

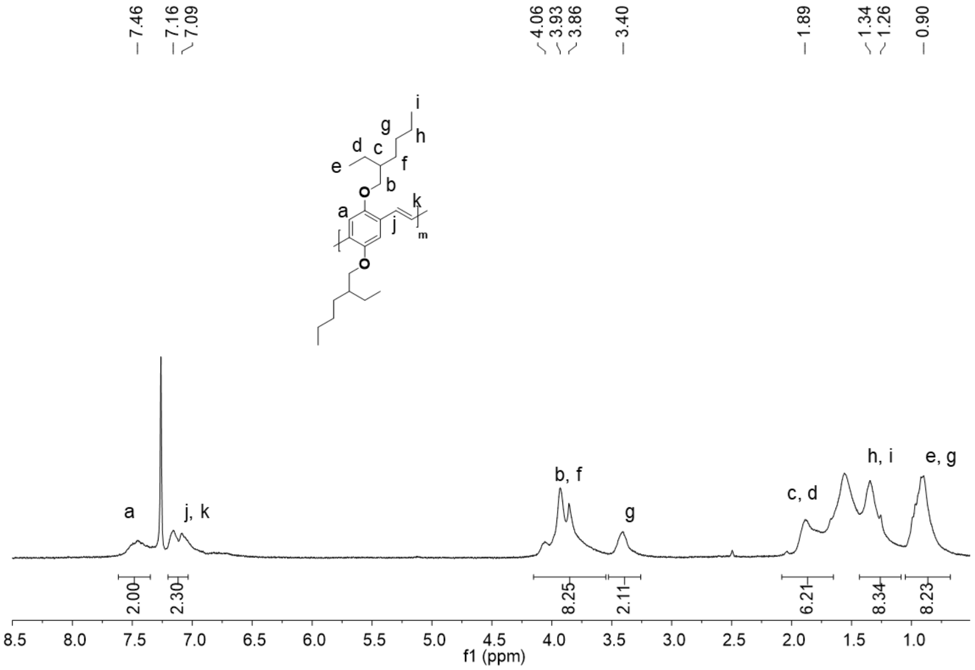

Figure 20. ^{1}H NMR spectra of PPV in CDCl$_3$.

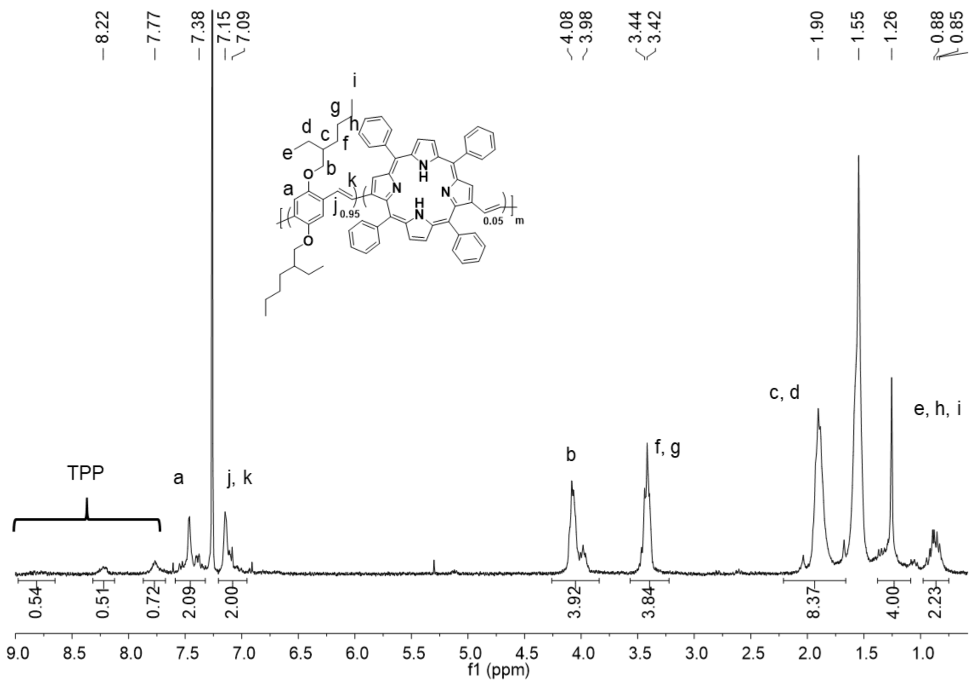

Figure 21. ^{1}H NMR spectra of PPV-TPP2.5% in CDCl$_3$.

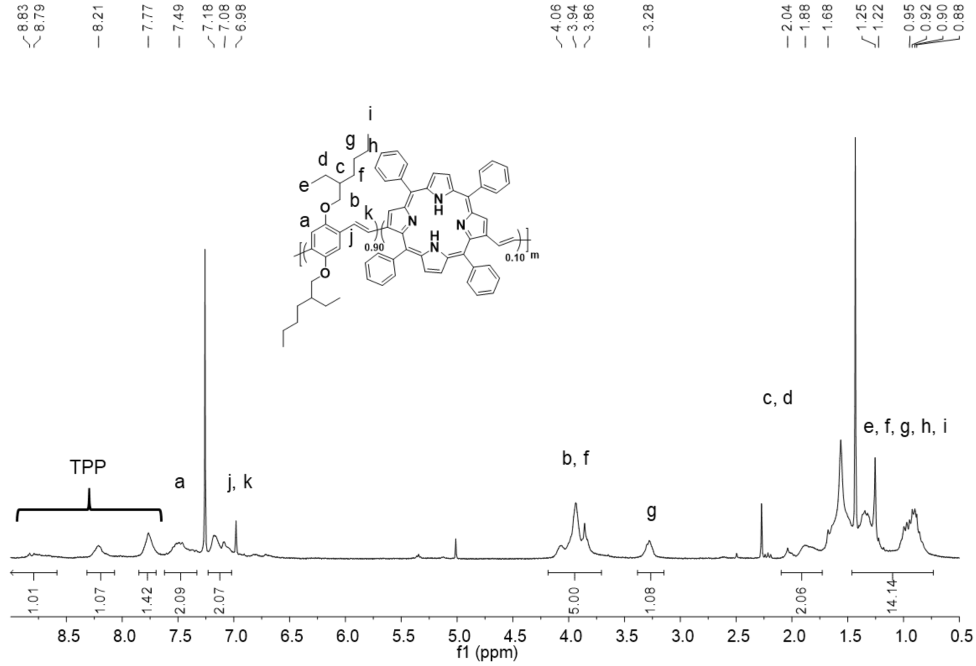

Figure 22. ^{1}H NMR spectra of PPV-TPP5% in CDCl$_3$.

Sample Name	M_n (g/mol)	M_w (g/mol)	PDI
PPV	8947	12613	1.4
PPV-TPP$_{2.5\%}$	11469	14478	1.26
PPV-TPP$_{5\%}$	12781	17016	1.33

Table 2. GPC data of PPV-TPPs.

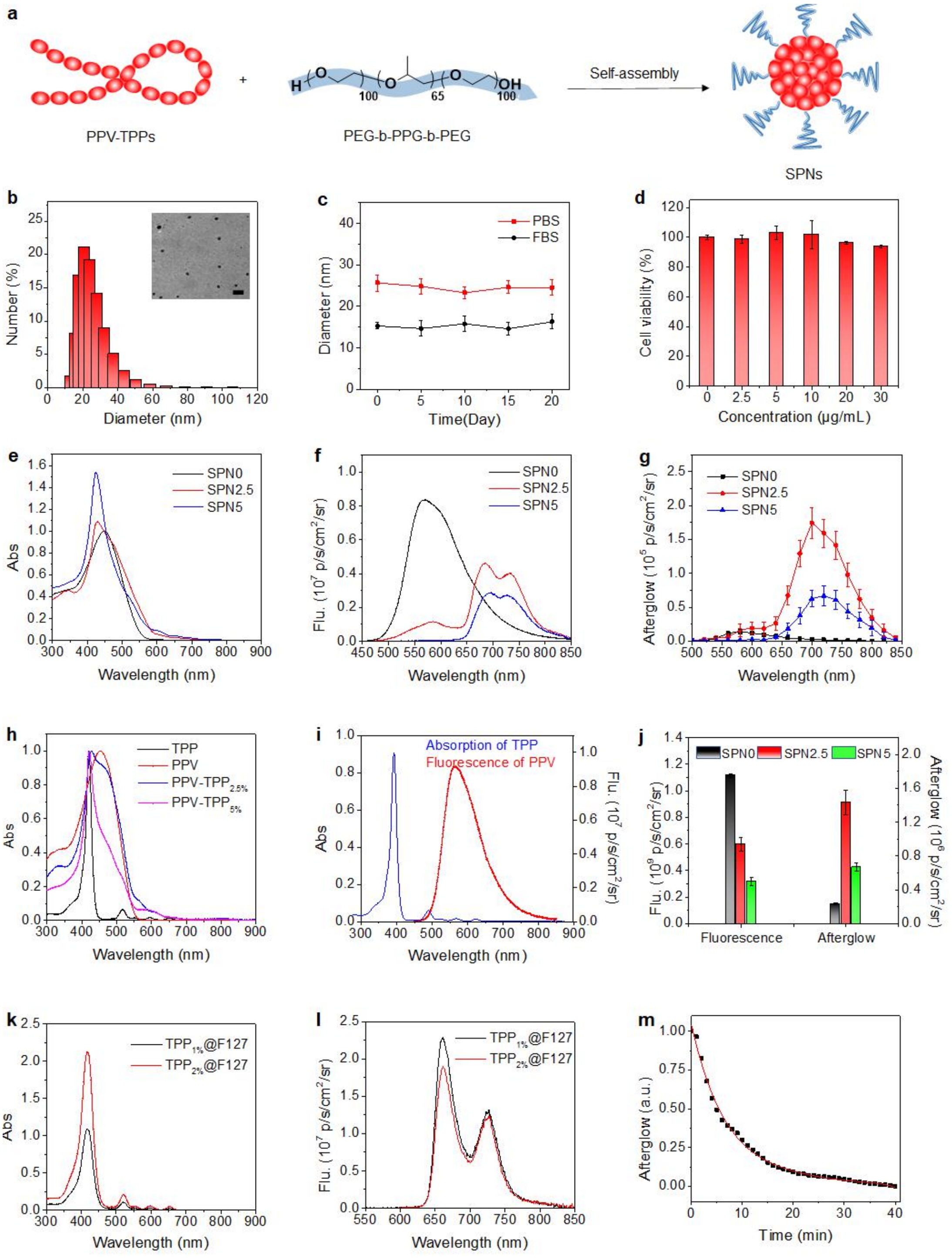

Figure 23. *In vitro* characterization of SPNs. a) Schematic illustration of the preparation of SPNs. b) DLS of SPN2.5 in 1×PBS buffer (pH = 7.4). The PDI of SPN2.5 is 0.356. Inset is TEM image of SPN2.5. The scale bar represents 100 nm. c) DLS data of SPN2.5 as a function of time incubated with PBS (pH = 7.4) and FBS. d) Cell viability of 4T1 cells after incubation with SPN2.5 solutions at various concentrations. e) UV-visible absorption spectra of SPNs. The

concentration of PPV component for all SPNs were 30 μg/mL in 1× PBS (pH = 7.4). f) Fluorescence spectra of SPNs. The concentration of PPV component of all SPNs were 100 μg/mL in 1× PBS (pH = 7.4). g) Afterglow luminescence spectra of SPNs (100 μg/mL). SPNs solutions were pre-irradiated for 1 min by white light before the collection of afterglow luminescence signal. h) Normalized UV-vis spectra of TPP, PPV, PPV-$TPP_{2.5\%}$ and PPV-$TPP_{5\%}$ in THF. i) UV-vis spectra of TPP and Fluorescence spectra of PPV in THF. j) Quantification of absolute fluorescence and afterglow intensities of SPNs. k) UV-vis spectra and l) Fluorescence spectra of $TPP_{1\%}$@F127 and $TPP_{2\%}$@F127 in PBS (pH = 7.4). The molar ratio of TPP to F127 is 1% for $TPP_{1\%}$@F127, which is equal to SPN2.5. The ratio of TPP to F127 is 2% for $TPP_{2\%}$@F127, which is equal to SPN5. m) Normalized decay of afterglow luminescence of SPNs (100 μg/mL) at room temperature. Before the collection of afterglow luminescence signal, SPNs solutions were pre-irradiated for 1 min with white light. The light power used in the experiments was 1 W/cm^2. Error bars represent the standard deviations of three separate measurements.

The PPV-TPPs were synthesized according to Scheme 6. Monomer 1,4-dibromo-2,5-bis((2-ethylhexyl)oxy)benzene was synthesized by 2,5-dibromohydroquinone and 3-(bromomethyl)heptane in the presence of K_2CO_3, 1,4-dibromo-2,5-bis((2-ethylhexyl)oxy)benzene was then copolymerized with trans-1,2-bis(tributylstannyl)ethene and 7,18-dibromo-5,10,15,20-tetraphenylporphyrin (TPP-Br) at different feeding ratio to yield PPV, PPV-$TPP_{2.5\%}$ and PPV-$TPP_{5\%}$ *via* Pd-catalyzed Stille coupling reaction (Scheme 6). As shown in the ^{1}H NMR of PPV-TPPs (Figure 19-22), the characteristic resonance peaks of TPP were found at 8.8, 8.2 and 7.8 ppm and the peaks of PPV backbone were found at 7.5, 7.2-7.1, 4.08-3.86, 3.40, 1.89, 1.30, 0.90-0.88 ppm, indicating the success of incorporation of TPP into PPV-TPPs. The molecular weight and PDI of PPV-TPPs were further characterized by GPC, and the molecular weights of PPV polymers ranged from 8900 to 13000 g mol^{-1} (Table 2). All the polymers had good solubility in THF, which facilitated the nanoprecipitation process used for the preparation of water-soluble nanoparticles.

Nanoprecipitation was applied to transform PPV, PPV-TPP2.5% and PPV-TPP5% into the hydrophilic nanoparticles termed as SPN0, SPN2.5 and SPN5, respectively in the presence of an amphiphilic triblock copolymer (PEG-*b*-PPG-*b*-PEG) (Figure 23a). DLS showed that the average hydrodynamic diameters of SPN, SPN2.5, SPN5 were similar, ranging from 25 to 30 nm. Taking SPN2.5 as the example, TEM showed its uniform spherical morphology with average diameter of about 25 nm, nearly identical to the DLS data (Figure 23b). No precipitation or obvious change in size was observed for SPN2.5 after storage in PBS (pH = 7.4) or FBS for 20 days (Figure 23c). In addition, SPN2.5 was non-cytotoxic to 4T1 cells as confirmed by MTS assay (Figure 23d). These results indicated that these SPNs should be suitable for biological applications.

The optical properties of SPNs were also tested in PBS solution (pH = 7.4). The UV-Vis spectra showed that all the SPNs had similar maximum absorption ranging from 430 to 450 nm (Figure 23e). Such an absorption band was assigned to the PPV segment as confirmed by the absorption spectra of the polymers in THF. With increasing the doping amount of TPP, a new absorption band of SPNs ranging from 600 to 700 nm appeared and gradually increased, verifying the incorporation of TPP into the backbone of PPV (Figure 23h). The fluorescence of TPP-free nanoparticle

(SPN0) had a visible emission with the maximum peak at 580 nm assigned to the PPV segment. With increased amount of TPP, the fluorescence at 580 nm decreased accompanied with increased NIR emission of TPP ranging from 650 to 750 nm (Figure 23f), and the saturation occurred at the doping amount of 2.5% (SPN2.5). Such a spectral change confirmed the occurrence of FRET from PPV segments to TPP, which was consistent with the good spectral overlap between the absorption of TPP and the emission of PPV from 500 to 700 nm (Figure 23i). However, as compared with SPN2.5, SPN5 showed decreased emission of TPP from 650 to 750 nm. To understand this phenomenon, the PPV-free nanoparticles were prepared *via* nanoprecipitation of TPP and PEG-b-PPG-b-PEG. Although the concentration of TPP was doubled (Figure 23k), the fluorescence decreased with increasing the doping concentration of TPP from 1 to 2% (Figure 23l). The quantification data showed that the absolute total fluorescence intensity of SPN0 was ~ 1.83 and ~ 3.67-fold higher than that of SPN2.5 and SPN5, respectively (Figure 23j). The decreased total fluorescence intensity should be attributed to the energy loss caused by FRET and the fluorescence self-quenching of TPP within SPN2.5 and SPN5.

The afterglow spectra and images of SPNs were collected after light irradiation under bioluminescence modes (without real-time excitation). The spectral profiles of afterglow were similarly to the fluorescence spectra (Figure 23g). However, with increasing doping of TPP, the absolute total afterglow intensity increased for both SPN2.5 and SPN5 relative to SPN0 (Figures 23g), which were different from the absolute total fluorescence intensity (decreased with increasing doping of TPP).

Moreover, the highest absolute afterglow intensity was observed for SPN2.5 rather than SPN5 (Figure 23j), which were ~ 6.12 and ~ 2.14-fold higher than that of SPN0 and SPN5, respectively. Such a difference in the absolute intensity between afterglow and fluorescence should be associated with their different luminescent mechanisms. The afterglow luminescence half-life of SPN2.5 was 5 min at room temperature (Figure 23m), long enough for imaging acquisition.

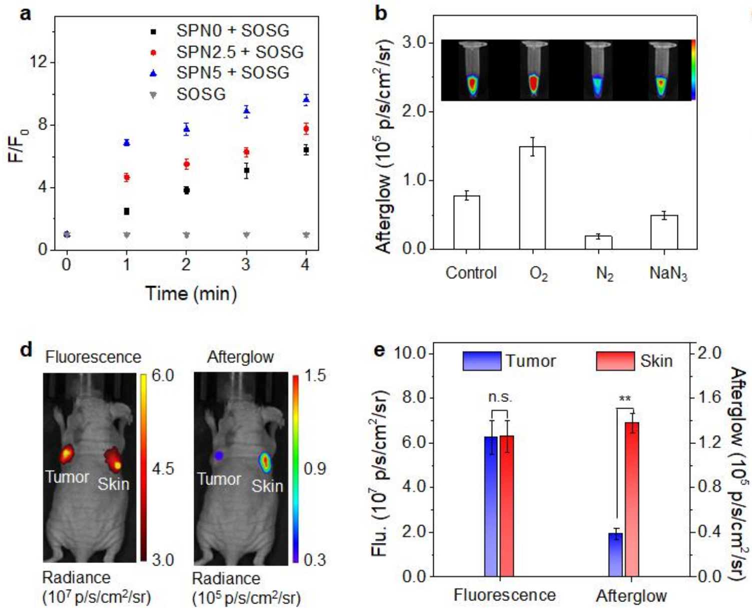

Figure 24. *In vivo* imaging of tumor hypoxia. a) Fluorescence enhancement (F/F_0) of SOSG (1 μM) in the absence or presence of SPN0, SPN2.5 and SPN5 (0.8 μg/mL) at 528 nm as a function of white light irradiation time. b) Afterglow luminescence intensities and images of SPN2.5 (50 μg/mL) acquired at room temperature, after purging by O_2, N_2 or in the presence of NaN_3 (50 w/w%). c) Schematic illustration of afterglow imaging of hypoxia and normoxia in a living mouse. SPN2.5 was purged with N_2 to remove oxygen before injection. d) Fluorescence and afterglow luminescence images of tumor and skin after local injection of SPN2.5 (100 μg/mL, 50 μL). e) Fluorescence and afterglow intensities of tumor and skin after local injection of SPN2.5 (100 μg/mL, 50 μL). Error bars represent standard deviations of three separate measurements (n = 3). n.s.: not significant, ** statistically significant difference ($p < 0.01$, n = 3).

As tested by $^1O_2$ sensor green (SOSG), the fluorescence intensities of SOSG at 528 nm in the presence of SPN0, SPN2.5 and SPN5 increased by 6.44-, 7.78- and 9.96-fold, respectively, after light irradiation for 4 min (Figure 24a). This proved that with increased doping amount of TPP, more $^1O_2$ was generated during light irradiation, and thus more PPV-dioxetane intermediates were produced, leading to the amplified afterglow for SPN2.5 and SPN5 relative to SPN0. However, due to the self-quenching of TPP, SPN5 had lower absolute afterglow intensity than SPN2.5. These data confirmed that incorporation of TPP into the backbone of PPV could amplify and red-shift its afterglow signal. With the brightest afterglow intensity among all the SPNs, SPN2.5 was chosen for *in vivo* imaging experiments. It was noted that the afterglow intensity of SPN2.5 could be increased by 1.90-fold when measured in O_2-saturated condition, while decreased by 4.06-fold when measured in N_2-saturated condition (Figure 24b); the addition of a $^1O_2$ scavenger (NaN_3) could reduce the afterglow intensity by 1.58-fold. Most tumor cells are in the hypoxic environment resulting from their rapid oxygen consuming for vasculature growth and cell proliferation. Because tumor hypoxia is associated with increased risk of invasion and metastasis, imaging of tumor hypoxia can be helpful for diagnosis and treatment of cancer. Because afterglow was sensitive to oxygen (Figure 24b), SPN2.5 was utilized to differentiate hypoxia and normoxia *in vivo*. The SPN2.5 solution was deoxygenated and then locally injected into tumor or under skin (Figure 24c). The fluorescence images of the mice were acquired at 720 nm upon excitation at 500 nm, while the afterglow luminescence images were obtained with a 30 s acquisition time with an open filter after pre-irradiated with white light for 1 min (Figure 24d). Signal quantification clearly showed that the afterglow intensity of locally injected skin was 3.56-fold higher than that of tumor while the fluorescence intensities between skin and tumor were almost the same (Figure 24e). The lower afterglow signal in tumor was attributed to the hypoxia environment of tumor, which had a low oxygen level that reduced the generation of $^1O_2$ and in turn the afterglow intensity of SPN2.5. These data indicated that afterglow luminescence of SPN2.5 could be potentially used to distinguish hypoxia from normoxia environment in living mice.

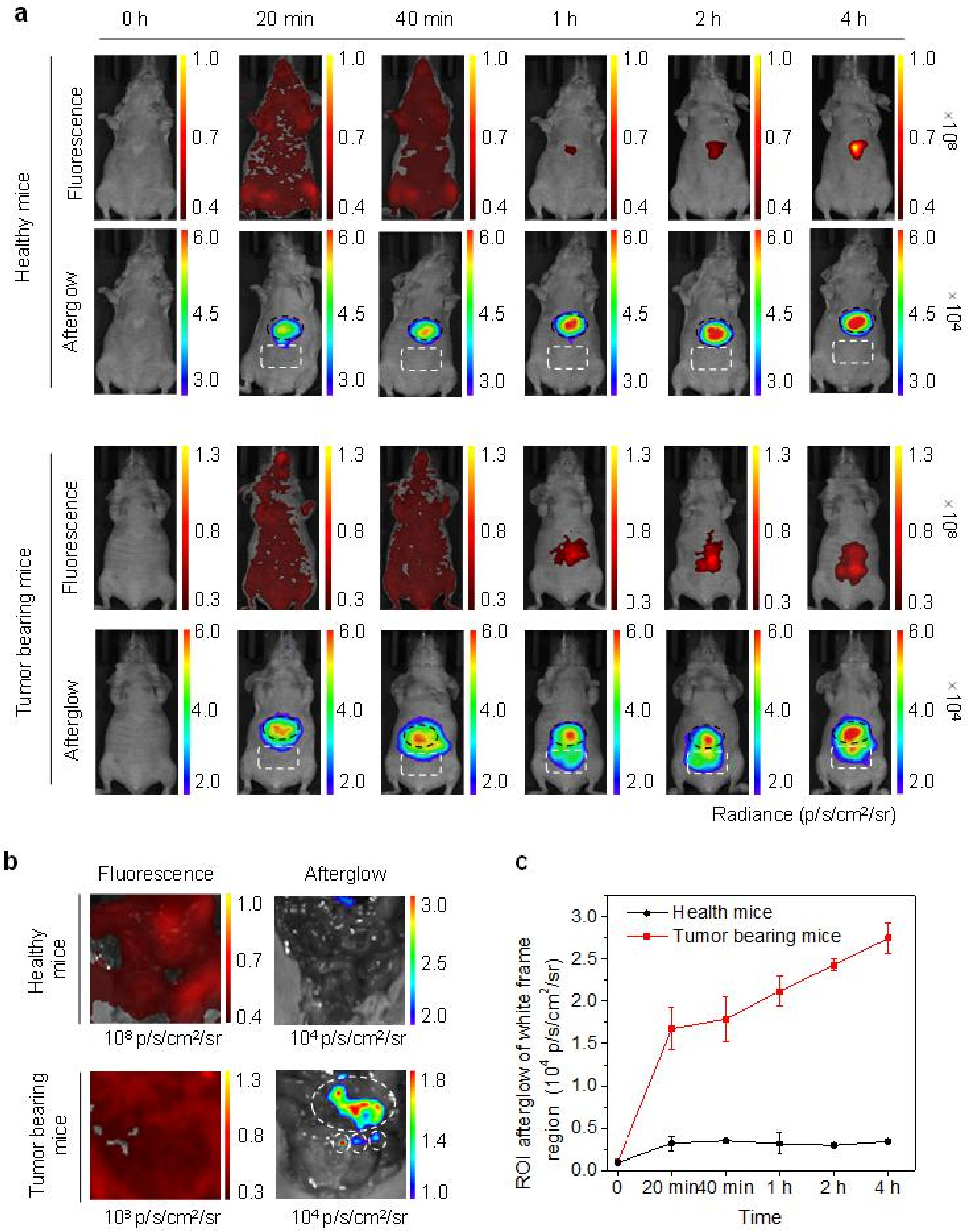

Figure 25. *In vivo* peritoneal metastatic tumor imaging. a) Fluorescence and afterglow luminescence images of healthy mice (up) and peritoneal metastatic tumor bearing mice (bottom) at different time points after intravenous injection of SPN2.5 (400 μg/mL, 200 μL). The liver site is marked by black circle. The lower quadrant region is marked by white frame. b) Fluorescence and afterglow luminescence images of mice with skin removed to expose the abdominal cavity at 4 h post-injection of SPN2.5. The lower quadrant region is marked by white circles. c) Afterglow luminescence intensities of the lower quadrant region (white frame) for SPN2.5-injected mice as

a function of post-injection time in Figure 25a. Error bars represent standard deviations of three separate measurements (n = 3).

To test the ability of SPN2.5 in imaging of metastatic tumor tissues, the peritoneal metastatic tumor mouse model was established by injecting 4T1 cell suspension (200 μL, 4×10^5) intraperitoneally into nude mice, and the healthy mice without injection of 4T1 cells was used as the control. The mice in both groups were injected with SPN2.5 through tail vein 4 d after the injection of cancer cells. Fluorescence and afterglow images were acquired at different time points post-injection of SPN2.5. Obvious afterglow signal from the liver (indicated by black circle) were observed for both groups at t = 20 min post-injection, while fluorescence signal of liver could only be detected after 1 h (Figure 25a). This reflected the higher tissue penetration of afterglow imaging relative to of fluorescence imaging. The afterglow intensity of lower quadrant region (indicted by white frame) gradually increased for 4T1 tumor-bearing mice (Figures 25a and 25c); in contrast, no obvious afterglow signal at the same region could be detected for the control group. At 4h post-injection, the afterglow signal in the lower quadrant region of 4T1 tumor-bearing mice was 27.6-times higher than background, while it was similarly to the background for the control mice. At this time point, skin and peritoneum of mice were removed and the lower quadrant region of mice were imaged by both afterglow and fluorescence. Due to the high sensitivity of afterglow, strong afterglow spots were detected on the intestines of T1 tumor-bearing mice, while only autofluorescence was detected in the abdominal cavity and no afterglow signal was observed for the control mice (Figure

25b).

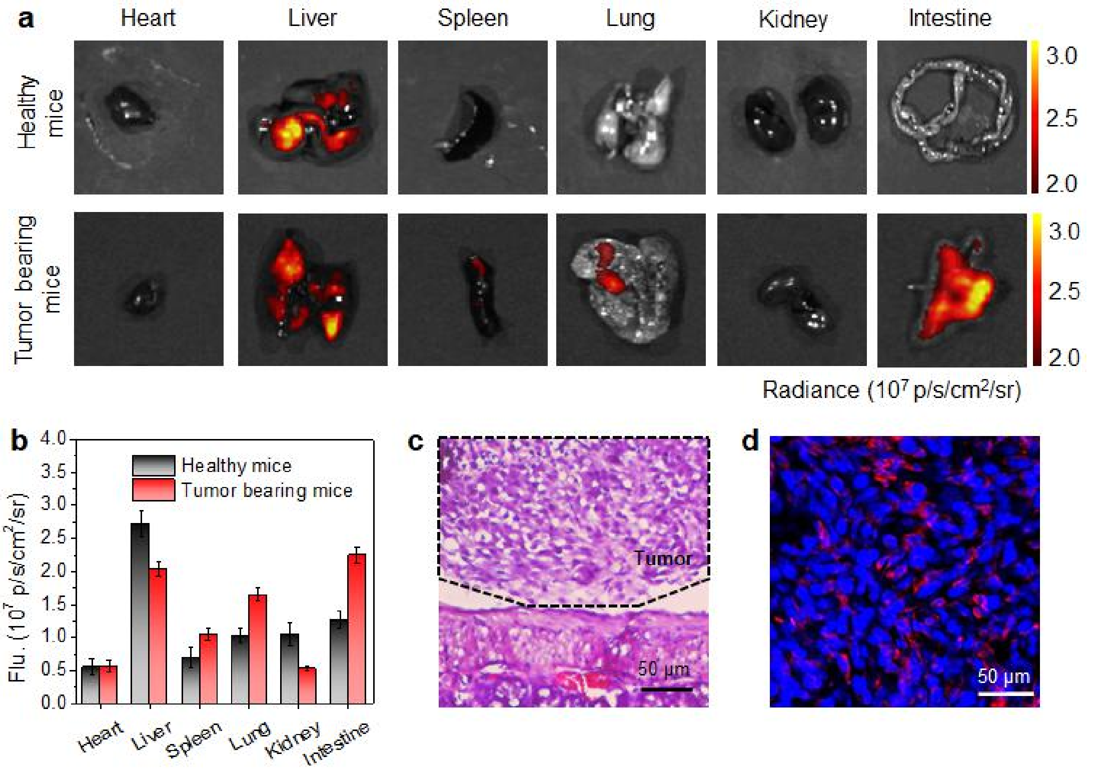

Figure 26. *Ex vivo* data of healthy mice and tumor bearing mice. a) *Ex vivo* biodistribution of healthy mice and tumor bearing mice in fluorescence signal. b) *Ex vivo* quantification of major organs from healthy mice and tumor bearing mice. c) H&E stained slices and d) confocal images of slices of peritoneal metastatic tumor obtained from SPN2.5-injected mice. The tumor regions are marked by black frames. For the fluorescence images, SPN2.5 was indicated as red color. The nuclei were stained by 4’,6-diamidino-2-phenylindole (DAPI) indicated as blue color.

To further verify SPN2.5 had the ability to selectively accumulate into the tumor site, *ex vivo* biodistribution were studied for both groups (Figure 26a). Obvious fluorescence signal could be observed both for the intestine and liver of 4T1 tumor-bearing mice (Figure 26b), while almost no fluorescence intensity could be detected for the intestine for the control mice. This further proved that the high fluorescence intensity from the intestine site of 4T1 tumor-bearing mice came from the metastatic tumor tissues. Histological examinations further confirmed the presence of tiny and naked eye barely detectable metastatic tumors on the surface of intestine (Figure 26c). Moreover, the fluorescence confocal imaging of tumor slices indicated that SPN2.5 had a good accumulation at the tumor site (Figure 26d). These data proved that the afterglow signals on the intestine site of 4T1 tumor-bearing mice came from the metastatic tumor tissues and indicated that SPN2.5 could be used as a potential afterglow imaging agent for *in vivo* detection of metastatic tumors.

5.4 Conclusion

In conclusion, we have synthesized a series of photosensitizer-incorporated PPVs and transformed them into afterglow nanoagents for *in vivo* imaging. With the help of FRET and promoted $^1O_2$ generation, SPN2.5 showed the NIR afterglow with the maximum at 720 nm, and amplified afterglow intensity that was 6.12-fold brighter than the non-doped nanoparticles (SPN0). The oxygen-sensitive afterglow of SPN2.5 made it useful for *in vivo* imaging of tumor hypoxia, showing 3.56-fold higher afterglow in skin than that in hypoxic tumor. In addition, the bright afterglow of SPN2.5 was used to detect tiny peritoneal metastatic tumor tissues in living mice through systemic administration. Due to the high sensitivity of afterglow imaging, metastatic tumor tissues could be delineated by afterglow spots on the intestines of SPN2.5 injected mice, which was not possible for fluorescence imaging. Thus, this study introduces a new generation of organic afterglow nanoagents with self-amplified signal for light-excitation-free *in vivo* imaging.

6. SPNs for PDT and PTT

6.1 SPN prodrug for Hypoxia-Activated Cancer Combined PDT-chemotherapy

6.1.1 Background

As we known, PDT have been used for cancer therapy; however, its efficacy is often compromised by tumor hypoxia. In fact, as a result of oxygen consumption and microvascular damage during PDT, PDT even increases the tumor hypoxia to a certain extent and further decreases its antitumor efficacy.[147] To overcome this issue, two strategies have been developed. One is to directly increase oxygenation in the tumor by corporation of oxygen-generating components such as perfluorocarbon and enzymes into photodynamic nanoparticles.[148] For example, hybrid MnO_2 nanoparticle coated with polyelectrolyte was developed for systemic intravaneous cancer treatment. The other is to combine PDT with chemotherapy, which uses the hypoxia-responsive carrier to encapsulate both photosensitizers and chemodrugs into the nanoparticles.[149] Although chemophototherapy is an emerging treatment for solid tumors,[150] most of these chemophototherapeutic agents are multicomponent systems, which suffer from the difficulty in quality control of nanoparticles preparation; moreover, they bear the risk of release/activation of the chemodrug in normal tissues. In addition, the overexpression or activation of intracellular reductases such as azoreductase and nitroreductase, can be promoted by tumor hypoxia, and various hypoxia-responsive moieties based on the reduction of azobenzene group, 2-nitroimidazole group, or nitrobenzene group have been designed and used for hypoxic tumor detection or treatment. Thus, hypoxia-microenvironment responsive prodrugs that can be specifically activated in solid tumors might be one of the effective strategies to overcome the hypoxia of tumors.

In this work, we synthesize a semiconducting polymer nano-prodrug (SPNpd) with a well-defined structure for hypoxia-activated synergistic cancer therapy. This nano-prodrug is assembled from an amphiphilic semiconducting brush polymer grafted with chemodrug side chains through hypoxia-cleavable linker. It has three key units (Figure 33a): the light-responsive photodynamic SPN core, hypoxia-cleavable linker and the chemotherapeutic drug, a bromoisophosphoramide mustard intermediate (IPM-Br). IPM-Br has been used for the treatment of a range of cancers, which is known to induce DNA crosslinking and cellular apoptosis.[151] Upon photoirradiation at 808 nm, SPNpd can generate $^1O_2$ for PDT; meanwhile, the tumor hypoxia in association with photoirradiation-depleted oxygen level specifically initiates the fragmentation and release of IPM-Br catalyzed by nitroreductase, leading to cell death. As such, SPNpd seamlessly integrates PDT with hypoxia-activated chemotherapy for synergistically amplified cancer therapy.

6.1.2 Experimental sections

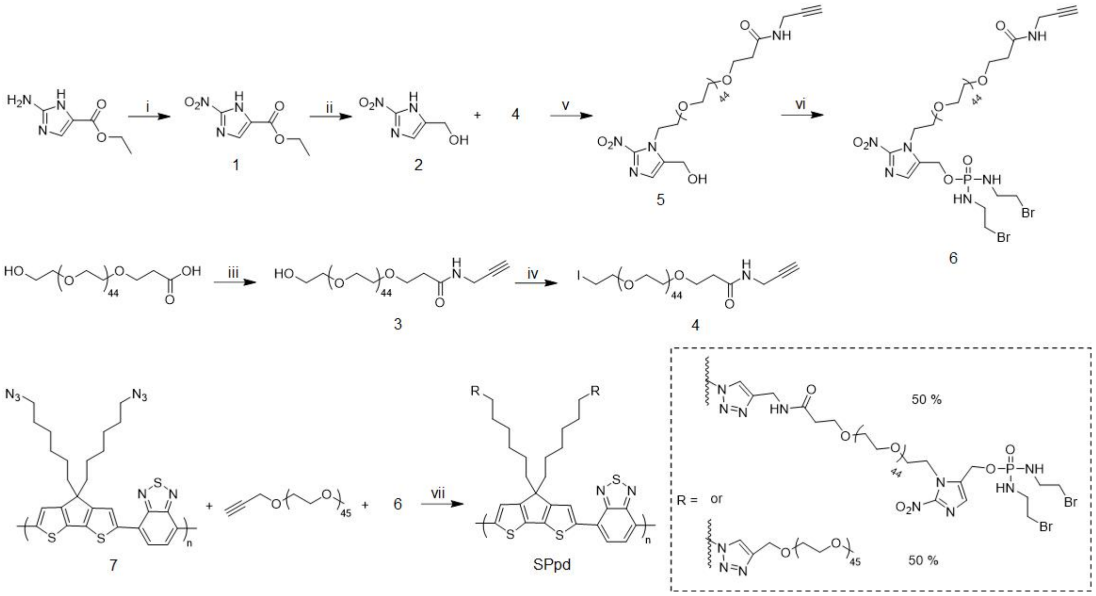

Scheme 7. Synthetic route and preparation of SPNpd and the drug-free control nanoparticle (SPNc). Reagents and conditions: i) AcOH, $NaNO_2$, rt, 4 h. ii) $NaBH_4$, I_2, tetrahydrofuran, 40 ºC, 24 h. iii) Propargylamine, 1-ethyl-3-(3-dimethylaminopropyl) carbodiimide hydrochloride, DCM rt, 24 h. iv) PBr_3, DCM, 0 ºC - rt, 12 h; NaI, acetone, 55 ºC, 48 h. v) $CsCO_3$, CH_3CN, 60 ºC, 48 h. vi) IPM-Br, triphenylphosphine (PPh_3), diisopropyl azodicarboxylate (DIAD), THF, 0 ºC - rt, 6 h. vii) CuBr, PMDETA, THF, 30 ºC, 24 h.

Synthesis of ethyl 2-nitro-1H-imidazole-5-carboxylate (1). Ethyl-2-amino-1H-imidazole-5-carboxylate (155 mg, 1 mmol) was added in AcOH (2 mL, 20 mmol), followed by addition of a saturated aqueous solution of $NaNO_2$ (1 mL, 10 mmol) dropwise. The reaction was conducted at room temperature for 4h. The solution was extracted with EA, and the organic layer was washed with water, $NaHSO_3$ aqueous solution and brine for three times. The organic solution was dried over anhydrous Na_2SO_4 and the crude product was purified *via* column chromatography over silica/hexane and EA (2/1, v/v). Compound 1 was obtained as brown solid (115 mg, 59.8 % yield). ^{1}H NMR (300 MHz, $CDCl_3$) δ 7.73 (s, 1H), 4.35 (q, J = 7.1 Hz, 2H), 1.34 (t, J = 7.1 Hz, 3H).

Synthesis of (2-nitro-1H-imidazol-5-yl) methanol (2). Compound 1 (115 mg, 0.59 mmol), $NaBH_4$ (66.3 mg, 1.8 mmol) and I_2 (246 mg, 1.8 mmol) were dissolved in anhydrous THF. The mixture was stirred at room temperature at 40 ºC for 24 h. The solvent was removed under vacuum. The solution was extracted with EA, and washed by water. The organic phase was dried over Na_2SO_4. The crude product was purified via column chromatography over silica/hexane and EA (1/2, v/v). Compound 2 was obtained as yellow solid (50 mg, 56.8 % yield). ^{1}H NMR (300 MHz, MeOD) δ 7.07 (s, 1H), 5.40 (s, 1H), 4.19 (q, J = 7.1 Hz, 2H).

Synthesis of hydroxyl-Polyethylene glycol (PEG)-alkyne (2K) (3). Hydroxyl-PEG-Carboxylic acid (COOH) (2K) (300 mg, 0.3 mmol) and EDC were added into DCM at 0 ºC. Propargylamine was added into the above solution after 1 h. The reaction was conducted at room temperature for 24 h. The solvent was removed under vacuum. The product was purified via dialysis against DI water. Compound 3 (280 mg, 91.3 % yield) was obtained after lyophilization.

Synthesis of Iodide-PEG-alkyne (2K) (4). Compound 3 (200 mg, 0.2 mmol) and PBr_3 (20 µL, 0.2 mmol) were dissolved in anhydrous DCM at 0 ºC. The mixture was stirred at room temperature for 12 h. The resulting solution was purified by dialysis and lyophilization. The intermediate product and NaI (85 mg, 0.6 mmol) were dissolved in acetone. The reaction was carried out at 55 ºC for 48 h. The solvent was removed under vacuum. The crude product was purified via dialysis. Compound 4 (103 mg, 48.5 % yield) was obtained after lyophilization. ^{1}H NMR (300 MHz, $CDCl_3$) δ 4.20 – 4.11 (m, 2H), 4.06 (dd, *J* = 5.6, 2.4 Hz, 2H), 3.99 – 3.93 (m, 3H), 3.92 – 3.24 (m, 180H), 2.25 (d, *J* = 19.6 Hz, 2H).

Synthesis of 1-(PEG-alkyne)-2-nitro-1H-imidazol-5-yl) methanol (5). Compound 2 (19 mg, 0.13 mmol), compound 4 (90 mg, 0.09 mmol) and $CsCO_3$ (59 mg, 0.18 mmol) were dissolved in anhydrous CH_3CN. The mixture was stirred at 60 ºC for 24 h. The solvent was removed under vacuum. The product was purified by dialysis. Compound 5 (85 mg, 70.8 % yield) was obtained as yellow solid. ^{1}H NMR (300 MHz, $CDCl_3$) δ 7.46 (s, 1H), 4.34 – 4.25 (m, 2H), 4.16 (d, J = 9.9 Hz, 1H), 4.09 (dd, J = 5.6, 2.5 Hz, 1H), 4.02 (s, 2H), 3.92 – 3.24 (m, 180H), 2.30 – 2.21 (t, 2H).

Synthesis of Compound 6. IPM-Br (37 mg, 0.12 mmol), compound 5 (70 mg, 0.06 mmol), PPh_3 (32 mg, 0.12 mmol), DIAD (23 μL, 0.12 mmol) were added to anhydrous THF at 0 ºC. The reaction was carried out at room temperature for 6 h. The solvent was removed under vacuum. The crude product was purified *via* column chromatography over silica/DCM and methanol (10/1, v/v). Compound 6 as yellow solid (43 mg, 39.1 % yield) was obtained. ^{1}H NMR (300 MHz, $CDCl_3$) δ 7.49 (s, 1H), 5.20 (d, *J* = 7.8 Hz, 2H), 4.37 – 4.25 (m, 2H), 4.17 (d, J = 10.6 Hz, 2H), 4.10 (dd, *J* = 5.6, 2.5 Hz, 2H), 4.03 (s, 2H), 3.93 – 3.37 (m, 180H), 2.95 (m, 9H), 2.26 (t, *J* = 2.5 Hz, 2H).

Synthesis of Polymer 9. Compound 6 (28 mg), polymer 7 (was synthesized according to the previous literature[1]) (20.8 mg) and methoxy-PEG-alkyne (8) (was synthesized by propargyl bromide, sodium hydride and methoxy-PEG-hydroxyl) (20 mg) were dissolved in anhydrous THF, followed by addition of CuBr (20 mg) and PMDETA (60 μL). The mixture was stirred at 30 ºC for 24 h. The solvent was removed and crude product was purified *via* dialysis against DI water. Polymer 9 (39 mg, yield 56.5 %) was obtained as blue solid after lyophilization. ^{1}H NMR (300 MHz, $CDCl_3$) δ 8.11 (d, J = 5.3 Hz, 1H), 7.97 – 7.42 (m, 3H), 6.97 (d, J = 21.3 Hz, 1H), 4.71 (s, 1H), 4.53 – 3.94 (m, 6H), 3.95 – 3.45 (m, 180H), 3.21 (s, 4H), 2.95 (s, 2H), 2.80 – 1.77 (m, 26H), 1.74 – 0.98 (m, 60H), 0.96 – 0.67 (m, 18H).

Characterization. DLS and zeta potential were obtained on the Malvern Nano-ZS Particle Size. TEM images were obtained on a JEM 1400 transmission electron microscope with an accelerating voltage from 40 to 120 kV. UV-Vis spectra were obtained on a Shimadzu UV-2450 spectrophotometer. Fluorescence experiments were carried out on a TCSPC spectrofluorometer. GPC was recorded by a Shimadzu LC-VP system with polystyrenes as the standard and HPLC grade THF as the eluent. NMR spectroscopy was recorded on a BRUKER Advance 300 NMR (1H, 300 MHz) system with $CDCl_3$ or methanol-D_4 as the solvent. The spectrum was internally referenced to the tetramethylsilane signal at 0 ppm. HPLC analyses were performed on an Agilent 1260 system equipped with a G1311B pump, a UV detector and an Agilent Zorbax SB-C18 RP (9.4 × 250 mm) column, with methanol (0.1% of trifluoroacetic acid) and H_2O (0.1% of TFA) as the eluent. ALSM800 confocal laser scanning microscope (Carl Zeiss, Germany) was used to capture the fluorescence images.

In Vitro $^1O_2$ Generation Study of SPNs. This data was performed by using SOSG. ICG was used as the reference. SOSG solution (5 μL, 100 μM) was added to SPNs and ICG solution (30 μg mL^{-1}, 1 mL) with a NIR laser irradiation (808 nm, 0.3 W/cm^2) for 4 min. The fluorescence of SOSG incubated with SPNs and ICG was recorded at 520 nm on a Fluorolog spectrofluorometer at various irradiation times. The quantification of $^1O_2$ generation efficiency (ΦΔ) of SPNs are estimated by comparing the photosensitizing reaction rate of SPNs with that of ICG by the following equation: $\Phi\Delta_{SPN} = (r_{SPN}/A_{SPN})/(r_{ICG}/A_{ICG}) \times \Phi\Delta_{ICG}$, where r_{SPN} and r_{ICG} are the SOSG reaction rate with $^1O_2$ generated from SPNs and ICG, which can be directly obtained from time-dependent fluorescence enhancement of SOSG, respectively; A_{SPN} and A_{ICG} are the corresponding absorbances of SPNs and ICG at 808 nm, respectively; $\Phi\Delta_{ICG}$ is the known $^1O_2$ generation efficiency of ICG, which is 0.2%.

In Vitro Prodrug Activation Assay. SPNpd (100 μM) and Nicotinamide adenine dinucleotide (NADH) (200 μM) were dissolved in tris buffer (pH = 7.4). Then, the mixture was degassed with vacuum-argon cycles to remove air. Nitroreductase (1μg·mL^{-1}) was added into this solution and the mixture was incubation at 37 ºC for 6 h. The resulting solution was purified by filtration through a 0.22 μm polyvinylidene fluoride syringe driven filter. The solution was analyzed by HPLC. The conditions were shown as below: methanol/ H_2O (v/v) = 0: 100 (0 min) to 20: 80 (40 min); flow rate = 1 mg mL^{-1}; detection under UV light at 214 nm.

In Vitro Cytotoxicity Assay. The 4T1 cells were cultured in DMEM containing 10 % FBS in a humidified environment containing 95% air and 5% CO_2 at 37 °C. 4T1 cells were seeded in 96-well plates at an intensity of 6×10^4 cells mL^{-1}. After 12 h incubation, the medium was replaced by fresh medium containing SPNpd or SPNc suspensions at different concentrations (5, 10, 20, 50, 100 μg mL^{-1}) and the cells were then incubated for 12 h. To simulate the hypoxic environment, the plates of hypoxic treatment groups were firstly incubated for 6 h in a nitrogen environment. To study the photodynamic effect on cell viability, the plates were irradiated by using an 808 nm laser (0.3 W cm^{-2}, 8 mins $well^{-1}$). All the treatment groups' cells were incubation for totally 12 h (include hypoxic treatment time and laser irradiation time). Then, MTS reagent was added into cell culture medium (1/5, v/v) for cell incubation. After 4 h incubation, UV measurement (490 nm) of cell culture medium was taken to calculate the cell viability.

Confocal Fluorescence Imaging for Cell Uptake. 4T1 cells (10^5 mL^{-1}) were plated on 14 mm glass coverslips and incubated for 12 h. SPNpd or SPNc (30 μg mL^{-1}) were added to the dishes and incubated with cells in DMEM for 12 h. The cells were washed with PBS, fixed with 4% paraformaldehyde and then stained with DAPI. The confocal system was used to capture the fluorescence images.

Tumor Mouse Model. All animal experiments were performed in compliance with the Guidelines established by the Institutional Animal Care and Use Committee (IACUC), SingHealth. To establish tumor models in six-week-old female NCr nude mice, two million 4T1 cells in supplemented DMEM (10% FBS, 1% pen/strep: 100

U mL^{-1} penicillin and 100 μg mL^{-1} streptomycin) were injected subcutaneously to NCr nude mice at the left flank.

Tumor Imaging. 4T1 cells (2 million cells per mouse) were injected subcutaneously to NCr nude mice at the left flank. When the tumor volume reached about 50-60 mm^3, SPNpd or SPNc (400 μg mL^{-1} based on the concentration of PCPDTBT, 200 μL) was systematically injected through the tail vein. NIR Fluorescence images were acquired at t = 1, 2, 4, 6, 8, 24 and 32 h post-injection. Fluorescence images were captured with a 0.1 s acquisition time with excitation at 675 ± 10 nm, and emission at 845 ± 10 nm using the IVIS Spectrum imaging system. Fluorescence images were analyzed by ROI analysis using the Living Image 4.0 Software.

*In Vivo Synergistic Antitumor Therapy***.** 4T1 cells (2 million cells per mouse) were injected subcutaneously to NCr nude mice at the left flank. When the tumor volume reached about 50-60 mm^3, the mice were randomly allocated to different groups and were treated with SPNpd or SPNc (400 μg mL^{-1} based on the concentration of PCPDTBT, 200 μL) or saline through tail vein. This date was designated as Day 1. Each group contains 4 mice. The treated mice were exposed to 808 nm laser of 0.3 W cm^{-2} for 6 min after systemic administration of SPNpd, SPNc or saline at the post-injection time of 24 h. IR thermal camera was used to monitor and record the temperature change of the tumor during irradiation. The tumor volumes were measured in two dimensions every other day using a slide caliper and calculated as $V = a \times b^2 / 2$ (a and b: the longest and shortest diameter of tumor respectively).

Histological Analysis. The mice were sacrificed after 15 days of treatment, the mice in each group were euthanized to extract tumors, hearts, livers, spleens, lungs and kidneys. The collected tumor or other tissues were fixed in 4% paraformaldehyde at 4 °C for 48 h and dehydrated with sucrose solution (30%) for 24 h. The dehydrated tumor tissues were embedded in frozen optimal cutting temperature medium and cut into 10 μm sections using a cryostat. For immunofluorescence staining, the tumors were fixed in 4% paraformaldehyde for 4 h at 4 °C, incubated in 30% sucrose solution for 12 h and frozen in Optimal Cutting Temperature (O.C.T.) embedding medium. 8 μm sections were cut for histological analysis. The sections were rehydrated in PBS containing 0.1% Triton X-100 for 10 min and followed by incubation with 3% BSA for 1 h at 37°C, then stained with cleaved caspase-3 antibody for 1 h in a humidified chamber at 37°C. The slides were washed three times with PBS for 5 min each and then counterstained with Alex-488 conjugated donkey anti-rabbit secondary antibody for 30 min at 37°C. Next, the nucleus was stained with DAPI. The slides were mounted by one drop of Fluoromount Aqueous Mounting Medium and imaged with CLSM.

6.1.3 Results and Discussions

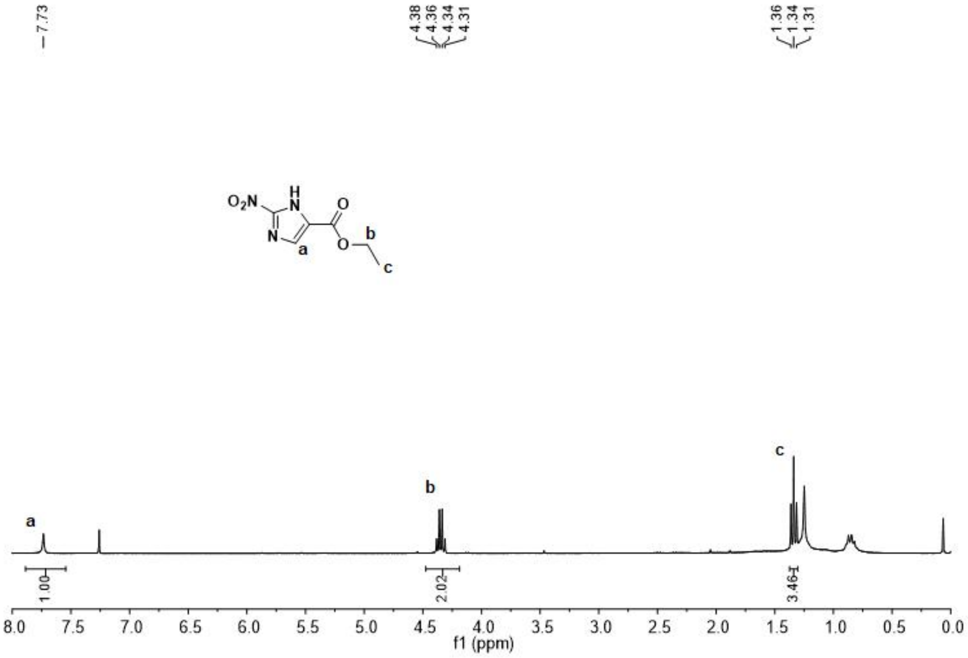

Figure 27. ^{1}H NMR spectra of ethyl 2-nitro-1H-imidazole-5-carboxylate (1) in $CDCl_3$.

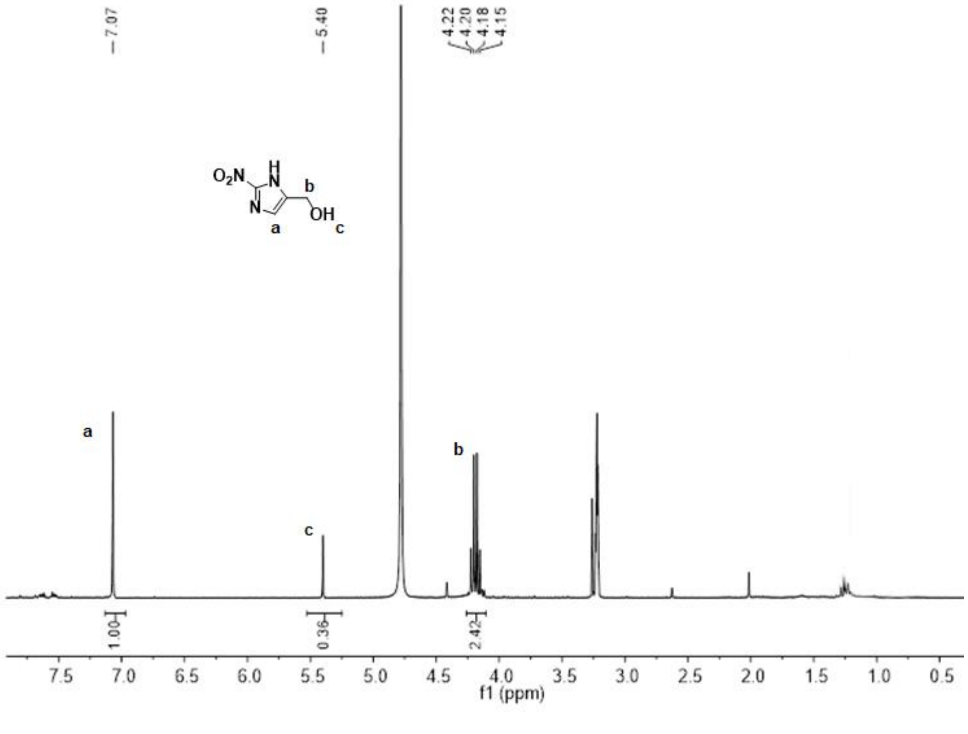

Figure 28. ^{1}H NMR spectra of (2-nitro-1H-imidazol-5-yl) methanol (2) in methanol-D_4.

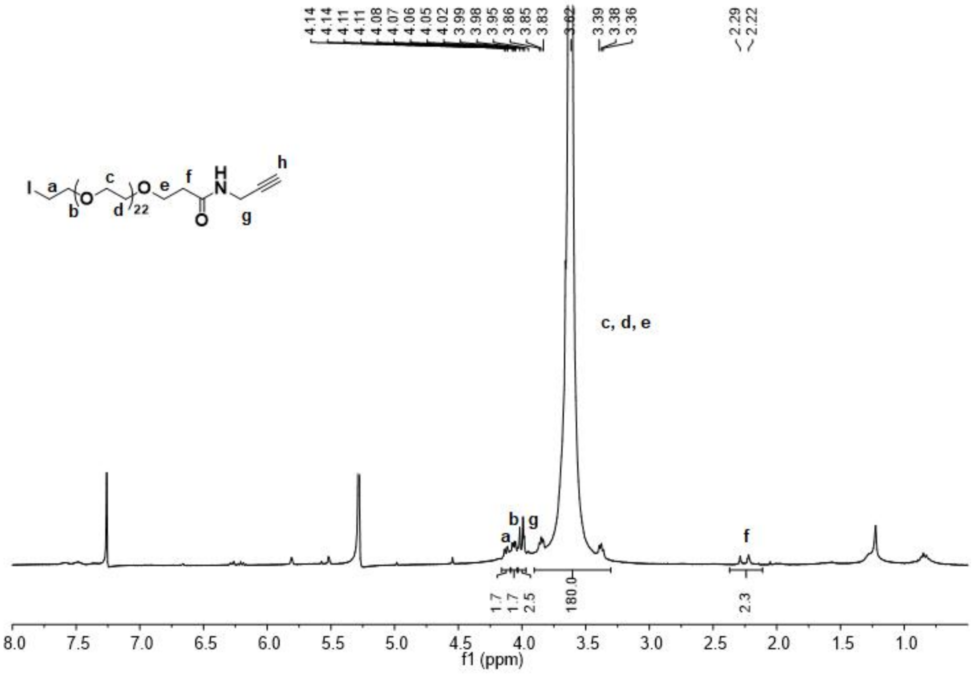

Figure 29. ^{1}H NMR spectra of Iodide-PEG-alkyne (4) in CDCl$_3$.

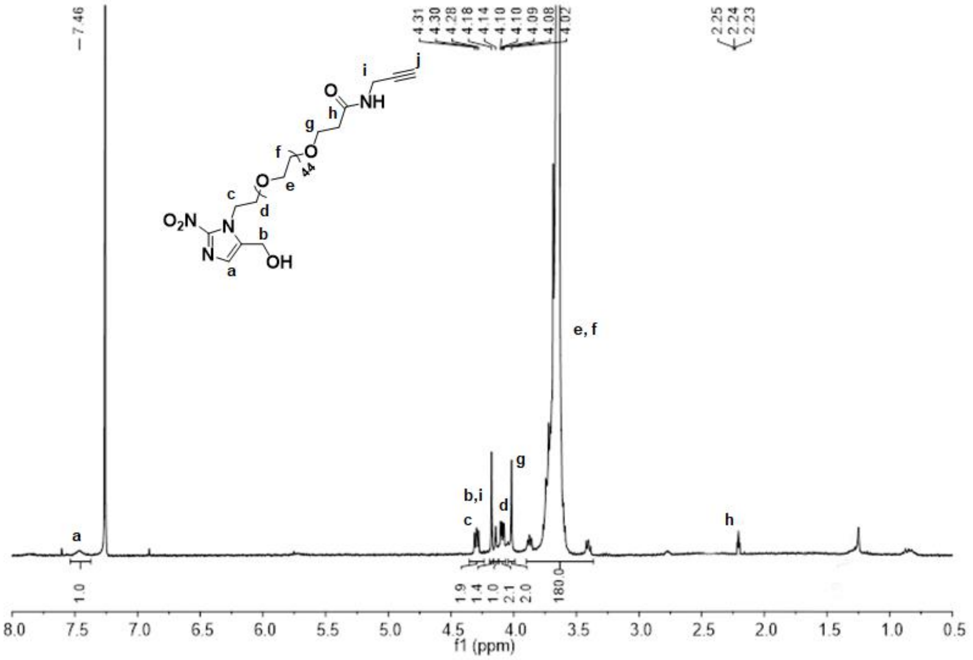

Figure 30. ^{1}H NMR spectra of 1-(PEG-alkyne)-2-nitro-1H-imidazol-5-yl) methanol (5) in CDCl$_3$.

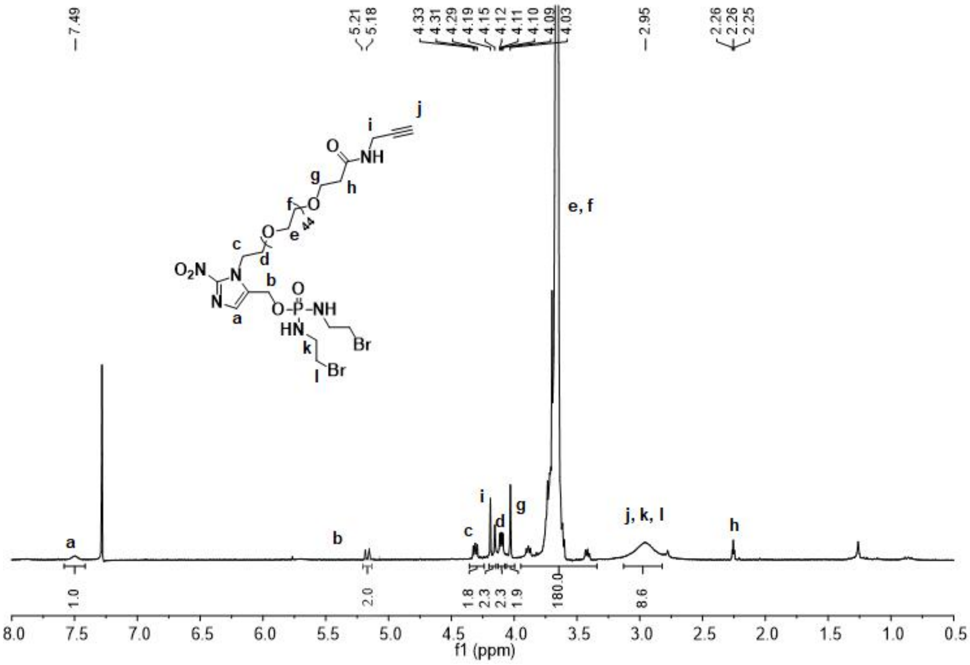

Figure 31. ^{1}H NMR spectra of compound 6 in $CDCl_3$.

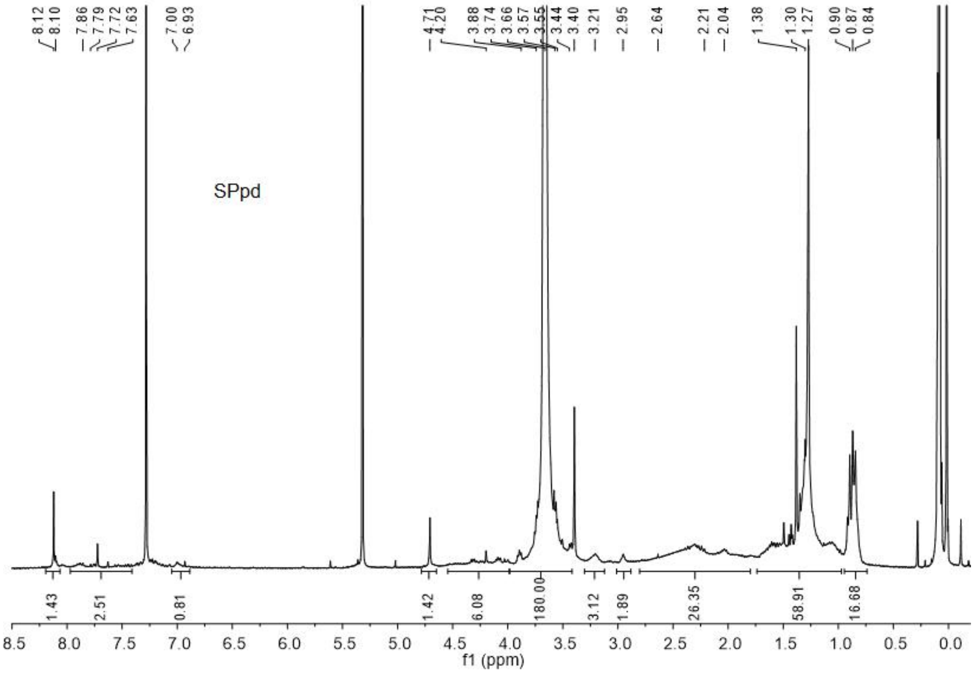

Figure 32. ^{1}H NMR spectra of compound 9 in $CDCl_3$.

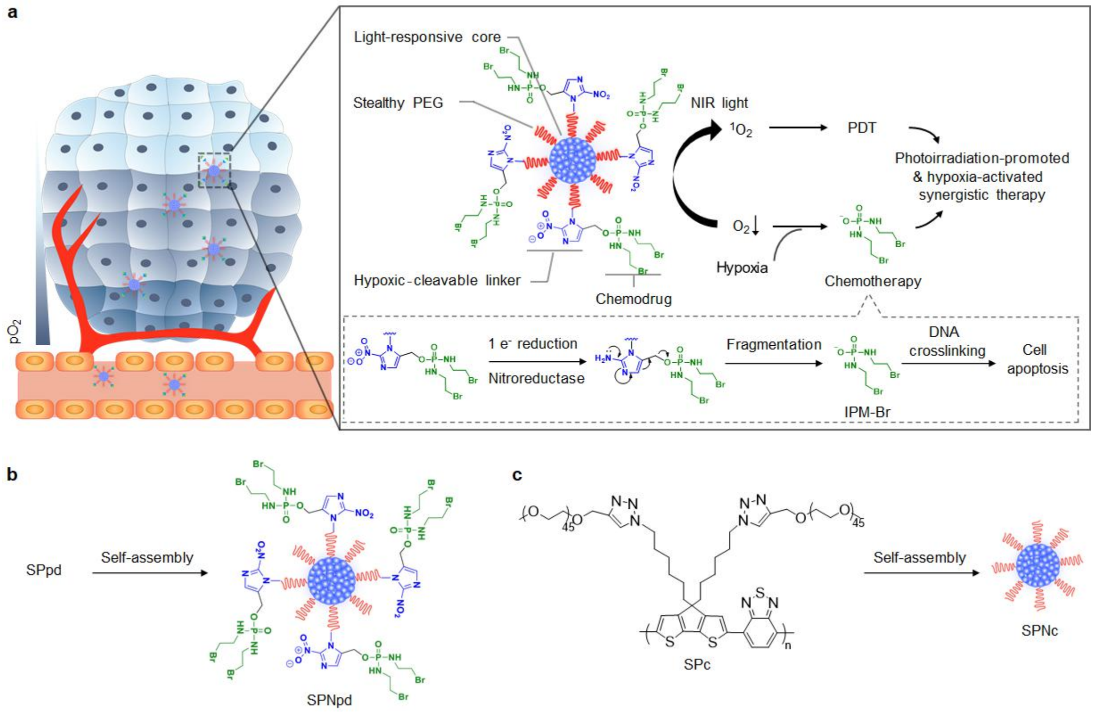

Figure 33. Molecular mechanism of SPNpd for synergistic cancer therapy. a) Schematic illustration of SPNpd for hypoxia-activated synergistic PDT and chemotherapy. b) and c) Scheme of formation of SPNpd and SPNc.

The drug-conjugated polymer (SPpd) and the drug-free control polymer (SPc) were synthesized via a graft-on approach (Scheme 7). To construct the drug-conjugated PEG (6), (2-nitro-1H-imidazol-5-yl) methanol (compound 2) was firstly synthesized *via* nitrification of ethyl 2-amino-1H-imidazole-5-carboxylate followed by ester reduction reaction. The iodide-PEG-alkyne (4) was synthesized via amidation of HO-PEG-carboxymethyl followed by halogen substitution reaction. The drug-conjugated PEG (6) was synthesized via substitution between 2 and 4, followed by phosphorylation. The ^{1}H NMR spectrum (Figure 31) showed that the characteristic proton resonance peak of -NH-C$\underline{H_2}$-CH$_2$-Br and -NH-CH$_2$-C$\underline{H_2}$-Br in IPM-Br were found at 2.95 ppm and -O-C$\underline{H_2}$-CH2-, -O-CH$_2$-C$\underline{H_2}$- in PEG were found at 3.93-3.37 ppm, implying the correct structure of 6. The final product SPpd was synthesized via copper(I)-catalyzed alkyne-azide cycloaddition (CAAC) reaction of the azide-modified polymer (polymer 7), compound 6, and mPEG-alkyne (the molar ratio of 6 to mPEG-alkyne was 1). As shown in the ^{1}H NMR spectra of SPpd (Figure 32), the characteristic proton resonance peaks of 7 were found at 8.12-7.63, 1.38 and 0.88 ppm. SPc was also synthesized via CAAC reaction of 7 and mPEG-alkyne. The gel permeation chromatography (GPC) data showed that the number-average molecular weights of SPpd and SPc were ~ 20000 g mol^{-1}with good PDI.

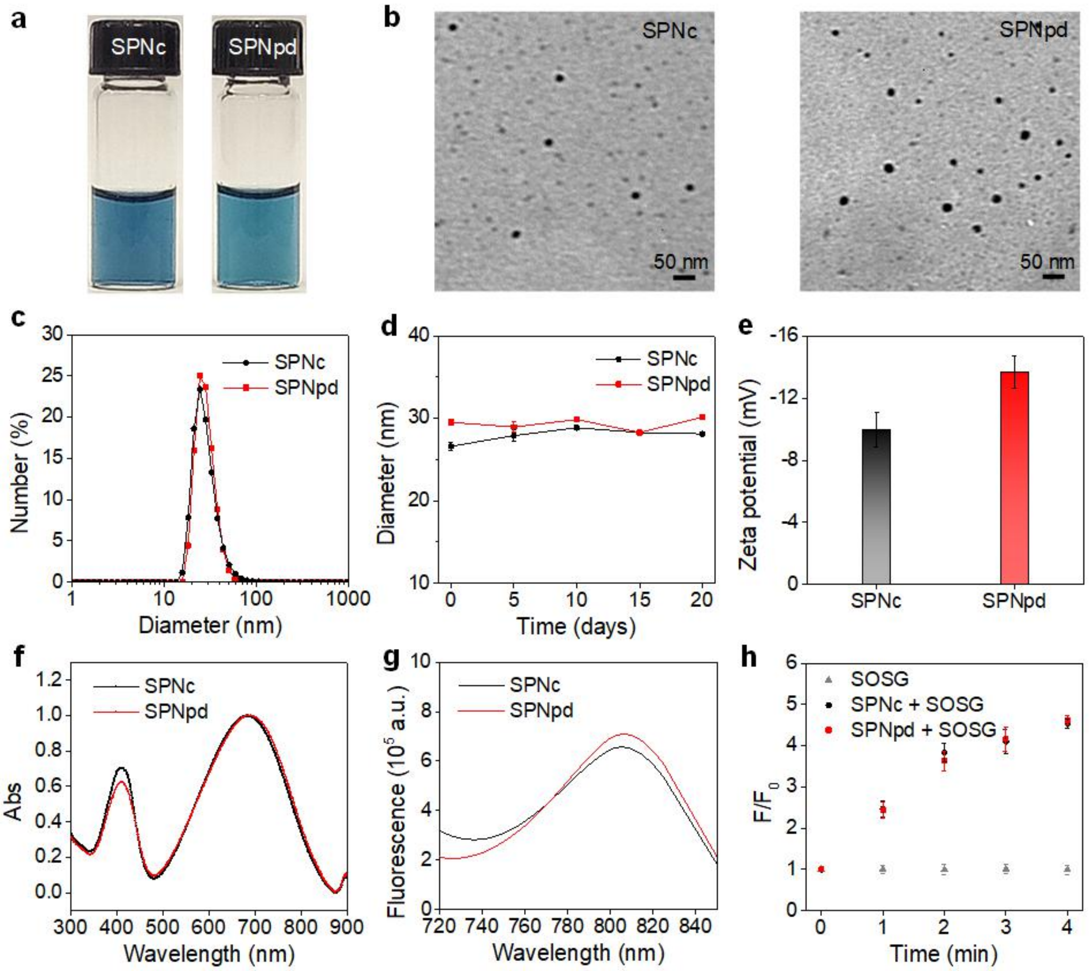

Figure 34. *In vitro* characterization. a) Pictures of nanoparticle solutions (30 μg mL^{-1}). b) TEM

images of SPNpd and SPNc (Scale bar = 50 nm). c) DLS data of SPNpd and SPNc. d) DLS data of SPNpd and SPNc as a function of incubation time in PBS (pH = 7.4). e) Zeta-Potentials of SPNpd and SPNc. f) UV−vis absorption and g) fluorescence spectra of SPNpd and SPNc. h) Generation of $^1O_2$ determined by increased fluorescence intensity of SOSG in the absence or presence of SPNpd and SPNc (30 μg mL^{-1}) as a function of photoirradiation time (808 nm, 0.3 W cm^{-2}). Error bars represent the standard deviations of three separate measurements (n = 3).

Both SPpd and SPc assembled into the nanoparticles due to their amphiphilic nature in aqueous solution (termed as SPNpd and SPNc, respectively) (Figure 33b and 33c), forming the translucent solutions (Figure 34a). The TEM data showed both SPNpd and SPNc have uniform spherical morphology with an average diameter of ~ 30 nm (Figure 34b), nearly identical to DLS data (Figure 34c). After storage in PBS for 20 days, no precipitation or obvious change in size was observed for both nanoparticles (Figure 34d). In PBS (pH = 7.4), SPNpd and SPNc had the zeta potentials of -10.3 and -13.7 mV, respectively (Figure 34e). Both SPNs had similar absorption ranging from 450 to 900 nm with the maximum at 690 nm ((Figure 34f), and their fluorescence maximum was at 820 nm (Figure 34g). SOSG was used to investigate the photodynamic property. Under photoirradiation at 808 nm for 4 mins, the fluorescence of SOSG at 528 nm increased by ~4.60-fold for SPNpd and SPNc (Figure 34f), proving that they had the identical photodynamic property under normoxic environment. The $^1O_2$ generation efficiencies ($\Phi\Delta$) of SPNpd (3.75%) and SPNc (3.73%) were ~18 times higher than ICG ($\Phi\Delta$ = 0.2%). These data indicated that the conjugation of the hypoxic activated-prodrug had minimal influence on the optical and photodynamic properties of SPNpd.

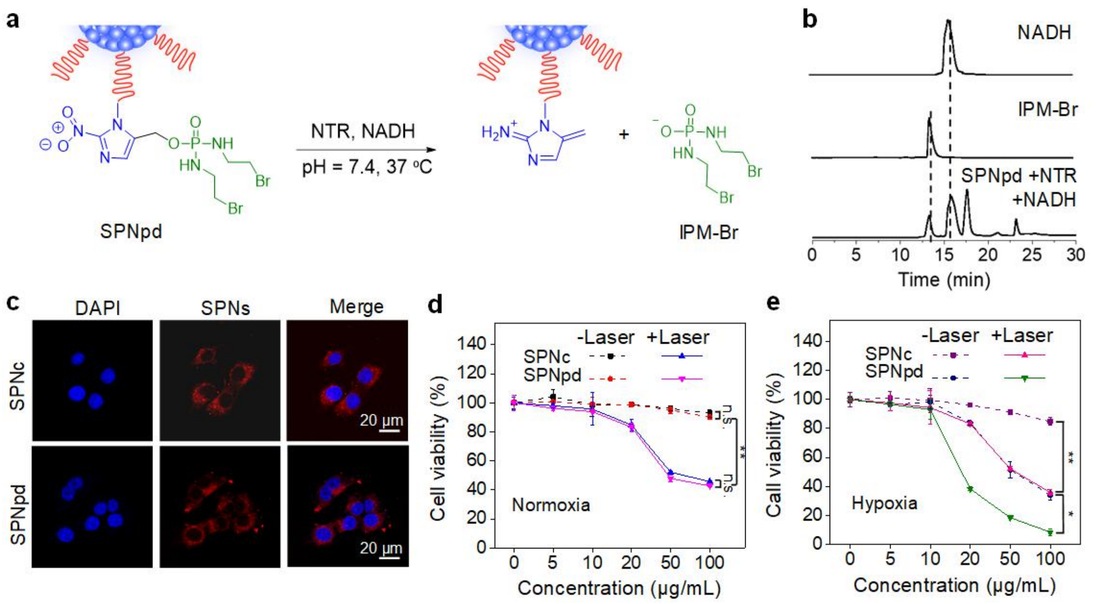

Figure 35. *In vitro* study of prodrug activation, cellular uptake and cytotoxicity. a) Scheme of prodrug activation and drug releasing study. b) HPLC profiles of NADH (200 µM), IPM-Br (10 µg mL^{-1}) and the resulting solution of SPNpd after incubation with nicotinamide adenine dinucleotide (NADH) under anaerobic condition for 6 h. c) Confocal fluorescence images of 4T1 cells incubation with SPNpd and SPNc (30 µg mL^{-1}) for 12 h. The blue fluorescence stands for the cell nuclei which were stained with 4,6-diamidino-2-phenylindole (DAPI). Cell viability of 4T1 cells after incubation with SPNc or SPNpd at various concentrations under d) normoxic. or e) hypoxic environment, with or without photoirradiation (808 nm, 0.3 W cm^{-2}). Error bars represent the standard deviations of three separate measurements (n = 3). n.s. means no significance, *p < 0.05, **p < 0.01 and ***p < 0.001.

To prove the hypoxia-induced prodrug activation of SPNpd, high-performance liquid chromatography (HPLC) analysis was used. SPNpd was first mixed with nitroreducase (NTR) after incubation with nicotinamide adenine dinucleotide (NADH) under anaerobic condition for 6 h (Figure 35a). The resulting solution was then analyzed by HPLC. An elution peak at 12.82 min corresponding to IPM-Br was observed in the HPLC trace of the resulting solution (Figure 35b), indicating that the NTR-induced activation of SPNpd and the subsequent release of IPM-Br. This phenomenon could be explained as following: the nitro groups of SPNpd were reduced to amino groups catalyzed by NTR followed by the release of active IPM-Br under hypoxic environment (Figure 33a).

Confocal fluorescence imaging revealed that both SPNpd and SPNc had a similar cell uptake with the nearly same fluorescence intensity (Figure 35c), probably because of their similar sizes and surface zeta potentials. MTS reagent was applied for cell viabilities tests. Under normoxic condition, without photoirradiation, both SPNpd and SPNc had negligible cytotoxicity against 4T1 cells even at a high concentration of 100 μg mL^{-1} (Figure 35d). Upon NIR photoirradiation at 808 nm, the cell viability of SPNc (45.7%) and SPNpd (43.7%) treated cells had no significant differences. This indicated that the prodrug was not activated and the conjugation of prodrug had no obviously impact on the PDT efficacy of SPNpd under the normoxic condition, which was consistent with SOSG assay results. However, under hypoxic condition without photoirradiation, the cell viability of SPNpd treated cells decreased to 34.1%, 2.5 times lower than that of SPNpd under normoxic condition (84.8%) (Figure 35e), indicating the prodrug activation. With NIR photoirradiation under hypoxic condition, the cell viability of SPNpd-treated cells further reduced to 8.3%, 4.3 times lower than SPNc (35.7%). These data confirmed the chemotherapeutic ability of SPNpd was only activated under hypoxic condition and synergized with PDT for amplified therapeutic effect.

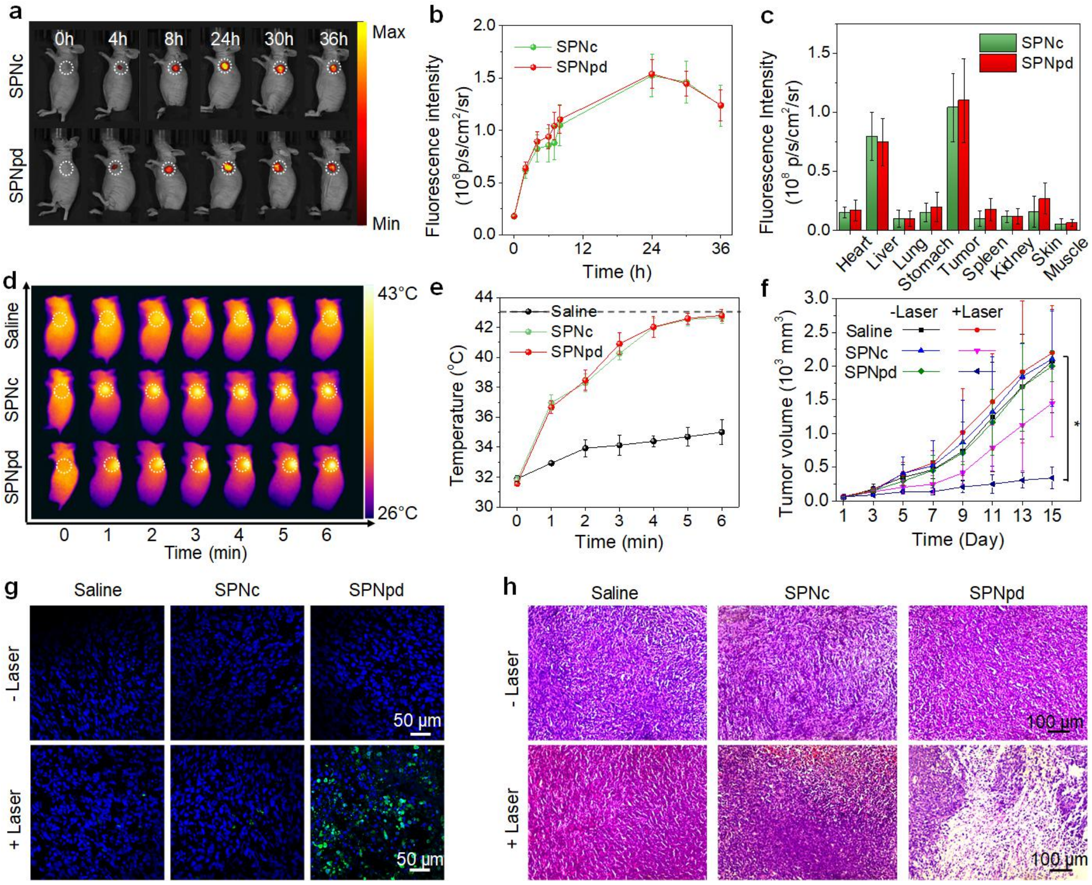

Figure 36. *In vivo* NIR fluorescence imaging and synergistic cancer therapy. a) Representative NIR fluorescence images of 4T1 tumor-bearing living mice at different time points after intravenous injection of SPNpd or SPNc (400 μg mL^{-1}, 0.2 mL). NIR fluorescence images were acquired for 0.1 s at 840 ± 10 nm upon excitation at 675 ± 10 nm. The tumor site is marked by white circle. b) Quantification of NIR fluorescence intensities of tumor as a function of post-injection time of SPNpd or SPNc. c) Quantification of major organs of mice 36 h after systemic administration of SPNpd or SPNc. Error bars were based on standard error of mean (SEM) (n = 3). d) IR thermal images of 4T1 tumor-bearing mice at 24 h post-injection of saline, SPNc, or SPNpd (400 μg mL^{-1}, 0.2 mL) after NIR photoirradiation at 808 nm (0.3 W cm^{-2}) for different amount of time. The tumor site is marked by white circle. e) Mean tumor temperature during NIR photoirradiation at 24 h post-injection of saline, SPNc, or SPNpd (400 μg mL^{-1}, 0.2 mL) into 4T1 tumor-bearing mice. Error bars are based on standard error of mean (SEM) (n = 4). f) Tumor growth curves for mice injected with saline, SPNc, or SPNpd (400 μg mL^{-1}, 0.2 mL) after photoirradiation for 6 min (*p < 0.05, n = 4). g) Immunofluorescent staining of caspase-3 for the tumors of mice treated with saline, SPNc, or SPNpd (400 μg mL^{-1}, 0.2 mL) with or

without NIR photoirradiation. Green and blue fluorescence indicates caspase-3 and nucleus staining, respectively. The tumors for immunofluorescent staining of caspase-3 were collected after 15 days of treatment. (scale bars = 50 μm). h) H&E staining of tumors from different treatment mice groups.

To identify the optimal *in vivo* phototherapeutic timepoint for SPNpd, NIR fluorescence imaging was conducted in the subcutaneous 4T1 xenograft tumor mouse model. After systemic administration of SPNpd or SPNc into the tumor-bearing living mice through tail vein, the NIR fluorescence images were longitudinally acquired (Figure 36a). The fluorescence of tumors gradually increased and reached maximum at 24 h post-injection for both SPNs (Figure 36b), indicating that both SPNs could passively accumulate in the tumor via the EPR effect. Moreover, the fluorescence intensity of tumor was 1.5-fold higher than that of liver for both SPNs (Figure 36c), indicating the preferred accumulation at tumor site. Additionally, *ex vivo* data showed that both SPNs had similar biodistribution (Figure 37a).

Because the tumors had the highest fluorescence intensities at 24 h post-injection of SPNc, or SPNpd, NIR photoirradiation was conducted at this time point for cancer phototherapy. Under NIR photoirradiation at 808 nm, the tumor temperatures for both SPNs-treated mice gradually increased (Figure 36d and 36e); however, the maximum temperatures for both SPNs-treated mice were controlled below the apoptosis threshold temperature (43 °C) so that the photothermal effect was minimized.[152] To evaluate the *in vivo* therapeutic effect, the tumor sizes were monitored continuously for 15 days after treatment (Figure 36f). Without photoirradiation, the tumor for SPNc or SPNpd treated mice showed similar growth rate as that for saline-treated mice, indicating no therapeutic effect for both SPNs. This also reflected that despite the presence of the prodrug units in SPNpd, the prodrug was inactive probably because SPNpd was accumulated at the position of tumor where the hypoxia was not high enough. With photoirradiation, the tumor growth of SPNc-treated mice was only slow down; in contrast, the tumor growth of SPNpd-treated mice was effectively deterred. This proved that the solo PDT induced by the SPN core was unable to inhibit the tumor growth. However, as the oxygen in the hypoxic tumor microenvironment was further depleted by PDT process, SPNpd was activated and the toxic drug (IPM-Br) was released, leading to the synergetic PDT and chemotherapy for amplified antitumor efficacy.

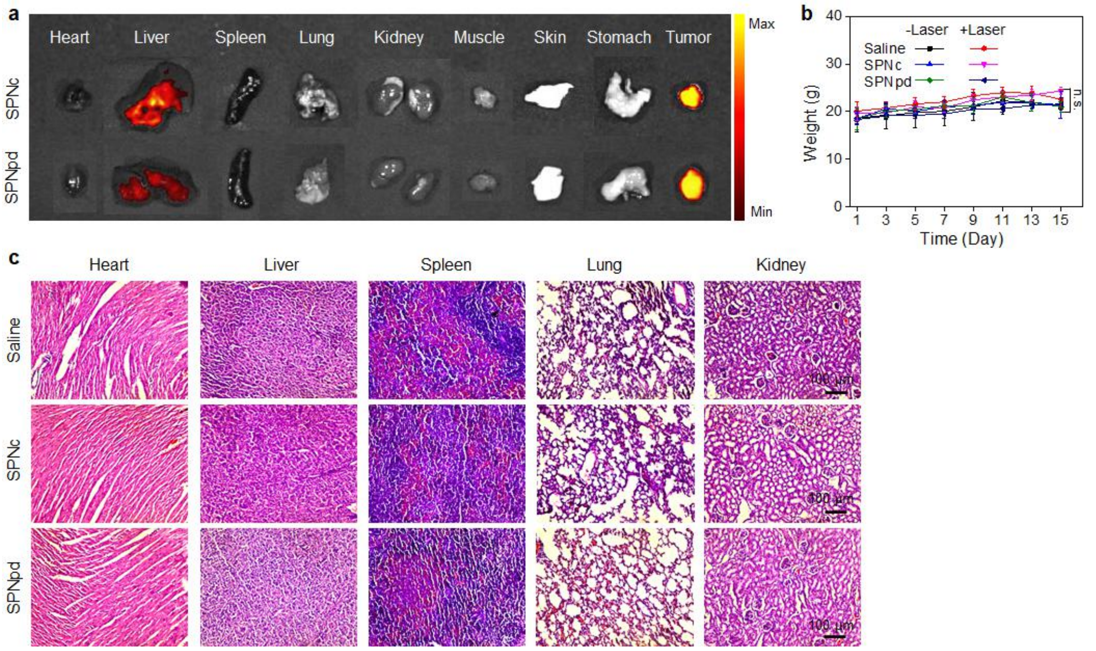

Figure 37. *Ex vivo* data of organs and tumor of SPNpd and SPNc treated mice. a) *Ex vivo* fluorescence images of major organs of mice 36 h after systemic administration of SPNc or SPNpd. Fluorescence images were acquired for 0.1 s at 840 ± 10 nm upon excitation at 675 ± 10 nm. b) Body weight of mice after intravenous injection of saline, SPNc or SPNpd (400 μg mL^{-1},

0.2 mL) into 4T1 tumor-bearing mice with or without laser irradiation at 808 nm (0.3 W cm^{-2}) for 6 min (n = 4). c) H&E staining of major organs in living mice after systemic administration of saline, SPNc or SPNpd with NIR laser (808nm, 0.3 W cm^{-2}) irradiation for 6 min (scale bars = 100 μm).

All mice groups had no significant weight loss for 15 days after treatment (Figure 37b) and no noticeable histopathological abnormalities were found in all major organs (Figure 37c), showing the good biosafety of both SPNs. Immunofluorescence caspase-3 staining revealed that without photoirradiation, no green fluorescence from the apoptotic cells was observed for both SPNs-treated mice. By contrast, with photoirradiation, stronger fluorescence from apoptotic cells was detected for the tumor tissues of SPNpd-treated mice as compared those with saline or SPNc treated mice. Similarly, H&E staining showed more necrotic cells for SPNpd-treated mice relative to SPNc-treated mice with photoirradiation, whereas other groups showed no obvious cell necrosis (Figure 36h). The histological analysis further verified the superior synergetic PDT and chemotherapy efficacy of SPNpd over the solo PDT of SPNc.

6.1.4 Conclusion

In summary, we have synthesized an organic photodynamic nano-prodrug (SPNpd) that can specifically release the chemodrug under photoirradiation-promoted hypoxia tumor microenvironment to exert synergetic PDT and chemotherapy. SPNpd possessed the photodynamic efficacy 18 times higher than ICG. Moreover, owing to its hypoxia-activated synergetic therapeutic effect, SPNpd showed 4.3-times higher anticancer efficacy as compared with its prodrug-free counterpart (SPNc) under NIR photoirradiation and hypoxic condition. After systemic administration, both SPNpd and SPNc effectively accumulated at the tumor of living mice due to their small sizes and stealthy PEG grafting. Without NIR photoirradiation, no obvious antitumor effect was observed for both SPNs, implying the inactivation of SPNpd. In contrast, photoirradiation effectively inhabited the tumor growth of SPNpd-treated mice, which was not possible for SPNc. Along with immunofluorescence staining and H&E staining, the *in vivo* data validated that SPNpd acted as a photoirradiation-promoted and hypoxia-responsive nanoprodrug for synergetic PDT and chemotherapy. To the best of our knowledge, SPNpd represents the first hypoxia-responsive phototherapeutic polymeric prodrug. In view of its high biosafety, preferable accumulation in tumor and NIR light response, such an organic phototherapeutic prodrug could be used for synergetic cancer therapy.

6.2 Dendronized SPN for Remote Activation of Gene Expression

6.2.1 Background

Regulation of cellular behaviors and transgene systems can provide useful tools to understand their physiological roles and potentially lead to innovative therapies. In this regard, gene therapy that utilizes viral or non-viral vectors to deliver exogenous nucleic acids into specific cells has become a promising therapeutic approach to treat genetic diseases and cancers.[153] However, it is challenging to precisely regulate gene expression at designated location and time to minimize off-target expression.[154] Although encoding tissue-specific promoters in therapeutic nucleic acids is one possible solution, which is less likely to be generalized for various diseases. Recently, gas molecules, radio waves and light have been used to remotely achieve gene expression. Due to low toxicity, easy tunability and high spatiotemporal resolution, light is the most ideal inducer among them. However, current methods are generally limited to UV[155] and visible light[156] with limited tissue penetration, restricting their *in vivo* applications. Moreover, optical responsive components can chemically integrate into therapeutic nucleic acids rather than into delivery vectors, partially complicating their performances.

In this study, we report the design and synthesis of a NIR absorbing dendronized semiconducting polymer (DSP) and demonstrate its proof-of-concept application as a photothermal nanocarrier and intracellular nanotransducer for remote activation of gene expression. DSP comprises three key components (Figure 38a): the hydrophobic semiconducting backbone, the cationic third-generation polyamidoamine (PAMAM3) side chains, and the neural PEG blocks, which serve as the NIR photothermal nanotransducer, the gene vector and the water-solubility enhancer, respectively.

6.2.2 Experiment sections

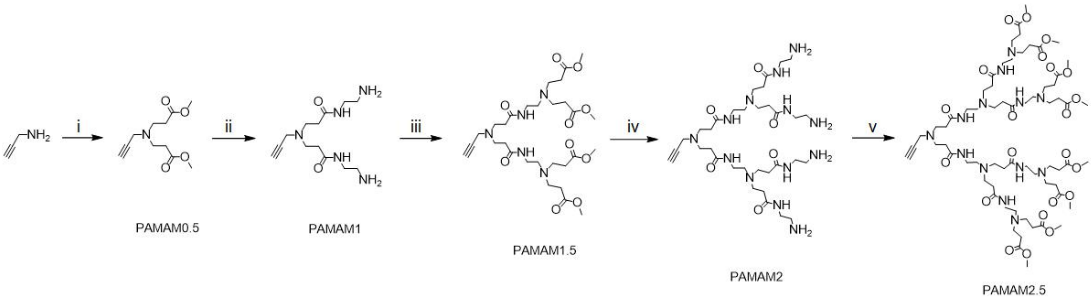

Scheme 8. The synthesis route of PAMAM2.5. i) Methyl acrylate, methanol, 30 ºC, 48 h. ii) Ethylenediamine, methanol, 30 ºC, 48 h. iii) Methyl acrylate, methanol, 30 ºC, 72 h. iv) Ethylenediamine, methanol, 30 ºC, 48 h. v) Methyl acrylate, methanol, 30 ºC, 72 h.

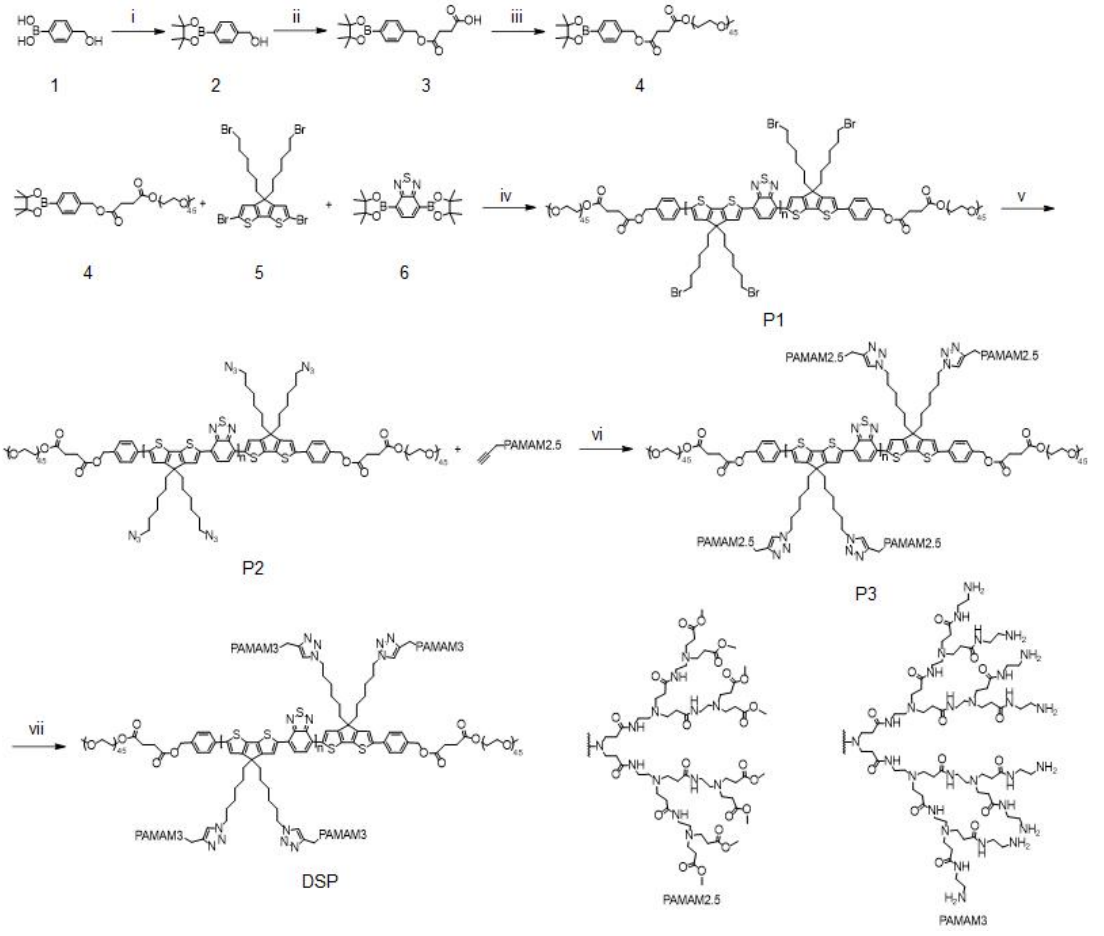

Scheme 9. Synthetic route of DSP. Conditions and reagents: i) Pinacol, magnesium sulfate ($MgSO_4$), THF, 25 ºC, 24 h. ii) Succinic anhydride, 4-dimethylaminopyridine (DMAP), THF, 25 ºC, 36 h. iii) PEG ($M_n = 2000$), dicyclohexylcarbodiimide (DCC), DMAP, THF, 25 ºC, 48 h. iv) $Pd(PPh_3)_4$, K_2CO_3, methyltrioctylammonium chloride, toluene/H_2O, 100 ºC, 2 h. v) NaN_3, DMF. vi) CuBr, PMDETA, THF, 25 ºC, 48 h. vii) Ethylenediamine, methanol.

Synthesis of PAMAM2.5. To a solution of propargylamine (220 mg, 4.00 mmol) in methanol (10.0 mL) was added dropwise methyl acrylate (1.30 mL, 14.4 mmol). The reaction mixture was stirred under argon for 48 h at 30 °C. The reaction solution was then evaporated, and the residue was purified by column chromatography on silica gel with hexane/EtOAc (2/1), yielding PAMAM0.5 (0.9 g, 85 % yield) as a colorless oil. ^{1}H NMR (300 MHz, CDCl3) δ 3.53 (d, J = 9.8 Hz, 6H), 3.30 (d, J = 2.3 Hz, 2H), 2.71 (t, J = 7.0 Hz, 4H), 2.34 (t, J = 7.0 Hz, 4H), 2.19–2.11 (m, 1H).

To a solution PAMAM0.5 (0.9 g, 4 mmol) in methanol (2.00 mL) was added ethylenediamine (5.00 mL, 75.0 mmol). The reaction mixture was stirred under argon for 48 h at 30 °C. The reaction solution was evaporated, and then the residue was purified by precipitation with methanol/Et_2O three times, yielding PAMAM1 (1.13 g, 97.7 % yield) as a pale viscous oil. To a solution of PAMAM1 (1.1 g, 4 mmol) in methanol (10.0 mL) was added dropwise methyl acrylate (2.50 mL, 27.6 mmol). The reaction mixture was stirred under argon for 72 h at 30 °C. The reaction solution was evaporated, and then the residue was purified by column chromatography on silica gel with EtOAc/methanol (10/1), yielding PAMAM 1.5 (1.93 g, 79.1 % yield) as colorless oil. ^{1}H NMR (300 MHz, $CDCl_3$) δ 7.16 (s, 2H), 3.66 (s, 12H), 3.44 (t, J = 6.6 Hz, 2H), 3.29 (q, J = 5.7 Hz, 4H), 2.84 (t, J = 6.6 Hz, 4H), 2.75 (t, J = 6.7 Hz, 8H), 2.54 (t, J = 5.9 Hz, 4H), 2.48 – 2.28 (m, 12H), 2.19 (s, 2H).

To a solution of PAMAM1.5 (1.35 g, 2.15 mmol) in methanol (5.00 mL) was added ethylenediamine (2.80 mL, 42.0 mmol). The reaction mixture was stirred under argon for 48 h at 30 °C. The reaction solution was evaporated, and then the residue was purified by precipitation with methanol /Et_2O three times, yielding PAMAM2 (1.3 g, 81.7% yield) as pale viscous oil. To a solution of PAMAM2 (1.3 g, 1.85

mmol) in methanol (10.0 mL) was added dropwise methyl acrylate (2.50 mL, 27.6 mmol). The reaction mixture was stirred under argon for 72 h at 30 °C. The solvent was evaporated, and then the residue was purified by column chromatography on silica gel with EtOAc/MeOH (2/1), yielding PAMAM 2.5 (1.98 g, 78.9 % yield) as yellow oil. ^{1}H NMR (300 MHz, $CDCl_3$) δ 7.80 (t, J = 5.2 Hz, 2H), 7.13 (t, J = 5.2 Hz, 4H), 3.671 (s, 24H), 3.45 (d, J = 1.9 Hz, 2H), 3.28 (dd, J = 11.6, 5.8 Hz, 12H), 2.91 – 2.71 (m, 28H), 2.56 (tt, J = 15.7, 7.7 Hz, 12H), 2.48 – 2.30 (m, 28H), 2.21 (d, J = 2.1 Hz, 1H).

Synthesis of 4-(4,4,5,5-tetramethyl-1,3,2-dioxaborolan-2-yl)benzyl succinate polyethylene glycol ester (HMPBA-pin-SA-PEG, monomer 4). 4-(Hydroxymethyl) phenylboronic acid (compound 1) (1 g, 0.65 mmol) was added into anhydrous THF followed by the addition of pinacol (0.93 g, 7.9 mmol). $MgSO_4$ (0.15 g) was then added into the mixture. The mixture was stirred at room temperature for 24 h and then filtered to remove the precipitate. The filtrate was evaporated by rotary evaporation and 40 mL of chloroform was added to dissolve the residue. The obtained solution was then washed with water (3 × 30 mL) and dried over Na_2SO_4 overnight. After filtration and evaporation, 4-(4,4,5,5-tetramethyl-1,3,2-dioxaborolan-2-yl) phenyl methanol (compound 2) (1.13 g, 58.6% yield) was obtained. ^{1}H NMR (300 MHz, $CDCl_3$) δ 7.79 (d, J = 8.0 Hz, 2H), 7.34 (d, J = 8.0 Hz, 2H), 4.68 (s, 2H), 1.34 (s, 12H)

Compound 2 (0.5 g, 2.11 mmol), succinic anhydride (0.75 g, 4.2 mmol), DMAP (10 mg, 0.1 mmol) were dissolved in anhydrous THF (10 mL). The mixture was stirred at room temperature for 36 h. Methanol (2 mL) was then added and continuously stirred for 1 h to hydrolyze the excess succinic anhydride. THF were evaporated under vacuum and chloroform (20 mL) was added to dissolve the residue. The solution was washed with HCl (0.1 M, 20 mL) and water (30 mL). The organic phase was dried over Na_2SO_4 overnight and then evaporated to obtain 4-(4,4,5,5-tetramethyl-1,3,2-dioxaborolan-2-yl) benzyl succinate (compound 3) as colorless oil (0.68g, 71% yield). ^{1}H NMR (300 MHz, $CDCl_3$) δ 7.82 (d, J = 8.0 Hz, 2H), 7.36 (d, J = 7.9 Hz, 2H), 5.27–5.10 (m, 2H), 2.79–2.64 (m, 4H), 1.36 (s, 12H).

Compound 3 (0.7 g, 2.1 mmol), mPEG (M_n = 2000) (3.4 g, 1.75 mmol) and DMAP (0.13 g, 1.05 mmol) were dissolved in anhydrous DCM (10 mL), then DCC (0.86 g, 4.2 mmol) was added to the solution dropwise. The reaction was conducted at room temperature for 48 h. And then filtered to remove the precipitate. The solvent was evaporated and the crude product was dissolved in water and purified by dialysis. After vacuum freeze drying, monomer 4 as white solids were obtained. ^{1}H NMR (300 MHz, $CDCl_3$) δ 7.81 (d, J = 8.0 Hz, 2H), 7.35 (d, J = 8.0 Hz, 2H), 5.15 (s, 2H), 3.78–3.58 (m, 190H), 2.70 (s, 4H), 1.35 (s, 12H).

Synthesis of (4-(4,4,5,5-tetramethyl-1,3,2-dioxaborolan-2-yl)benzyl) succinate polyethylene glycol ester end-capped poly{4-(4,4-bis(6-bromohexyl)-6-methy-l 4H-cyclopenta[2,1-b:3,4-b']dithiophen-2-yl)-7-methylbenzo[c][1,2,5]thiadiazole} (P1). 4,4'-Bis-(5-bromopentyl)-4H-cyclopenta[2,1-b:3,4-b′]dithiophene (monomer 5) (50 mg, 0.075 mmol), 2,1,3- benzothiadiazole-4,7-bis (boronic acid pinacol ester) (monomer 6) (27 mg, 0.068 mmol), $Pd(PPh_3)_4$ (3 mg, 0.03 mmol) and K_2CO_3 (122.5

mg, 0.69 mmol) were added in a 50 mL Schlenk tube. Then toluene (1.5 mL) with methyltrioctylammonium chloride (1 mg) and water (1.25 mL) were added to the reaction tube. The reaction vessel was degassed by freeze-pump-thaw circles for three times. The reaction was conducted at 100 ºC, when the solution turning to blue, monomer 4 (16.9 mg, 0.0075 mmol) (dissolved in 0.4 ml of toluene, also degassed by freeze-pump-thaw) solution was added into the tube. The mixture was stirred at 100 ºC overnight. The product was extracted with DCM and washed by water (20 mL) and brine (30 mL). The organic phase was concentrated and powered into excess methanol. The polymer was filtered and washed with methanol and acetone and then dried under vacuum for 24 h. ^{1}H NMR (300 MHz, $CDCl_3$) δ 8.11 (s, 2H), 7.95–7.83 (m, 1H), 7.61 (s, 3H), 6.91 (s, 2H), 3.64 (s, 12H), 3.35 (d, J = 16.6 Hz, 4H), 1.74 (s, 6H), 1.25 (s, 28H), 0.86 (d, J = 7.5 Hz, 6H). GPC data: M_n = 8414, PDI = 1.791.

Synthesis of (4-(4,4,5,5-tetramethyl-1,3,2-dioxaborolan-2-yl)benzyl) succinate polyethylene glycol ester end-capped poly[4-(4,4-bis(6-azidohexyl)-6-methyl-4H-cyclopenta[2,1-b:3,4-b']dithiophen-2-yl)-7-methylbenzo[c][1,2,5]thiadiazole (P2). P1 (30 mg) and NaN_3 (12 mg) were dissolved in DMF (5 mL)/ THF (10 mL). The mixture was stirred at 25 ºC for 24 h. The solvent was evaporated and CH_2Cl_2 was added to dissolve the residue. The solution was washed with water and brine. The organic phase was collected and dried with Na_2SO_4. The organic phase was concentrated and powered into excess methanol. The polymer was filtered and washed with methanol and acetone and then dried under vacuum for 24 h. ^{1}H NMR

(300 MHz, $CDCl_3$) δ 8.09 (s, 2H), 7.96–7.82 (m, 1H), 7.59 (s, 2H), 6.91 (s, 2H), 3.64 (s, 11H), 3.21 (d, J = 16.6 Hz, 4H), 1.73 (s, 6H), 1.26 (s, 28H), 0.88 (d, J = 7.5 Hz, 6H).

Synthesis of (4-(4,4,5,5-tetramethyl-1,3,2-dioxaborolan-2-yl)benzyl) succinate polyethylene glycol ester end-capped poly{4-[4,4-bis(4-PAMAM3-1H-1,2,3-triazol-1-yl)hexyl]-6-methyl-4H-cyclopenta[2,1-b:3,4-b']dithiophen-2-yl}-7-methylbenzo[c] [1,2,5]thiadiazole} (DSP). P2 (30 mg, 0.05 mmol), propargylamine core PAMAM 2.5 (0.3 g, 0.2 mmol) and CuBr (31.2 mg, 0.2 mmol) were dissolved in THF (10 mL), then PMDETA (233 μL, 1 mmol) was added to this solution. The mixture was stirred at 25 ºC for 24 h. The solvent was evaporated. Excess of DCM was added to the residue, and washed with water and brine. The organic phase was collected and dried with Na_2SO_4. The organic phase was concentrated and powered into excess methanol. The polymer P3 was filtered and washed with methanol and acetone and then dried under vacuum for 24 h. Then, P3 (60 mg, 0.03 mmol) was dissolved in methanol (20 mL)/ THF (5 mL). Ethylenediamine (36 mg, 0.6 mmol) was added to this solution dropwise and slowly. The mixture was stirred at 60 ºC for 48 h. The solvent was evaporated and the residue was dissolved in water, and purified by dialysis. After vacuum freeze-drying, DSP was obtained. ^1H NMR (300 MHz, methanol-D_4) δ 8.06 (d, J = 26.7 Hz, 2H), 7.72 – 7.47 (m, 3H), 7.03 (d, J = 14.5 Hz, 3H), 6.61 (d, J = 3.6 Hz, 1H), 3.62 (d, J = 19.1 Hz, 106H), 3.01 (d, J = 4.2 Hz, 16H), 2.95 – 2.69 (m, 135H), 2.64 – 2.52 (m, 36H), 2.36 (dd, J = 20.1, 12.0 Hz, 72H), 1.72 (s, 6H), 1.30 (dd, J = 28.9, 17.8 Hz, 34H), 0.91 (s, 6H).

6.2.3 Results and Discussions

DSP was synthesized *via* a graft-on approach (Scheme 8 and 9). Pd-catalyzed Suzuki polymerization of PEG-functionalized endcapping agent (4), 4,4’-bis-(5-bromopentyl)-4H-cyclopenta[2,1-b:3,4-b’]dithiophene (5), and 2,1,3-benzothiadiazole-4,7-bis (boronic acid pinacol ester) (6) led to the PEG-endcapped poly(cyclopentadithiophene-*alt*-benzothiadiazole) triblock copolymer (P1). The bromide groups of P1 was converted into the azide groups, allowing it to undergo the click reaction to graft PAMAM2.5 onto it. At last, the resulted grafted SP (P3) reacted with ethylenediamine *via* Michael-addition reaction to convert PAMAM2.5 into the third-generation form (PAMAM3), affording the final polymer (DSP). This section was performed by me, while *in vitro* characterization of DSP and its transfection capability, *in vitro* and *in vivo* DSP-mediated photothermal activation of gene expression were performed by Dr Yan Lyu.

The intermediate polymers and DSP were characterized by NMR. DSP could be directly dissolved in aqueous solution and buffer, that can not only efficiently deliver genes into cells but also convert NIR light into heat for photothermal applications. In association with heat inducible promoter modified genes, DSP can act as the intracellular photothermal nanotransducer to remotely activate gene expression upon NIR light irradiation at 808 nm.

7. Conclusion

This thesis report describes my research work on design and synthesize SPNs for *in vivo* molecular imaging (including PA imaging, afterglow imaging and chemiluminescence imaging). Due to their excellent optical properties and good biocompatibility, SPNs composed of opto-electronically active semiconducting polymers (SPs) and amphiphilic polymer matrixes have gained more and more attention as a new category of molecular imaging nano-agents. By changing the chemical structures of SPs and encapsulating them into different amphiphilic polymers, it is also feasible to use SPNs as phototherapeutic agents for cancer phototherapy including photothermal and photodynamic therapy.

In **Chapter 3**, by grafting amphiphilic PEG on DPP-based SPs backbones, PCD-PEG and PFD-PEG were developed, showing better photostability and higher PA signal as compared to concentration-match GNRs. Moreover, with a self-assembled small nanoparticular structure (40 nm), the strong PA brightness of PCD-PEG allowed it to image the tumor of living mice with a tumor SBR as high as 7. In addition, these kind SPAs solve the potentially aggregation issues of traditional method prepared micelle-like SPNs. To enhance the imaging sensitivity, activatable PA probes that change their signals in response to the biomolecule of interest have been developed. However, the SBRs for such probes still heavily rely on the concentration difference of endogenous biomarkers between diseased and normal tissues. To solve this problem, SPNphs composed of thermoresponsive PDMA-*r*-HPA side chain and PCPDTBT backbone were developed for contrast-enhanced *in vivo* imaging of tumor. SPNph1 had LCSTs at 48 °C, and underwent phase separation to form large nanoparticles. Thus, SPNph1 possessed thermoresponsive PA property, showing 1.6-fold signal increment when temperature was above LCSTs. In addition, the thermoresponsive PA property of SPNph1 enabled in situ remote manipulation of PA signals by laser-irradiation-mediated heating, leading to the 1.43-fold enhancement in the tumor SBR (as high as 6.12).

Immunotherapy that aims to train host immune cells to kill malignant cells provides new treatment options for various cancer types. However, immunotherapy often encounters the dilemma of limited patient response rate in the clinic. To optimize immunotherapeutic benefits, molecular imaging is promising for real-time evaluation of immunoactivation in living subjects. In **Chapter 4**, by encapsulating a $O_2^{\bullet -}$-cleavable chemiluminescence substrate, SPNRs were developed for real-time *in vivo* chemiluminescence imaging of cancer immunotherapy and applied for high throughput screening of immunotherapeutics. Upon specific reaction with $O_2^{\bullet -}$, the sulfonate ester of caged dioxetanes within SPNRs is specifically cleaved to induce the deprotection of Tf group, resulting in the formation of high-energy unstable phenolate-dioxetane derivatives. Subsequently, iCRET from the unstable derivatives to the SP occurs, leading to the generation of chemiluminescence signals at the long wavelength range of the PFODBT at 700 nm. In addition, SPNR3 could detect the levels of endogenous $O_2^{\bullet -}$ in different cell lines, revealing that cytotoxic T cell has higher endogenous $O_2^{\bullet -}$ level than cancer and normal cells. More importantly, SPNR3 had preferential accumulated in the tumor of living mice after systemic administration, and could turn on the chemiluminescence signals to report the $O_2^{\bullet -}$ level related to the populations of activated cytotoxic T cells and helper T cells in the course of cancer immunotherapy.

Cancer metastasis with its complex cell-biological mechanism, systemic nature, and drug resistance is the main cause of recurrence and death of most cancer patients. Early diagnosis of metastases thus plays a critical role in the effective treatment of cancer. Afterglow or persistent luminescence has drawn more attention for its low background and high sensitivity as a result of eliminated real-time light excitation. In **Chapter 5**, TPP incorporated PPV-based semiconducting copolymers SPN-TPPs were developed as afterglow nanoagent for *in vivo* imaging of tumor hypoxia and tumor metastasis. With the help of FRET and promoted $^1O_2$ generation, SPN2.5 showed the NIR afterglow with the maximum at 720 nm, and amplified afterglow intensity that was 6.12-fold brighter than the nondoped nanoparticles (SPN0). The O_2 sensitive afterglow of SPN2.5 made it useful for *in vivo* imaging of tumor hypoxia, showing 3.6-fold higher afterglow in skin than that in hypoxic tumor. In addition, due to the high sensitivity of afterglow imaging, metastatic tumor tissues could be delineated by afterglow spots on the intestines of SPN2.5 injected mice, which was not possible for fluorescence imaging.

Most tumor cells are in the hypoxic environment resulting from their rapid oxygen consuming for vasculature growth and cell proliferation. Despite the promise of PDT in cancer therapy, its oxygen reliance limits the therapeutic effect against tumor hypoxia. In fact, as a result of oxygen consumption and microvascular damage during PDT, PDT even increases the tumor hypoxia to a certain extent and further decreases its antitumor efficacy. In **Chapter 6**, SPNpd composed of PCPDTBT as light-responsive photodynamic core, hypoxia-cleavable linker and IPM-Br as the chemotherapeutic drug have been developed for solving the tumor hypoxia problem. Upon photoirradiation at 808 nm, SPNpd can generate $^1O_2$ for PDT; meanwhile, the tumor hypoxia in association with photoirradiation-depleted oxygen level specifically initiates the fragmentation and release of IPM-Br catalyzed by nitro reductase, leading to cell death. Without NIR photoirradiation, no obvious antitumor effect was observed for both SPNs, implying the inactivation of SPNpd. Owing to its hypoxia activated synergetic therapeutic effect, SPNpd showed 4.3-fold higher anticancer efficacy as compared with its prodrug free counterpart (SPNc) under NIR photoirradiation and hypoxic condition. Along with immunofluorescence staining and H&E staining, the in vivo data validated that SPNpd acted as a photoirradiation-promoted and hypoxia-responsive nanoprodrug for synergetic PDT and chemotherapy. In addition, dendronized semiconducting polymer (DSP) was developed for gene delivery and photothermal activation. Such kind of polymers holds great promise to be developed into nanomedicines for remotely controlled therapeutic transgene dosing.

Although preclinical applications of SPNs for molecular imaging and phototherapy have obtained significant progress, there are still some issues that need to be considered for their clinical applications. SPNs have been reported to show minimal cytotoxicity and even good *in vivo* biocompatibility, but their long-term biosafety and biodegradation in living bodies need to be concerned and require further investigation. Potential influences of SPNs on the fate and functions of some cell types, such as stem cells, red blood cells and immune cells are largely unknown and need to be studied. Oral or local administration rather than intravenous injection in some specific diseases settings is another strategy to reduce the accumulation and retention of SPNs in the body. We could also design biodegradable SPNs for clinic applications. For example, we added the vinylene bonds into the SP backbone, making it enzymatically biodegradable with enhanced mass absorption coefficient and photothermal conversion efficacy. We designed fully organic nanoagents compose of π-conjugated oxidizable optical polymer, were easily degraded by myeloperoxidase and lipase rich in phagocytes, transforming from nonfluorescent nanoparticles into NIR fluorescent ultrasmall metabolites (~1 nm). In addition, we should solve the problem of how to effective activating SPNs in human body. It is dependent on which kind of disease we will treat. If we apply SPNs for imaging and treatment of dermatosis or skin cancers, we can directly use NIR laser irradiation to activate the SPNs, because the penetration depth is enough for these applications. If we use this kind of probe to treat deep-seated tumors, we should activate it by red-shifting the light response into the second NIR window (ranging from 1000 to 1700 nm, showing the intrinsic advantages of reduced light–tissue interaction and increased allowable power density for light irradiation) or by integrating with endoscopic light delivery system or ultrasound. In addition, phototherapy is always combined with surgery in clinic. For example, phototherapy assistant surgery has been used for esophageal and esophagogastric junction cancers treatment in clinic. In conclusion, SPNs can serve as a versatile nanoplatform for emerging biomedical applications with the rapid progress of nanotechnology.

8. Reference

[1] H. A. Loomans-Kropp, A. Umar, *NPJ precision oncology* **2019**, *3*, 3.

[2] S. A. Soper, A. Rasooly, *The Analyst* **2016**, *141*, 367.

[3] A. Marusyk, K. Polyak, *Biochimica et biophysica acta* **2010**, *1805*, 105.

[4] A. Hellebust, R. Richards-Kortum, *Nanomedicine (London, England)* **2012**, *7*, 429.

[5] M. A. Pysz, S. S. Gambhir, J. K. Willmann, *Clinical radiology* **2010**, *65*, 500.

[6] L. Bu, B. Shen, Z. Cheng, *Advanced drug delivery reviews* **2014**, *76*, 21.

[7] M. Wu, J. Shu, *Contrast media & molecular imaging* **2018**, *2018*, 1382183.

[8] D. P. Cormode, P. C. Naha, Z. A. Fayad, *Contrast media & molecular imaging* **2014**, *9*, 37.

[9] A. Zhu, D. Lee, H. Shim, *Seminars in oncology* **2011**, *38*, 55.

[10] Q. You, Q. Sun, M. Yu, J. Wang, S. Wang, L. Liu, Y. Cheng, Y. Wang, Y. Song, F. Tan, N. Li, *ACS Applied Materials & Interfaces* **2017**, *9*, 40017.

[11] Z.-Y. Chen, Y.-X. Wang, Y. Lin, J.-S. Zhang, F. Yang, Q.-L. Zhou, Y.-Y. Liao, *BioMed research international* **2014**, *2014*, 819324.

[12] M. Herranz, A. Ruibal, *Journal of oncology* **2012**, *2012*, 863747.

[13] C. Wang, Z. Wang, T. Zhao, Y. Li, G. Huang, B. D. Sumer, J. Gao, *Biomaterials* **2018**, *157*, 62.

[14] M. Gao, F. Yu, C. Lv, J. Choo, L. Chen, *Chemical Society Reviews* **2017**, *46*, 2237.

[15] J. Cao, B. Zhu, K. Zheng, S. He, L. Meng, J. Song, H. Yang, *Frontiers in bioengineering and biotechnology* **2020**, *7*, 487.

[16] G. Hong, A. L. Antaris, H. Dai, *Nature Biomedical Engineering* **2017**, *1*, 0010.

[17] V. Pansare, S. Hejazi, W. Faenza, R. K. Prud'homme, *Chemistry of materials : a*

publication of the American Chemical Society **2012**, *24*, 812.

[18] Y. Ma, X. Liu, Q. Ma, Y. Liu, *OncoTargets and therapy* **2018**, *11*, 8517.

[19] J. Gao, X. Chen, Z. Cheng, *Current topics in medicinal chemistry* **2010**, *10*, 1147.

[20] Z. Huang, H. Zeng, I. Hamzavi, A. Alajlan, E. Tan, D. McLean, H. Lui, *Journal of biomedical optics* **2006**, *11*, 34010.

[21] S. He, J. Song, J. Qu, Z. Cheng, *Chemical Society Reviews* **2018**, *47*, 4258.

[22] L.-Y. Huang, S. Zhu, R. Cui, M. Zhang, *Analytical Chemistry* **2020**, *92*, 535.

[23] D. M. Close, T. Xu, G. S. Sayler, S. Ripp, *Sensors (Basel, Switzerland)* **2011**, *11*, 180.

[24] L. Mezzanotte, M. Root, H. Karatas, E. Goua, C. Löwik, *Trends in Biotechnology* **2017**, *35*.

[25] C. E. Badr, B. A. Tannous, *Trends in biotechnology* **2011**, *29*, 624.

[26] J. Li, L. Chen, L. Du, M. Li, *Chemical Society Reviews* **2013**, *42*, 662.

[27] V. Ntziachristos, D. Razansky, *Chemical Reviews* **2010**, *110*, 2783.

[28] L. V. Wang, S. Hu, *Science* **2012**, *335*, 1458.

[29] Y. Jiang, K. Pu, *Small* **2017**, *13*, 1700710.

[30] J. Wu, L. You, L. Lan, H. J. Lee, S. T. Chaudhry, R. Li, J.-X. Cheng, J. Mei, *Advanced Materials* **2017**, *29*, 1703403.

[31] G. S. Filonov, A. Krumholz, J. Xia, J. Yao, L. V. Wang, V. V. Verkhusha, *Angewandte Chemie (International ed. in English)* **2012**, *51*, 1448.

[32] J. F. Lovell, C. S. Jin, E. Huynh, H. Jin, C. Kim, J. L. Rubinstein, W. C. W. Chan, W. Cao, L. V. Wang, G. Zheng, *Nature Materials* **2011**, *10*, 324.

[33] a) J. V. Jokerst, A. J. Cole, D. Van de Sompel, S. S. Gambhir, *ACS Nano* **2012**, *6*, 10366; b) J. Liu, X. Zheng, L. Yan, L. Zhou, G. Tian, W. Yin, L. Wang, Y. Liu, Z. Hu, Z. Gu, C. Chen, Y. Zhao, *ACS Nano* **2015**, *9*, 696.

[34] A. De La Zerda, C. Zavaleta, S. Keren, S. Vaithilingam, S. Bodapati, Z. Liu, J. Levi, B. R. Smith, T.-J. Ma, O. Oralkan, Z. Cheng, X. Chen, H. Dai, B. T. Khuri-Yakub, S. S. Gambhir, *Nature Nanotechnology* **2008**, *3*, 557.

[35] K. Yang, L. Feng, X. Shi, Z. Liu, *Chemical Society Reviews* **2013**, *42*, 530.

[36] K. H. Song, C. Kim, C. M. Cobley, Y. Xia, L. V. Wang, *Nano letters* **2009**, *9*, 183.

[37] A. Ruggiero, C. H. Villa, J. P. Holland, S. R. Sprinkle, C. May, J. S. Lewis, D. A. Scheinberg, M. R. McDevitt, *International journal of nanomedicine* **2010**, *5*, 783.

[38] X. Huang, J. Song, B. C. Yung, X. Huang, Y. Xiong, X. Chen, *Chemical Society reviews* **2018**, *47*, 2873.

[39] Q. Miao, K. Pu, *Bioconjugate Chemistry* **2016**, *27*, 2808.

[40] a) A. Dragulescu-Andrasi, S.-R. Kothapalli, G. A. Tikhomirov, J. Rao, S. S. Gambhir, *Journal of the American Chemical Society* **2013**, *135*, 11015; b) J. Lin, S. Wang, P. Huang, Z. Wang, S. Chen, G. Niu, W. Li, J. He, D. Cui, G. Lu, X. Chen, Z. Nie, *ACS Nano* **2013**, *7*, 5320.

[41] a) Y. Zhang, M. Jeon, L. J. Rich, H. Hong, J. Geng, Y. Zhang, S. Shi, T. E. Barnhart, P. Alexandridis, J. D. Huizinga, M. Seshadri, W. Cai, C. Kim, J. F. Lovell, *Nature Nanotechnology* **2014**, *9*, 631; b) C. Xie, X. Zhen, Y. Lyu, K. Pu, *Advanced Materials* **2017**, *29*, 1703693; c) X. Meng, Y. Yang, L. Zhou, l. Zhang, Y. Lv, S. Li, Y. Wu, M. Zheng, W. Li, G. Gao, G. Deng, T. Jiang, D. Ni, P. Gong, L. Cai, *Theranostics* **2017**, *7*, 1781.

[42] Q. Chen, X. Liu, J. Chen, J. Zeng, Z. Cheng, Z. Liu, *Advanced Materials* **2015**, *27*, 6820.

[43] J. Levi, S. R. Kothapalli, T.-J. Ma, K. Hartman, B. T. Khuri-Yakub, S. S. Gambhir, *Journal of the American Chemical Society* **2010**, *132*, 11264.

[44] L. Zhang, S. Gao, F. Zhang, K. Yang, Q. ma, L. Zhu, *ACS nano* **2014**, *8*.

[45] P. Huang, J. Lin, X. Wang, Z. Wang, C. Zhang, M. He, K. Wang, F. Chen, Z. Li, G. Shen, D. Cui, X. Chen, *Advanced Materials* **2012**, *24*, 5104.

[46] D. Gao, X. Guo, X. Zhang, S. Chen, Y. Wang, T. Chen, G. Huang, Y. Gao, Z. Tian, Z. Yang, *Materials Today Bio* **2020**, *5*, 100035.

[47] M. Arruebo, N. Vilaboa, B. Sáez-Gutierrez, J. Lambea, A. Tres, M. Valladares, A. González-Fernández, *Cancers* **2011**, *3*, 3279.

[48] U. Chitgupi, Y. Qin, J. F. Lovell, *Nanotheranostics* **2017**, *1*, 38.

[49] S. Farkona, E. P. Diamandis, I. M. Blasutig, *BMC medicine* **2016**, *14*, 73.

[50] H. Abrahamse, M. R. Hamblin, *The Biochemical journal* **2016**, *473*, 347.

[51] M. Nita, A. Grzybowski, *Oxidative medicine and cellular longevity* **2016**, *2016*, 3164734.

[52] N. Kotagiri, G. P. Sudlow, W. J. Akers, S. Achilefu, *Nature Nanotechnology* **2015**, *10*, 370.

[53] C.-P. Liu, T.-H. Wu, C.-Y. Liu, K.-C. Chen, Y.-X. Chen, G.-S. Chen, S.-Y. Lin, *Small* **2017**, *13*, 1700278.

[54] A. C. S. Samia, X. Chen, C. Burda, *Journal of the American Chemical Society* **2003**, *125*, 15736.

[55] J. Ge, M. Lan, B. Zhou, W. Liu, L. Guo, H. Wang, Q. Jia, G. Niu, X. Huang, H. Zhou, X. Meng, P. Wang, C.-S. Lee, W. Zhang, X. Han, *Nature Communications* **2014**, *5*, 4596.

[56] a) Y. Liu, Y. Liu, W. Bu, C. Cheng, C. Zuo, Q. Xiao, Y. Sun, D. Ni, C. Zhang, J. Liu, J. Shi, *Angewandte Chemie International Edition* **2015**, *54*, 8105; b) J. Xu, L. Xu, C. Wang, R. Yang, Q. Zhuang, X. Han, Z. Dong, W. Zhu, R. Peng, Z. Liu, *ACS Nano* **2017**, *11*, 4463.

[57] J. F. Lovell, C. S. Jin, E. Huynh, H. Jin, C. Kim, J. L. Rubinstein, W. C. W. Chan, W. Cao, L. V. Wang, G. Zheng, *Nature Materials* **2011**, *10*, 324.

[58] P. García Calavia, G. Bruce, L. Pérez-García, D. A. Russell, *Photochemical & Photobiological Sciences* **2018**, *17*, 1534.

[59] P. Juzenas, W. Chen, Y.-P. Sun, M. A. N. Coelho, R. Generalov, N. Generalova, I. L. Christensen, *Advanced drug delivery reviews* **2008**, *60*, 1600.

[60] D. Maggioni, M. Galli, L. D'Alfonso, D. Inverso, M. V. Dozzi, L. Sironi, M. Iannacone, M. Collini, P. Ferruti, E. Ranucci, G. D'Alfonso, *Inorganic Chemistry* **2015**, *54*, 544.

[61] J. Hu, Y. A. Tang, A. Elmenoufy, H. Xu, Z. Cheng, X. Yang, *Small (Weinheim an der Bergstrasse, Germany)* **2015**, *11*.

[62] X. Li, N. Kwon, T. Guo, Z. Liu, J. Yoon, *Angewandte Chemie International Edition* **2018**, *57*, 11522.

[63] S. Mallidi, S. Anbil, A.-L. Bulin, G. Obaid, M. Ichikawa, T. Hasan,

Theranostics **2016**, *6*, 2458.

[64] W. Sheng, S. He, W. J. Seare, A. Almutairi, *Journal of biomedical optics* **2017**, *22*, 80901.

[65] D. Jaque, L. Martínez Maestro, B. del Rosal, P. Haro-Gonzalez, A. Benayas, J. L. Plaza, E. Martín Rodríguez, J. García Solé, *Nanoscale* **2014**, *6*, 9494.

[66] A. C. V. Doughty, A. R. Hoover, E. Layton, C. K. Murray, E. W. Howard, W. R. Chen, *Materials (Basel, Switzerland)* **2019**, *12*, 779.

[67] Y. Ren, Q. Chen, H. Qi, L. Ruan, *Nanomaterials (Basel, Switzerland)* **2017**, *7*, 416.

[68] M. Zhang, H. S. Kim, T. Jin, J. Woo, Y. J. Piao, W. K. Moon, *Oncotarget* **2017**, *8*, 86566.

[69] K. Yang, J. Wan, S. Zhang, B. Tian, Y. Zhang, Z. Liu, *Biomaterials* **2012**, *33*, 2206.

[70] S. Augustine, J. Singh, M. Srivastava, M. Sharma, A. Das, B. D. Malhotra, *Biomaterials Science* **2017**, *5*, 901.

[71] C. M. Hessel, V. P. Pattani, M. Rasch, M. G. Panthani, B. Koo, J. W. Tunnell, B. A. Korgel, *Nano letters* **2011**, *11*, 2560.

[72] J. Mei, Y. Diao, A. L. Appleton, L. Fang, Z. Bao, *Journal of the American Chemical Society* **2013**, *135*, 6724.

[73] A. Rose, Z. Zhu, C. F. Madigan, T. M. Swager, V. Bulović, *Nature* **2005**, *434*, 876.

[74] A. B. Sanghvi, K. P. H. Miller, A. M. Belcher, C. E. Schmidt, *Nature Materials* **2005**, *4*, 496.

[75] K. Pu, N. Chattopadhyay, J. Rao, *Journal of controlled release : official journal of the Controlled Release Society* **2016**, *240*, 312.

[76] Y.-H. Chan, P. J. Wu, *Particle & Particle Systems Characterization* **2014**, *32*.

[77] Y. Yang, L. Wang, B. Wan, Y. Gu, X. Li, *Frontiers in bioengineering and biotechnology* **2019**, *7*, 320.

[78] K. Pu, A. J. Shuhendler, J. V. Jokerst, J. Mei, S. S. Gambhir, Z. Bao, J. Rao, *Nature Nanotechnology* **2014**, *9*, 233.

[79] J. Li, J. Rao, K. Pu, *Biomaterials* **2018**, *155*, 217.

[80] Y. Lyu, Y. Fang, Q. Miao, X. Zhen, D. Ding, K. Pu, *ACS Nano* **2016**, *10*, 4472.

[81] C. Xie, X. Zhen, Q. Lei, R. Ni, K. Pu, *Advanced Functional Materials* **2017**, *27*, 1605397.

[82] G. Hong, Y. Zou, A. L. Antaris, S. Diao, D. Wu, K. Cheng, X. Zhang, C. Chen, B. Liu, Y. He, J. Z. Wu, J. Yuan, B. Zhang, Z. Tao, C. Fukunaga, H. Dai, *Nature Communications* **2014**, *5*, 4206.

[83] A. J. Shuhendler, K. Pu, L. Cui, J. P. Uetrecht, J. Rao, *Nature biotechnology* **2014**, *32*, 373.

[84] C. Wu, S. J. Hansen, Q. Hou, J. Yu, M. Zeigler, Y. Jin, D. R. Burnham, J. D. McNeill, J. M. Olson, D. T. Chiu, *Angewandte Chemie International Edition* **2011**, *50*, 3430.

[85] J.-C. Yu, Y.-L. Chen, Y.-Q. Zhang, X.-K. Yao, C.-G. Qian, J. Huang, S. Zhu, X.-Q. Jiang, Q.-D. Shen, Z. Gu, *Chemical Communications* **2014**, *50*, 4699.

[86] C. Yin, X. Zhen, H. Zhao, Y. Tang, Y. Ji, Y. Lyu, Q. Fan, W. Huang, K. Pu, *ACS Applied Materials & Interfaces* **2017**, *9*, 12332.

[87] X. Zhen, J. Zhang, J. Huang, C. Xie, Q. Miao, K. Pu, *Angewandte Chemie International Edition* **2018**, *57*, 7804.

[88] J. Zhang, X. Zhen, P. K. Upputuri, M. Pramanik, P. Chen, K. Pu, *Advanced Materials* **2017**, *29*, 1604764.

[89] Q. Miao, Y. Lyu, D. Ding, K. Pu, *Advanced Materials* **2016**, *28*, 3662.

[90] Y. Lyu, X. Zhen, Y. Miao, K. Pu, *ACS Nano* **2017**, *11*, 358.

[91] X. Zhen, X. Feng, C. Xie, Y. Zheng, K. Pu, *Biomaterials* **2017**, *127*, 97.

[92] Y. Lyu, J. Zeng, Y. Jiang, X. Zhen, T. Wang, S. Qiu, X. Lou, M. Gao, K. Pu, *ACS Nano* **2018**, *12*, 1801.

[93] J. Li, K. Pu, *Chemical Society Reviews* **2019**, *48*, 38.

[94] S. Li, K. Chang, K. Sun, Y. Tang, N. Cui, Y. Wang, W. Qin, H. Xu, C. Wu, *ACS Applied Materials & Interfaces* **2016**, *8*, 3624.

[95] Y. Tang, H. Chen, K. Chang, Z. Liu, Y. Wang, S. Qu, H. Xu, C. Wu, *ACS Applied Materials & Interfaces* **2017**, *9*, 3419.

[96] L. Huang, Z. Li, Y. Zhao, J. Yang, Y. Yang, A. I. Pendharkar, Y. Zhang, S. Kelmar, L. Chen, W. Wu, J. Zhao, G. Han, *Advanced Materials* **2017**, *29*, 1604789.

[97] H. Zhu, J. Li, X. Qi, P. Chen, K. Pu, *Nano Letters* **2018**, *18*, 586.

[98] K. Chang, Z. Liu, X. Fang, H. Chen, X. Men, Y. Yuan, K. Sun, X. Zhang, Z. Yuan, C. Wu, *Nano Letters* **2017**, *17*, 4323.

[99] D. Li, G. Zhang, W. Xu, J. Wang, Y. Wang, L. Qiu, J. Ding, X. Yang, in *Theranostics, Vol. 7*, **2017**, pp. 4029.

[100] B. Guo, G. Feng, P. N. Manghnani, X. Cai, J. Liu, W. Wu, S. Xu, X. Cheng, C. Teh, B. Liu, *Small* **2016**, *12*, 6243.

[101] X. Zhen, C. Xie, K. Pu, *Angewandte Chemie International Edition* **2018**, *57*, 3938.

[102] Y. Jiang, L. Jingchao, X. Zhen, C. Xie, K. Pu, *Advanced materials (Deerfield Beach, Fla.)* **2018**, *30*.

[103] Y. Lyu, C. Xie, S. A. Chechetka, E. Miyako, K. Pu, *Journal of the American Chemical Society* **2016**, *138*, 9049.

[104] J. Li, C. Xie, J. Huang, Y. Jiang, Q. Miao, K. Pu, *Angewandte Chemie International Edition* **2018**, *57*, 3995.

[105] X. Wu, Y. Zhang, K. Takle, O. Bilsel, Z. Li, H. Lee, Z. Zhang, D. Li, W. Fan, C. Duan, E. M. Chan, C. Lois, Y. Xiang, G. Han, *ACS Nano* **2016**, *10*, 1060.

[106] C. J. Rijcken, C. J. Snel, R. M. Schiffelers, C. F. van Nostrum, W. E. Hennink, *Biomaterials* **2007**, *28*, 5581.

[107] D. Zhang, G.-B. Qi, Y.-X. Zhao, S.-L. Qiao, C. Yang, H. Wang, *Advanced Materials* **2015**, *27*, 6125.

[108] Z. Yang, Y. Dai, C. Yin, Q. Fan, W. Zhang, J. Song, G. Yu, W. Tang, W. Fan, B. C. Yung, J. Li, X. Li, X. Li, Y. Tang, W. Huang, J. Song, X. Chen, *Advanced Materials* **2018**, *30*, 1707509.

[109] Y. Jiang, D. Cui, Y. Fang, X. Zhen, P. K. Upputuri, M. Pramanik, D. Ding, K. Pu, *Biomaterials* **2017**, *145*, 168.

[110] E. S. Lee, V. G. Deepagan, D. G. You, J. Jeon, G.-R. Yi, J. Y. Lee, D. S. Lee, Y. D. Suh, J. H. Park, *Chemical Communications* **2016**, *52*, 4132.

[111] D. Lee, S. Khaja, J. C. Velasquez-Castano, M. Dasari, C. Sun, J. Petros, W. R. Taylor, N. Murthy, *Nature Materials* **2007**, *6*, 765.

[112] Y. H. Seo, A. Singh, H.-J. Cho, Y. Kim, J. Heo, C.-K. Lim, S. Y. Park, W.-D. Jang, S. Kim, *Biomaterials* **2016**, *84*, 111.

[113] X. Zhen, C. Zhang, C. Xie, Q. Miao, K. L. Lim, K. Pu, *ACS Nano* **2016**, *10*, 6400.

[114] H. J. Kim, Y. H. Seo, S. An, A. Jo, I. C. Kwon, S. Kim, *Theranostics* **2018**, *8*, 1798.

[115] D. Mao, W. Wu, S. Ji, C. Chen, F. Hu, D. Kong, D. Ding, B. Liu, *Chem* **2017**, *3*, 991.

[116] J. Koury, M. Lucero, C. Cato, L. Chang, J. Geiger, D. Henry, J. Hernandez, F. Hung, P. Kaur, G. Teskey, A. Tran, *Journal of immunology research* **2018**, *2018*, 9585614.

[117] W. Wei, D. Jiang, E. B. Ehlerding, Q. Luo, W. Cai, *Trends in cancer* **2018**, *4*, 359.

[118] a) D. M. Pardoll, *Nature Reviews Cancer* **2012**, *12*, 252; b) V. Ntziachristos, J. Ripoll, L. V. Wang, R. Weissleder, *Nature Biotechnology* **2005**, *23*, 313; c) A. M. Smith, M. C. Mancini, S. Nie, *Nat Nanotechnol* **2009**, *4*, 710.

[119] R. Tavaré, H. Escuin-Ordinas, S. Mok, M. N. McCracken, K. A. Zettlitz, F. B. Salazar, O. N. Witte, A. Ribas, A. M. Wu, *Cancer Research* **2016**, *76*, 73.

[120] B. M. Luby, C. D. Walsh, G. Zheng, *Angewandte Chemie International Edition* **2019**, *58*, 2558.

[121] B. C. Dickinson, C. J. Chang, *Nature Chemical Biology* **2011**, *7*, 504.

[122] E. L. Yarosz, C.-H. Chang, *Immune network* **2018**, *18*, e14.

[123] P. Wang, J. Geng, J. Gao, H. Zhao, J. Li, Y. Shi, B. Yang, C. Xiao, Y. Linghu, X. Sun, X. Chen, L. Hong, F. Qin, X. Li, J.-S. Yu, H. You, Z. Yuan, D. Zhou, R. L. Johnson, L. Chen, *Nature Communications* **2019**, *10*, 755.

[124] L. A. Sena, S. Li, A. Jairaman, M. Prakriya, T. Ezponda, D. A. Hildeman, C. R. Wang, P. T. Schumacker, J. D. Licht, H. Perlman, P. J. Bryce, N. S. Chandel, *Immunity* **2013**, *38*, 225.

[125] P. Cheng, J. Zhang, J. Huang, Q. Miao, C. Xu, K. Pu, *Chemical Science* **2018**, *9*, 6340.

[126] O. Green, T. Eilon, N. Hananya, S. Gutkin, C. R. Bauer, D. Shabat, *ACS Central Science* **2017**, *3*, 349.

[127] L. E. Padgett, H. M. Tse, *The Journal of Immunology* **2016**, *197*, 1733.

[128] J. J. Hu, N. K. Wong, S. Ye, X. Chen, M. Y. Lu, A. Q. Zhao, Y. Guo, A. C. Ma, A. Y. Leung, J. Shen, D. Yang, *Journal of the American Chemical Society* **2015**, *137*, 6837.

[129] J. Huang, J. Li, Y. Lyu, Q. Miao, K. Pu, *Nature Materials* **2019**, *18*, 1133.

[130] M. Pudlo, C. Demougeot, C. Girard-Thernier, *Medicinal Research Reviews* **2017**, *37*, 475.

[131] O. Moiseeva, V. Bourdeau, A. Roux, X. Deschênes-Simard, G. Ferbeyre, *Molecular and Cellular Biology* **2009**, *29*, 4495.

[132] A. Angajala, S. Lim, J. B. Phillips, J. H. Kim, C. Yates, Z. You, M. Tan, *Frontiers in Immunology* **2018**, *9*, 1605.

[133] D. T. Dickey, L. L. Muldoon, N. D. Doolittle, D. R. Peterson, D. F. Kraemer, E. A. Neuwelt, *Cancer Chemother Pharmacol* **2008**, *62*, 235.

[134] a) S. Valastyan, R. A. Weinberg, *Cell* **2011**, *147*, 275; b) P. S. Steeg, *Nature Medicine* **2006**, *12*, 895.

[135] R. M. Kwee, T. C. Kwee, *Gastric Cancer* **2009**, *12*, 6.

[136] R. Qiao, R. Zhu, M. Gao, *Current Pharmaceutical Design* **2015**, *21*, 6260.

[137] P. Mi, D. Kokuryo, H. Cabral, H. Wu, Y. Terada, T. Saga, I. Aoki, N. Nishiyama, K. Kataoka, *Nature Nanotechnology* **2016**, *11*, 724.

[138] D. Entenberg, S. Voiculescu, P. Guo, L. Borriello, Y. Wang, G. S. Karagiannis, J. Jones, F. Baccay, M. Oktay, J. Condeelis, *Nature Methods* **2018**, *15*, 73.

[139] Q. le Masne de Chermont, C. Chanéac, J. Seguin, F. Pellé, S. Maîtrejean, J.-P. Jolivet, D. Gourier, M. Bessodes, D. Scherman, *Proceedings of the National Academy of Sciences* **2007**, *104*, 9266.

[140] J. Shi, X. Sun, J. Li, H. Man, J. Shen, Y. Yu, H. Zhang, *Biomaterials* **2015**, *37*, 260.

[141] A. Abdukayum, J.-T. Chen, Q. Zhao, X.-P. Yan, *Journal of the American Chemical Society* **2013**, *135*, 14125.

[142] T. Maldiney, A. Bessière, J. Seguin, E. Teston, S. K. Sharma, B. Viana, A. J. J. Bos, P. Dorenbos, M. Bessodes, D. Gourier, D. Scherman, C. Richard, *Nature Materials* **2014**, *13*, 418.

[143] F. Liu, W. Yan, Y.-J. Chuang, Z. Zhen, J. Xie, Z. Pan, *Scientific Reports* **2013**, *3*, 1554.

[144] T. Maldiney, M. U. Kaikkonen, J. Seguin, Q. le Masne de Chermont, M. Bessodes, K. J. Airenne, S. Ylä-Herttuala, D. Scherman, C. Richard, *Bioconjugate Chemistry* **2012**, *23*, 472.

[145] Y. Jiang, J. Huang, X. Zhen, Z. Zeng, J. Li, C. Xie, Q. Miao, J. Chen, P. Chen, K. Pu, *Nature communications* **2019**, *10*. 2064.

[146] Q. Miao, C. Xie, X. Zhen, Y. Lyu, H. Duan, X. Liu, J. V. Jokerst, K. Pu, *Nature Biotechnology* **2017**, *35*, 1102.

[147] B. W. Henderson, V. H. Fingar, *Cancer Res* **1987**, *47*, 3110.

[148] Y. Cheng, H. Cheng, C. Jiang, X. Qiu, K. Wang, W. Huan, A. Yuan, J. Wu, Y. Hu, *Nature communications* **2015**, *6*, 8785.

[149] C. Qian, J. Yu, Y. Chen, Q. Hu, X. Xiao, W. Sun, C. Wang, P. Feng, Q.-D. Shen, Z. Gu, *Advanced Materials* **2016**, *28*, 3313.

[150] D. Luo, K. A. Carter, D. Miranda, J. F. Lovell, *Advanced Science* **2017**, *4*, 1600106.

[151] J. X. Duan, H. Jiao, J. Kaizerman, T. Stanton, J. W. Evans, L. Lan, G. Lorente, M. Banica, D. Jung, J. Wang, H. Ma, X. Li, Z. Yang, R. M. Hoffman, W. S. Ammons, C. P. Hart, M. Matteucci, *Journal of Medicinal Chemistry* **2008**, *51*, 2412.

[152] C. S. Jin, J. F. Lovell, J. Chen, G. Zheng, *ACS Nano* **2013**, *7*, 2541.

[153] L. Naldini, *Nature* **2015**, *526*, 351.

[154] M. A. Kay, *Nature Reviews Genetics* **2011**, *12*, 316.

[155] B. C. McKay, L. J. Stubbert, C. C. Fowler, J. M. Smith, R. A. Cardamore, J. C. Spronck, *Proceedings of the National Academy of Sciences of the United States of America* **2004**, *101*, 6582.

[156] M. Folcher, S. Oesterle, K. Zwicky, T. Thekkottil, J. Heymoz, M. Hohmann, M. Christen, M. Daoud El-Baba, P. Buchmann, M. Fussenegger, *Nature Communications* **2014**, *5*, 5392.